Local probe investigations of the electronic phase diagrams of iron pnictides and chalcogenides

DISSERTATION

zur Erlangung des akademischen Grades

Doctor rerum naturalium
(Dr. rer. nat.)

vorgelegt

der Fakultät Mathematik und Naturwissenschaften
der technischen Universität Dresden

von

Diplom-Physiker Philipp Materne

geboren am 07.03.1987 in Dresden

1. Gutachter: Prof. Dr. Hans-Henning Klauß

2. Gutachter: Prof. Dr. Joachim Wosnitza

Eingereicht am 27.04.2015

Disputation am 24.09.2015

Die Dissertation wurde in der Zeit von August 2011 bis April 2015
im Institut für Festkörperphysik angefertigt.

Abstract

In this work, the electronic phase diagrams of $Ca_{1-x}Na_xFe_2As_2$ and $Fe_{1+y}Te$ were investigated using muon spin relaxation and Mössbauer spectroscopy.

Single crystals of $Ca_{1-x}Na_xFe_2As_2$ with $x = 0.00$, 0.35, 0.50, and 0.67 were examined. The undoped 122 parent compound $CaFe_2As_2$ is a semi metal and shows antiferromagnetic commensurate spin density wave order below 167 K. By hole doping via Na substitution, the magnetic order is suppressed and superconductivity emerges including a Na-substitution level region, where both phases coexist. Upon Na substitution, a tilting of the magnetic moments out of the ab-plane is found.

The interaction of the magnetic and superconducting order parameter in this coexistence region was studied and a nanoscopic coexistence of both order parameters is found. This is proven by a reduction of the magnetic order parameter of 7 % in $x = 0.50$ below the superconducting transition temperature. This reduction was analysed using Landau theory and a systematic correlation between the reduction of the magnetic order parameter and the ratio of the transition temperatures, T_c/T_N, for the 122 family of the iron pnictides is presented.

The magnetic phase transition is accompanied by a tetragonal-to-orthorhombic phase transition. The lattice dynamics at temperatures above and below this magneto-structural phase transition were studied and no change in the lattice dynamics were found. However, the lattice for finite x is softer than for the undoped compound.

For $x = 0.67$, diluted magnetic order is found. Therefore, the magnetism in $Ca_{1-x}Na_xFe_2As_2$ is persistent even at optimal doping. The superconducting state is investigated by measuring the temperature dependence of the magnetic penetration depth, where two superconducting gaps with a weighting of nearly 50:50 are obtained. A temperature independent anisotropy of the magnetic penetration depth $\gamma_\lambda = 1.5(4)$ is obtained, which is much smaller compared to other 122 compounds indicating a more three-dimensional behaviour of $Ca_{1-x}Na_xFe_2As_2$.

Powder samples of $Fe_{1+y}Te$ with $y = 0.06$, 0.12, 0.13, and 0.15 were examined. Fluctuating paramagnetic moments at room temperature were found, which are independent of the excess iron level y. Below 100 K, a magnetic precursor phase is observed, which is independent of y. $Fe_{1.06}Te$ shows a commensurate spin density wave phase below T_N, while for $y \geq 0.13$ an incommensurate spin density wave phase below T_N is found. However, a slowing down of the magnetic fluctuations with decreasing temperature and static magnetic order at lowest temperature are observed.

In dieser Arbeit wurden die elektronischen Phasendiagramme von $Ca_{1-x}Na_xFe_2As_2$ and $Fe_{1+y}Te$ mit Hilfe der Myonspinrelaxations- und Mössbauerspektroskopie untersucht.

Einkristalle von $Ca_{1-x}Na_xFe_2As_2$ mit $x = 0.00$, 0.35, 0.50 und 0.67 wurden untersucht. Das undorierte 122-System $CaFe_2As_2$ ist ein Halbmetal und zeigt eine antiferromagnetische Spindichtewelle unterhalb von 167 K. Substituiert man Ca durch Na, werden Löcher in das System eingebracht. Die magnetische Ordnung wird mit steigendem Na-Anteil unterdrückt und Supraleitung tritt auf. Dabei existiert ein Na-Substitutionslevelbereich, in welchem Magnetismus und Supraleitung koexistieren. Desweiteren wurde ein herausdrehen der magnetischen Momente aus der ab-Ebene als Funktion von x beobachtet.

Die Wechselwirkung des magnetischen mit dem supraleitenden Ordnungsparameter in der Koexistenzregion wurde untersucht und nanoskopische Koexistenz der beiden Ordnungsparameter wurde gefunden. Dies konnte durch eine Reduktion des magnetischen Ordnungsparameteres um 7 % in $x = 0.50$ unterhalb der supraleitenden Ordnungstemperatur gezeigt werden. Diese Reduktion wurde mit Hilfe der Landautheorie untersucht und es wurden systematische Korrelationen zwischen der Reduktion des magnetischen Ordnungsparamteres und dem Verhältnis der Übergangstemperaturen, T_c/T_N, in der 122-Familie der Eisenpniktide gefunden.

Der magnetische Phasenübergang wird von einem strukturellen Phasenübergang begleitet. Die Gitterdynamik wurde bei Temperaturen oberhalb und unterhalb dieses magneto-elastischen Phasenübergangs untersucht. Es wurden keine Änderungen in der Gitterdynamik festgestellt. Jedoch konnte festgestellt werden, dass das Gitter für endliche x weicher ist als für das undotierte System.

Für $x = 0.67$ wurde festgestellt, dass der Magnetismus im $Ca_{1-x}Na_xFe_2As_2$-System auch noch bei optimaler Dotierung zu finden ist. In der supraleitenden Phase wurde die Temperaturabghängigkeit der magnetischen Eindringtiefe untersucht und es wurden zwei supraleitende Bandlücken gefunden. Die Anisotropie der magnetischen Eindringtiefe ist temperaturunabhängig und mit $\gamma_\lambda = 1.5(4)$ wesentlich kleiner als in anderen 122-Verbindungen, was für eine erhöhte Dreidimensionalität in $Ca_{1-x}Na_xFe_2As_2$ spricht.

Pulverproben von $Fe_{1+y}Te$ mit $y = 0.06$, 0.12, 0.13 und 0.15 wurden untersucht. Es wurden fluktuierende paramagnetische Momente bei Raumtemperatur gefunden, welche unabhängig vom Überschusseisenlevel y sind. Unterhalb von 100 K wurde eine magnetische Vorgängerphase gefunden, welche unabhängig von y ist. Mit fallender Temperatur wurde eine Verlangsamung der magnetischen Fluktuationen festgestellt, welche in einer statischen magnetischen Ordnung bei tiefen Temperaturen münden.

Contents

Contents

Abbreviations and symbols

AFM	antiferromagnetic, antiferromagnet, antiferromagnetism
ARPES	angle resolved photo-emission spectroscopy
$\vec{B} = \mu_0 \vec{H}$	magnetic field
BCS	Bardeen-Cooper-Schrieffer
B_{hf}	magnetic hyperfine field
CDW	charge densitiy wave
δ_{C}	chemical shift
DFT	density functional theory
DOS	density of states
E_{F}	Fermi energy
EFG	electric field gradient
η	asymmetry parameter of the electric quadrupole interaction
E_{R}	recoil energy
f_i	muon spin precession frequency on site i
f	recoilless fraction
FeChn	iron-chalcogen
FePn	iron-pnictogen
FS	Fermi surface
g	gyromagnetic ratio
Γ_{nat}	natural line width $\Gamma_{\mathrm{nat}} = 4.7$ neV (for $^{57}\mathrm{Fe}$)
γ_λ	magnetic penetration depth anisotropy
GKT	Gauss-Kubo-Toyabe
LKT	Lorentz-Kubo-Toyabe
LPD	London penetration depth
λ_{L}	longitudinal muon spin relaxation rate
λ_{L}	transversal muon spin relaxation rate
μSR	muon spin relaxation
M_{eff}	effective vibrating mass
PM	paramagnetic
T_c	superconducting transition temperature
θ_{D}	Debye temperature
θ	angle between the magnetic hyperfine field and the principal axis of the EFG
T_{N}	Néel, magnetic transition temperature
$T_{\mathrm{N}}^{\mathrm{onset}}$	highest temperature with a finite magnetic volume fraction
$T_{\mathrm{N}}^{100\%}$	highest temperature with a magnetic volume fraction of 100 %
T_{N}^{χ}	magnetic transition temperature determined by magnetic susceptibility measurements
SC	superconductor, superconducting, superconductivity
SDW	spin density wave
V_{mag}	magnetic volume fraction
V_{zz}	z-component of the principal axis of the EFG

c   speed of light c = 299792458 m/s

e   elementary charge e = $1.602176565 \cdot 10^{-19}$ A·s

γ_μ gyromagnetic ratio of the muon $\gamma_\mu = 2\pi \cdot 135.5342(5)$MHz/T

$\hbar$ Planck constant $\hbar = 6.62606957 \cdot 10^{-34}$ J·s

k_B Boltzman constant $k_B = 1.3806488(13) \cdot 10^{-23}$ J/K

μ_B Bohr magneton $\mu_B = 9.27400968(20) \cdot 10^{-24}$ J/T

μ_P magnetic moment of the proton $\mu_P = 1.410606743(33) \cdot 10^{-26}$ J/T

m_e electron mass $m_e = 510.998928(11)$ keV/c^2

m_p proton mass $m_p = 938.272046(21)$ MeV/c^2

τ_μ mean lifetime of the muon $\tau_\mu = 2.19703(4)$ μs

1. Introduction

"*It's a neural-net processor. It thinks and learns like we do. It's superconducting at room temperature.*" - Tarissa Dyson about the central processing unit of a terminator [1].

Room-temperature superconductivity - what is the reality in James Cameron's *Terminator 2*, is still a dream of the future in the real world.

But lets take a step back. Everything started with the discovery of a vanished resistivity in metallic mercury below 4.2 K by Heike Kamerlingh Onnes in 1911, who was rewarded with the Nobel Prize in physics in 1913. From this starting point, one major goal of the basic research was and is to find a compound, which is superconducting at room temperature. As time was passing by, the superconducting transition temperature in conventional superconductors increased to $T_c = 39$ K in MgB_2, which was discovered in 2001 [2]. The term conventional superconductivity is not well-defined in the literature, but is usually associated with phonon-mediated superconductivity, which can be described by the famous Bardeen-Cooper-Schrieffer (BCS) theory. The BCS-theory was published in 1957 and describes the formation of a coherent ground state out of electron pairs with opposite spin and momenta [3]. Bardeen, Cooper, and Schrieffer were awarded with the Nobel Prize in physics in 1972 for their theory. With the discovery of the cuprate superconductors in 1986 by Bednorz and Müller, who where rewarded with the Nobel Prize in physics in 1987, T_c raised up to 153 K [4], which is up to now the highest achieved superconducting transition temperature. Superconductivity in cuprates is found in close proximity to magnetic order: The antiferromagnetic order in the parent compounds are at least as important as the high T_c, as magnetic moments were seen as deleterious to the superconductivity in earlier times. The cuprates are unconventional superconductors. Unfortunately, a complete theory of unconventional superconductivity is still lacking up to now.

With the discovery of the iron pnictides in 2008 [5], a new class of high-temperature superconductors was identified. This class takes the proximity of magnetic order and superconductivity to its extremes, as under certain conditions superconductivity and magnetic order coexisting in the same phase competing for the same electronic states at the Fermi surface. The understanding of this coexistence phase as well as of the high-temperature superconductivity in general in these compounds is an important topic in contemporary correlated-electron physics.

Therefore, studying this crossover from magnetic order to superconductivity with focus on the phase boundary between both orders is crucial for an understanding of the high-temperature superconductivity in the iron-based superconductors and for unconventional superconductivity in general. A combined study of macroscopic techniques and local magnetic probes will give further insight in the electronic properties of these compounds.

In this work, I examined $Ca_{1-x}Na_xFe_2As_2$ and $Fe_{1+y}Te$ using muon spin relaxation and Mössbauer spectroscopy to study the pure magnetic and superconducting phases as well

as the coexistence region. For a better understanding of the experiments, the principle of both techniques is given. Muon spin relaxation spectroscopy is described in Sec. 2 with focus on magnetic order and superconductivity. Mössbauer spectroscopy is described in Sec. 3 with focus on magnetic order and lattice dynamics. In Sec. 4, a short introduction to the physics of iron pnictides and chalcogenides is given. In Sec. 5 and 6, the relevant properties of both investigated systems are presented followed by the results of the muon spin relaxation and Mössbauer spectroscopy experiments. In Sec. 7, I summarize my work and give an outlook.

2. Muon spin relaxation

Muon spin relaxation, usually abbreviated as μSR, is an experimental technique, which is used to study in particular magnetic and superconducting properties in condensed-matter systems. The μSR technique uses a 100 % spin-polarized muon beam to investigate the electronic properties of solid states. This chapter is organized in the following way: firstly, basic properties of the muon are described. Secondly, important experimental details are discussed. Thirdly, the interaction of the muon with the sample is discussed with focus on systems with magnetic order and/or superconductivity.

2.1. Muon properties

The muon belongs to the family of elementary fermions. A summary of its basic properties is shown in Tab. 2.1. In contrast to stable particles like electrons or protons, the muon radioactively decays with a mean lifetime of $\tau_\mu \approx 2.2$ μs. In nature, two muons exist. They can be distinguished by their charge: the positive muon has a charge of $q_{\mu^+} = +$e and the negative muon has a charge of $q_{\mu^-} = $-e with e being the elemental charge. Most other physical properties are equal for both types of muons. For purposes of condensed-matter physics, usually the positive muon is used. Therefore, all discussions in this thesis are referred to the positive muon. It carries a spin of $s_\mu = 1/2$. With a mass of $m_\mu \approx 105.7$ MeV/c^2, the muon is around 200 times heavier than an electron, which has a mass of $m_e \approx 511$ keV/c^2. The proton has a 9 times higher mass with $m_p \approx 938$ MeV/c^2 than the muon. For this reason, the positively charged muon is often called a light proton.

muon property	value
spin	1/2
charge	$\pm$e
mass	206.76826(11) m_e
	0.111609513(17) m_p
	105.658 3668(38) MeV/c^2
magnetic moment	3.18334547(47) μ_p
	$4.84 \cdot 10^{-3}$ μ_{B}
gyromagnetic ratio	$2\pi \cdot 135.5342(5)$ MHz/T
mean liftime	2.19703(4) μs

Table 2.1.: Basic properties of the muon in terms of electron and proton properties. m_p denotes the proton mass, m_e the electron mass, the elementary charge e, μ_p the magnetic moment of the proton and μ_{B} the Bohr magneton.

2.2. Muon production

Positive muons can be produced using a high-energy proton beam. In a synchrotron or cyclotron, protons will be accelerated to energies of $E > 500$ MeV and then directed on a target (usually carbon or beryllium). Via proton-proton (p-p) and proton-neutron (p-n) interactions in the target, positively charged pions π^+ are produced via the reactions

$$
\begin{aligned}
p + p &\to \pi^+ + d, \\
p + p &\to \pi^+ + p + n, \\
p + n &\to \pi^+ + n + n,
\end{aligned}
\tag{2.1}
$$

with deuterion d. The positive pion decays after a mean lifetime of $\tau_{\pi^+} \approx 26$ ns via

$$
\pi^+ \to \mu^+ + \nu_\mu
\tag{2.2}
$$

into a positive muon, which has an energy of ~ 4.1 MeV in the rest frame of the pion, and a muon-neutrino. For a deeper understanding of the properties of this decay, the helicity h is a useful quantity. A possible definition is

$$
h = 2\vec{s} \cdot \vec{e}_{\vec{p}},
\tag{2.3}
$$

where $\vec{s}$ describes the spin of the particle and $\vec{e}_{\vec{p}}$ is the momentum unit vector describing the direction of the momentum. The helicity operator has $2s+1$ eigenstates ranging from $-s$ to $+s$. For massless particles or, in a good approximation, particles with $v \approx$ c, where c denotes the speed of light in vacuum, only the eigenstates $+s$ and $-s$ are allowed. This is an important property for the muon neutrino. Its mass is not exactly known up to know, but to common knowledge, the muon neutrino travels with $v_\nu \approx$ c. Therefore, the eigenvalue of the helicity operator of $h_{\nu_\mu} = -1$ for the muon neutrino ν_μ (the muon anti-neutrino $\overline{\nu}_\mu$ has an eigenvalue of $+1$ for h) is obtained, resulting in a spin orientation antiparallel to the direction of the momentum.
The pion has a spin $s_{\pi^+} = 0$, while neutrino and muon are $s = 1/2$ - particles. Using the conservation of angular momentum

$$
\vec{s}_{\pi^+} = 0 = \vec{s}_{\nu_\mu} + \vec{s}_{\mu^+} = \frac{1}{2}\vec{e}_{s(\nu_\mu)} + \frac{1}{2}\vec{e}_{s(\mu^+)},
\tag{2.4}
$$

where $\vec{e}_s$ denotes the direction of the spins, results in an antiparallel alignment, $\vec{e}_{s(\nu_\mu)} || - \vec{e}_{s(\mu)}$, of the neutrino and muon spins. In the rest frame of the pion ($\vec{p}_{\pi^+} = 0$), both decay products have the same, but opposite momenta due to conservation of momentum:

$$
\vec{p}_{\pi^+} = 0 = \vec{p}_{\nu_\mu} + \vec{p}_\mu.
\tag{2.5}
$$

Taking into account the negative helicity of the muon neutrino, the muon spin is aligned antiparallel to its momentum. Due to this, a 100 % spin-polarized muon beam is produced.

2.3. Muon implantation

The muon enters the sample with a kinetic energy E_{kin} of ~ 4.1 MeV. E_{kin} is reduced to 2-3 keV within $10^{-10} - 10^{-9}$ s due to ionization effects and electron scattering. After another 10^{-13}s, the kinetic energy is reduced to a few hundred eV due to inelastic collisions with the atoms as well as through the creation of short-lived and unstable muonium states. As the muon is positively charged, it is repulsed by the also positively charged nuclei. Therefore, the muon tend to move to the minima of the electrostatic potential and come to rest at these interstitial sites. The muon interacts with the electrostatic potential leading to the so-called host-lattice relaxation, which changes the lattice constants by a few %. After coming to rest, the muon still has its initial spin polarisation, as the thermalization process is rapid and only electrostatic interactions occur.

2.4. Muon decay

The positive muon decays into a positron and two neutrinos with a mean lifetime of $\tau_\mu \approx 2.2$ ms via

$$\mu^+ \to e^+ + \nu_e + \overline{\nu}_\mu \tag{2.6}$$

into a positron e^+, an electron neutrino ν_e and a muon anti-neutrino $\overline{\nu}_\mu$. The kinetic energy of the positron varies up to a maximum energy of ≈ 52.83 MeV, depending on the momenta of the neutrinos. Positrons with the highest energies emerge, if the momentum of the positron is opposite to the momenta of the two neutrinos. As the helicity of both neutrinos is different ($h_{\overline{\nu}_\mu} = +1$ and $h_{\nu_e} = -1$), their spins are aligned antiparallel and adding up to zero. Therefore, muon and positron spin are pointing in the same direction. Due to the parity violation of the weak interaction, only chiral right-handed positrons ($h_{e^+} = +1$) are produced. Thus, the momentum of the muon is parallelly aligned to the spin direction. This causes an anisotropic distribution of the positron emission, as the positron is predominantly emitted along the muon spin direction. This distribution can be described by calculating the probability $\mathrm{d}W$ of the emission of a positron with energy $\mathrm{d}\varepsilon$ in the solid angle $\mathrm{d}\Omega$ using [6]

$$\frac{\mathrm{d}^2 W(\varepsilon, \varphi)}{\mathrm{d}\varepsilon\,\mathrm{d}\Omega} = \frac{3 - 2\varepsilon}{2\pi\tau_\mu}\varepsilon^2 \left[1 - \frac{1 - 2\varepsilon}{3 - 2\varepsilon}\cos(\varphi) \right], \tag{2.7}$$

where $\varepsilon = E_{\text{kin}}/E_{\text{max}}$ is the normalized positron energy, τ_μ the mean life time of the muon and φ the angle between the muon spin and the momentum of the emitted positron. Integration over all energies leads to the anisotropic emission probability [6]

$$\frac{\mathrm{d}W(\varphi)}{\mathrm{d}\Omega} = \frac{1}{4\pi\tau_\mu} \left[1 + \frac{1}{3}\cos(\varphi) \right]. \tag{2.8}$$

2.5. Experimental setup

There are, in principle, two types of setups for a μSR experiment: Continuous wave (CW) and pulsed muon sources. The former technique is used at the Paul Scherrer Institute

(PSI) in Villigen, Switzerland, and at the Tri-University Meson Facility (TRIUMF) in Vancouver, Canada. The latter technique is used at the ISIS in Oxford, United Kingdom, and at KEK and JPARC in Japan. As all μSR experiments of this PhD thesis were performed using the General Purpose Spectrometer (GPS) and DOLLY at PSI, only the CW situation is described. For informations about the pulsed muon sources, the interested reader is referred to the websites of the facilities.
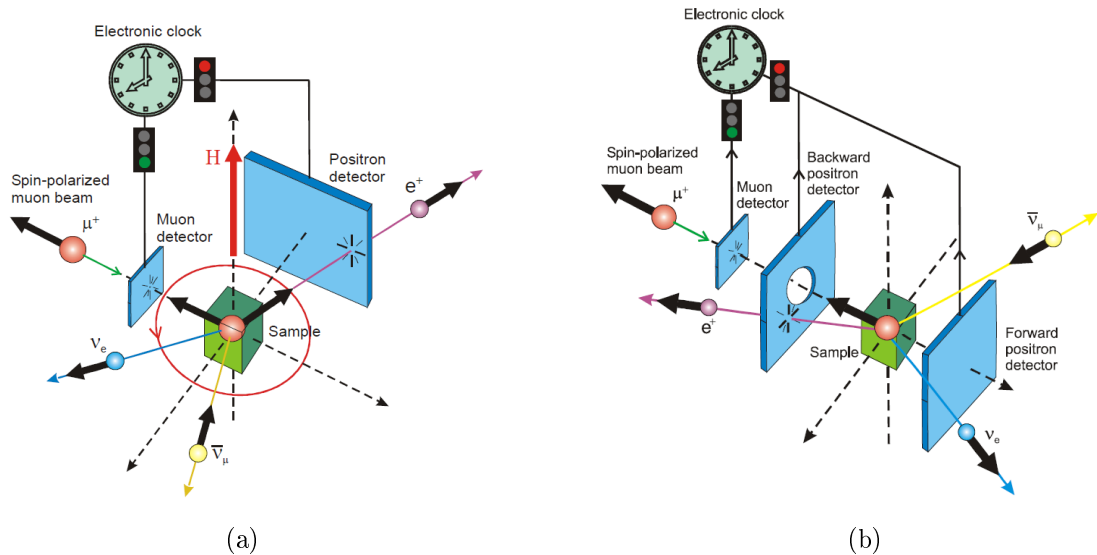

(a)   (b)

Figure 2.1.: Sketch of the experimental setup of a μSR experiment in (a) transversal and (b) zero field geometry. The red arrow denotes the direction of the applied external magnetic field $\vec{H}_{\text{ext}}$. μ^+ is the incident positive muon, e^+ is the emitted positron, ν_e the electron neutrino and $\overline{\nu}_\mu$ the muon anti-neutrino. Taken from Ref. [7].

In a CW experiment, single muons are implanted in the sample. An electronic clock measures the time between the implantation of the muon and the detection of the emitted positron in one of the detectors. The experiment is equipped with a so-called "veto system" to ensure, that only one single muon is measured at the same time.
After the implantation of the muon in the sample and its thermalisation within $< 10^{-9}$ s, the muon spin interacts with the electromagnetic environment. Afterwards, the muon decays and the positron is predominantly emitted in the direction of the muon spin. The decay positrons are detected as a function of time and solid angle, which is given by the detector position. The positron detection rate $\mathrm{d}n(t)/\mathrm{d}t$ is given by [6]

$$\frac{\mathrm{d}n(t)}{\mathrm{d}t} = \frac{\mathrm{d}W(\varphi)}{\mathrm{d}\Omega}N(t)\mathrm{d}\Omega, \tag{2.9}$$

where $\mathrm{d}\Omega$ is the solid angle covered by the positron detector, φ the angle between the detector axis and the initial muon spin polarisation $\vec{P}(0)$, and $N(t) = N_0\mathrm{e}^{-t/\tau_\mu}$. Using

Eq. (2.8) and Eq. (2.9), the detection rate is given by [6]

$$\frac{\mathrm{d}n(t)}{\mathrm{d}t} = \frac{1}{4\pi\tau_\mu}\left\{1 + \frac{1}{3}\vec{P}(t)\vec{e}_{\mu\Omega}\right\}N(t)\mathrm{d}\Omega, \tag{2.10}$$

where $\vec{e}_{\mu\Omega}$ is the unit vector pointing from the muon to the detector and, therefore, $\vec{P}(t)\vec{e}_{\mu\Omega}$ is the projection of the muon spin polarisation in this direction.

To extract the time-dependent asymmetry of the muon decay, the normalized difference in the detection rate of different detectors i,j is needed and is given by

$$A(t) = \frac{\frac{\mathrm{d}}{\mathrm{d}t}n_i(t) - \frac{\mathrm{d}}{\mathrm{d}t}n_j(t)}{\frac{\mathrm{d}}{\mathrm{d}t}n_i(t) + \frac{\mathrm{d}}{\mathrm{d}t}n_j(t)}. \tag{2.11}$$
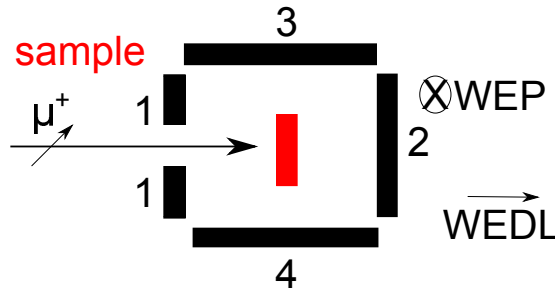

Figure 2.2.: Sketch of the GPS and DOLLY spectrometer. The detector pairs 3,4 and 2,1 as well as the implemented magnets WEP and WEDL are shown, where the arrows denote the direction of the magnetic field. The chosen muon spin direction, which is 45° rotated from the muon beam direction, is shown.

The detector arrangement at GPS is shown in Fig 2.2 with the detector pairs 3,4 and 2,1. By counting the number of positrons, which are measured in a time-interval $[t_n, t_{n+1}]$ after the muon implantation, a time histogram is recorded with $t_N = n\Delta t$, n=1, 2, 3, ... and Δt is the time resolution of the detector. The time dependence of the positron detection rate is described by these time histograms.

The asymmetry for two opposite detectors can be calculated using Eq. (2.11) and is given by

$$A(t) = A_0\vec{P}(t)\vec{e}_{\mu\Omega}, \tag{2.12}$$

where $A_0 = A(0)$ is the maximum asymmetry. By analysing the asymmetry $A(t)$, one can study the time evolution of the muon spin polarisation, $\vec{P}(t)$, in the sample, which is determined by the interaction of the muon spin with its electromagnetic environment.

In practice, there are experimental limitations. The maximum asymmetry is usually smaller than the theoretically expected 1/3 due to, for example, a finite solid angle.

2.6. Interaction of the muon with the sample

As the muon has a spin of 1/2, it does not couple to electric field gradients. Therefore, the spin Hamiltonian of the muon is determined by dipole-dipole and Fermi-contact inter-

actions. The Hamiltonian, which describes the magnetic interaction of the muon with its electromagnetic environment, is given by

$$\mathcal{H} = \mathcal{H}_{\text{dipol}} + \mathcal{H}_{\text{hf}} = -\gamma_\mu \hbar^2 \frac{\mu_0}{4\pi} \sum_i \gamma_{J_i} \left\{ \frac{3 \left[\vec{r}_i \vec{S}_\mu\right] \cdot \left[\vec{r}_i \vec{J}_i\right]}{r_i^5} - \frac{\vec{S}_\mu \vec{J}_i}{r_i^3} \right\} + \sum_i A_i \vec{S}_\mu \vec{J}_i, \quad (2.13)$$

where the first term describes the dipole-dipole interaction of the muon spin with nuclear and electronic magnetic moments $\gamma_{J_i} \hbar \vec{J}_i$. The second term describes the Fermi-contact interaction with conduction electrons, if the electrons have a non-zero magnetization at the muon site. γ_μ denotes the gyromagnetic ratio of the positive muon and γ_{J_i} of the spin $\vec{J}_i$. $\vec{r}_i$ is the position vector connecting the muon spin $\vec{S}_\mu$ and $\vec{J}_i$. A_i denotes the hyperfine coupling constant between the muon spin and the spin $\vec{J}_i$.

Under the assumption, that the perturbation of the electronic system of the solid state due to the muon is negligible small, the Hamiltonian can be written in a mean-field approximation:

$$\begin{aligned}
\mathcal{H} &= -\gamma_\mu \hbar \vec{S}_\mu \left\{ \hbar \frac{\mu_0}{4\pi} \sum_i \gamma_{J_i} \left[\frac{\vec{r}_i \left[\vec{r}_i \langle\vec{J}_i\rangle\right]}{r_i^5} - \frac{\langle\vec{J}_i\rangle}{r_i^3} \right] + \frac{1}{\hbar\gamma_\mu} \sum_i A_i \langle\vec{J}_i\rangle \right\} \\
&= -\gamma_\mu \hbar \vec{S}_\mu \left[\vec{B}_{\text{dip}} + \vec{B}_{\text{hf}} \right] \\
&= -\gamma_\mu \hbar \vec{S}_\mu \vec{B}_{\text{loc}}.
\end{aligned} \quad (2.14)$$

This approximation is valid for magnetic materials, where the magnetic exchange interaction of electronic magnetic moments is much larger than the dipole-dipole interaction of the muon with an electronic moment. For an understanding of the mean-field Hamiltonian, it is necessary to know the local magnetic field $\vec{B}_{\text{loc}}$ at the muon site.

In solids, the local magnetic field at the muon stopping site is a function of space and time $\vec{B}(\vec{r}, t)$. The space dependence is based on disorder and the dipole interaction of the muon spin with randomly oriented nuclear moments. It causes a dephasing of the muon spin precession. The time dependence is based on magnetic fluctuations and muon diffusion and results in a relaxation of the muon spin polarisation to thermal equilibrium.

The muons randomly stop at interstitial sites. As a result, the measured asymmetry and consequently $\vec{P}(t)$ is an ensemble average of the spatial variation of $\vec{B}_{\text{loc}}$. Instead of using the spatial variation of $\vec{B}_{\text{loc}}$, $\vec{P}(t)$ can be calculated using a finite distribution of the magnetic fields $n(\vec{B}_{\text{loc}})$ [8]:

$$\vec{P}(t) = \int \vec{P}'(\vec{B}_{\text{loc}}, t) n(\vec{B}_{\text{loc}}) \mathrm{d}\vec{B}_{\text{loc}}, \quad (2.15)$$

where $\vec{P}'(\vec{B}_{\text{loc}}, t)$ denotes the local muon spin polarisation. In the following chapters, the cases of static and dynamic magnetic field distributions as well as muon spin relaxation in

magnetically ordered systems are discussed.

2.6.1. Static relaxation

Static relaxation means, that the local magnetic field at the muon site does not change over the observation time, which is usually a few lifetimes τ_μ of the muon. This condition can be expressed as

$$\frac{B_{\mathrm{loc}}(t)}{\frac{\mathrm{d}}{\mathrm{d}t}B_{\mathrm{loc}}(t)} \gg \tau_\mu. \tag{2.16}$$

For a static isotropic Gaussian field distribution, which is given by

$$n(\vec{B}_{\mathrm{loc}}) = \left[\frac{\gamma_\mu}{\sqrt{2\pi}\sigma}\right]^3 \exp\left(-\frac{[\gamma_\mu B_{\mathrm{loc}}^x]^2}{2\sigma^2} - \frac{[\gamma_\mu B_{\mathrm{loc}}^y]^2}{2\sigma^2} - \frac{[\gamma_\mu B_{\mathrm{loc}}^z]^2}{2\sigma^2}\right), \tag{2.17}$$

with the standard deviation $\sigma = \sigma_x = \sigma_y = \sigma_z$, and under the assumption of $\vec{P}(t{=}0) = P_0\vec{e}_z$, Eq. (2.15) reduces to [6]

$$P_x(t) = P_y(t) = 0, \tag{2.18}$$

$$P_z(t) = \int \mathrm{d}B_{\mathrm{loc}}\mathrm{d}\theta\mathrm{d}\varphi \; n(\vec{B}_{\mathrm{loc}}) \left[\cos^2(\theta) + \sin^2(\theta)\cos(\gamma_\mu B_{\mathrm{loc}})\right] B_{\mathrm{loc}}^2, \tag{2.19}$$

where θ denotes the angle between the initial muon spin polarisation $\vec{P}(t{=}0)$ and the local magnetic field direction. The integration of Eq. (2.17) results in the static Gauss-Kubo-Toyabe function $G_{\mathrm{GKT}}(t,\sigma)$ [9]

$$P_z(t) = \frac{1}{3} + \frac{2}{3}\left[1 - \sigma^2 t^2\right] \mathrm{e}^{-\frac{1}{2}\sigma^2 t^2} = G_{\mathrm{GKT}}(t,\sigma). \tag{2.20}$$

This function is used to describe the influence of randomly oriented dense (nuclear) magnetic moments on the time evolution of the muon spin polarisation, where the assumption of isotropy is valid. For an isotropic Lorentz field distribution, which is given by

$$n(\vec{B}_{\mathrm{loc}}) = \frac{\gamma_\mu^3}{\pi^3}\frac{\lambda}{\gamma_\mu^2[B_{\mathrm{loc}}^x]^2 + \lambda^2} \cdot \frac{\lambda}{\gamma_\mu^2[B_{\mathrm{loc}}^y]^2 + \lambda^2} \cdot \frac{\lambda}{\gamma_\mu^2[B_{\mathrm{loc}}^z]^2 + \lambda^2}, \tag{2.21}$$

with $\lambda = \lambda_x = \lambda_y = \lambda_z$, the time evolution of the muon spin polarisation can be calculated under the assumption of $\vec{P}(t{=}0){=}P_0\vec{e}_z$ by using Eq. (2.15) resulting in [6]

$$P(t) = \frac{1}{3} + \frac{2}{3}[1 - \lambda t]\mathrm{e}^{-\lambda t} = G_{\mathrm{LKT}}(t,\lambda), \tag{2.22}$$

the static Lorentz-Kubo-Toyabe function $G_{\mathrm{LKT}}(t,\lambda)$. This function is used to describe the time evolution of the muon spin polarisation under the interaction of the muon spin with diluted (nuclear) magnetic moments. The time evolution of the muon spin polarisation for the Gauss-Kubo-Toyabe and Lorentz-Kubo-Toyabe function is shown in Fig. 2.3.
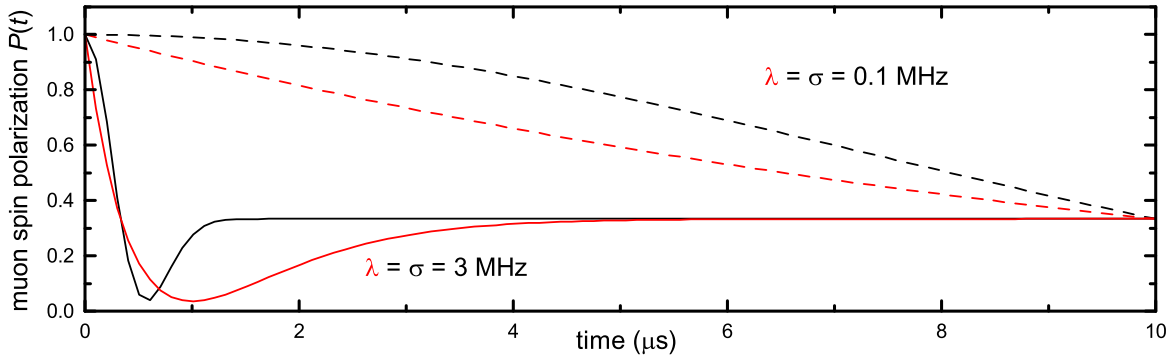
Figure 2.3.: Gauss-Kubo-Toyabe (black) and Lorentz-Kubo-Toyabe (red) function for relaxation rates of 0.1 MHz (dashed line) and 3 MHz (straight line).

2.6.2. Dynamic relaxation

Dynamic muon spin relaxation is caused by, e.g., muon diffusion or fluctuations of the internal magnetic field. This non-static behaviour can be modelled by the strong-collision approximation [9]. The muons experience a fluctuation of the magnetic field B after a characteristic time τ_c, or the magnetic field fluctuates with a frequency of $\nu = 1/\tau_c$, respectively. In the strong-collision model, the magnetic field values before and after the fluctuation are treated as independent, which corresponds to a first-order Markov process [9]. Before the first fluctuation, the muons experience a static field B_0 and hence the time evolution of the muon spin polarisation exhibits a static depolarisation $P_S(t)$. The probability of observing no fluctuation after a time t is given by [9]

$$p_0(t) = \mathrm{e}^{-\frac{t}{\tau_c}} P_S(t). \tag{2.23}$$

The probability of having one fluctuation at a time $t \in (0,t')$ is given by [9]

$$p_1(t) = \frac{1}{\tau_c} \int_0^\infty \mathrm{d}t' \ \mathrm{e}^{-\frac{t-t'}{\tau_c}t} P_S(t-t')\mathrm{e}^{-\frac{t'}{\tau_c}} P_S(t) \tag{2.24}$$

and of n fluctuations at a time $t \in (0,t')$ by [9]

$$p_n(t) = \frac{1}{\tau_c} \int_0^t \mathrm{d}t' \ p_{n-1}(t-t')\mathrm{e}^{-\frac{t'}{\tau_c}} P_S(t). \tag{2.25}$$

Consequential, the time evolution of the muon spin polarisation including all possible fluctuation channels is given by [9]

$$P(t) = \sum_n^\infty p_n(t). \tag{2.26}$$

This expression can be evaluated for any internal field distribution resulting in the dynamic Kubo-Toyabe function. For an isotropic Gaussian field distribution with a standard

deviation σ, slow fluctuations, $\sigma\tau_c \gg 1$, lead to an exponentially damped 1/3 - tail with a damping rate $\lambda = 2/3\tau_c$. In the limit of fast fluctuations, $\sigma\tau_c \ll 1$, an overall exponential depolarisation,

$$P(t) = \mathrm{e}^{-\lambda\tau_c}, \qquad \lambda = 2\sigma^2\tau_c \tag{2.27}$$

is obtained.

2.6.3. Magnetic order

Assuming an ideal crystal lattice, long-range commensurate magnetic order of electronic moments creates a well-defined finite magnetic field at the muon site, which can be described by $n(\vec{B}_{\mathrm{loc}}) = \delta(\vec{B}_0 - \vec{B}_{\mathrm{loc}})$ with the Dirac delta function $\delta(B)$. Applying this field distribution $n(\vec{B}_{\mathrm{loc}})$ on Eq. (2.15) results in a general expression for the relaxation and, therefore, the time evolution of the muon spin polarisation is given by [6]

$$P(t) = \cos^2(\theta) + \sin^2(\theta)\cos(\gamma_\mu B_0 t). \tag{2.28}$$

For an isotropic internal-field distribution, $P(t)$ can be expressed by

$$P(t) = \frac{1}{3} + \frac{2}{3}\cos(\gamma_\mu B_0 t), \tag{2.29}$$

after averaging over all spatial directions θ. This is, for example, the case in a powder sample.

In real systems a distribution of local fields is often found. For an isotropic Lorentz distribution

$$n(\vec{B}_{\mathrm{loc}}) = \frac{\gamma_\mu^3}{\pi^3} \frac{\lambda}{\gamma_\mu^2[B_{\mathrm{loc}}^x]^2 + \lambda^2} \cdot \frac{\lambda}{\gamma_\mu^2[B_{\mathrm{loc}}^y]^2 + \lambda^2} \cdot \frac{\lambda}{\gamma_\mu^2[B_{\mathrm{loc}}^z]^2 + \lambda^2}, \tag{2.30}$$

with $\lambda = \lambda_x = \lambda_y = \lambda_z$, Eq. (2.15) gives [10]

$$P(t) = \frac{1}{3} + \frac{2}{3}\left\{\cos(2\pi f_\mu t) - \frac{\lambda}{2\pi f_\mu}\sin(2\pi f_\mu t)\right\}\mathrm{e}^{-\lambda t}, \tag{2.31}$$

with $2\pi \times f_\mu = \gamma_\mu|\vec{B}_0|$. For $\lambda/2\pi f_\mu \ll 1$, Eq. (2.31) reduces to

$$P(t) = \frac{1}{3} + \frac{2}{3}\cos(2\pi f_\mu t)\mathrm{e}^{-\lambda t}, \tag{2.32}$$

which is a commonly used equation to analyse the time evolution of the muon spin polarisation in magnetically ordered systems.

For an ideal commensurate magnetic structure, one value of B_{loc} is expected. In contrast, for an incommensurate magnetic structure, any number of magnetically inequivalent muon sites is possible. Assuming a periodical field modulation, e.g. a spin-density wave, results in $\vec{B} = \vec{B}_{\mathrm{max}}\cos(\vec{q}\vec{r})$, where B_{max} is the maximum magnetic field, $\vec{q}$ the wave vector and $\vec{r}$ the position vector. This field modulation results in the magnetic field distribution

2. Muon spin relaxation

[11]

$$n(B) = \frac{2}{\pi} \frac{1}{\sqrt{B_{\text{max}}^2 - B^2}}, \tag{2.33}$$

which is the so-called Overhauser form of the spin density wave. Applying this field distribution to Eq. (2.15) gives the corresponding time evolution of the muon spin polarisation

$$P(t) = \frac{1}{3} + \frac{2}{3} J_0(\gamma_\mu B_{\text{max}} t), \tag{2.34}$$

where J_0 is the 0th-order Bessel function. $P(t)$ has the same structure as in the case of static commensurate magnetic order. Only the form of the oscillation is different, which is illustrated in Fig. 2.4. The sinusoidal oscillation shows no damping, while the Bessel-oscillation shows a strong damping.
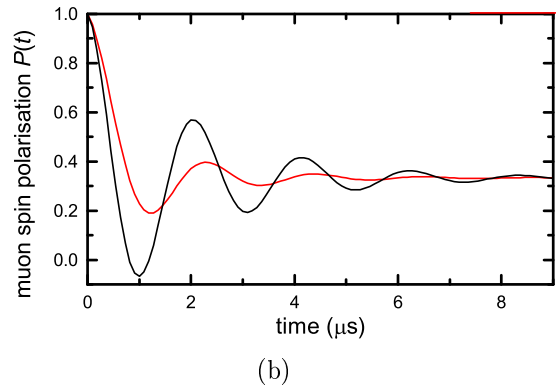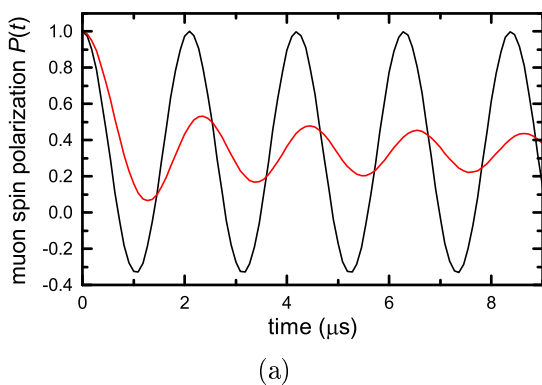
Figure 2.4.: time evolution of the muon spin polarisation $P(t)$ with a sinusoidal (black) or Bessel (red) oscillation for the undamped (a) and damped (b) case. The exponential relaxation in (b) has a relaxation rate $\lambda = 0.5$ MHz.

In single crystals, the situation is different, as the local field has a fixed, yet arbitrary orientation. A useful approach is to introduce variable parameters a_1 and a_2 as well as a phase ϕ leading to the expression [6]

$$P(t) = a_1 + a_2 \cos(2\pi f_\mu t + \phi) e^{-\lambda t}, \tag{2.35}$$

where a_1 and a_2 are not connected in a simple way.

$P(t)$ for the case of N magnetically inequivalent muon stopping sites can be expressed by

$$P(t) = \sum_i^N p_i \left\{ a_{1,i} \cos(2\pi f_{\mu,i} t + \phi) e^{-\lambda_{\text{T},i} t} + a_{2,i} e^{-\lambda_{\text{L},i} t} \right\}, \tag{2.36}$$

where p_i denotes the occupation probability of the different muons site with $\sum_i^N p_i = 1$. The exponential damping of the tail a_2 is modeled by the (longitudinal) exponential damping rate λ_{L}. This exponential damping is, however, a result of dynamic magnetic field fluctuations.

It is possible with μSR to determine the magnetic volume fraction of a sample. In a temperature region, where not 100 % of the sample is magnetically ordered, a certain amount of the muons show a depolarisation of $P(t)$ due to the interaction of the muon spin with randomly oriented nuclear magnetic moments only. The rest of the muons stops in sample volumes, which are magnetically ordered and, therefore, $P(t)$ shows a depolarisation following Eq. (2.36). To separate this signal fractions, the following equation can be used:

$$P(t) = V_{\mathrm{mag}} \sum_{i}^{N} p_i \left\{ a_{1,i} \cos(2\pi f_{\mu,i} t + \phi) \mathrm{e}^{-\lambda_{\mathrm{T},i} t} + a_{2,i} \mathrm{e}^{-\lambda_{\mathrm{L},i} t} \right\}$$
$$+ [1 - V_{\mathrm{mag}}] G_{\mathrm{GKT}}(t, \sigma_{\mathrm{nm}}), \tag{2.37}$$

where V_{mag} denotes the magnetic volume fraction and dense nuclear moments are assumed.

Another possibility to measure the magnetic volume fraction is to apply a weak external transverse field B_{TF}. $P(t)$ then is given by

$$P(t) = V_{\mathrm{mag}} \left\{ a_1 + a_2 \cos(2\pi f_\mu) \mathrm{e}^{-\lambda t} \right\} + [1 - V_{\mathrm{mag}}] \cos(\gamma_\mu B_{\mathrm{TF}} t). \tag{2.38}$$

Muons, which stop in a paramagnetic sample volume interact with the external magnetic field and, therefore, perform a precession with a frequency $2\pi \times f_{\mathrm{TF}} = \gamma_\mu B_{\mathrm{TF}}$. Muons, which stop in a magnetically ordered sample volume only experience the internal local field B_{loc}, if $B_{\mathrm{TF}} \ll B_{\mathrm{loc}}$. Consequently, the magnetic volume fraction is given by the relative amount of muons precessing with a frequency f_{TF}.

2.7. μSR in type-II superconductors

As described in Sec. 2.6, μSR is a suitable tool to measure the shape of the magnetic field distribution inside a sample. This can be used to investigate the Shubnikov phase of a type-II superconductor.
By applying an external magnetic field B_{ext} with $B_{c1} < B_{\mathrm{ext}} < B_{c2}$ at temperatures below the superconducting transition temperature, T_c, a vortex lattice is formed. B_{c1} is the lower and B_{c2} the upper critical field of the superconductor. The Gibbs free energy G_s for the case of an inhomogeneous superconductor, e.g. including spatial variation of the superconducting order parameter, $|\psi(\vec{r})|^2$, in an applied magnetic field $\vec{B}_{\mathrm{ext}}$ is given by

$$G_s[\psi, \vec{A}] = G_n + \alpha |\psi(\vec{r})|^2 + \frac{\beta}{2} |\psi(\vec{r})|^4 + \frac{1}{2\mu_0} \left| \vec{B}_{\mathrm{ext}} - \vec{B}_i \right|^2 + \frac{1}{2m_s} \left| \left[-i\hbar \vec{\nabla} - q_s \vec{A} \right] \psi \right|^2, \tag{2.39}$$

where the Gibbs free energy is a functional of ψ and the vector potential $\vec{A}$. q_s is the charge and m_s the mass of the superconducting charge carriers. G_n denotes the Gibbs free energy of the normal state. The term $\frac{1}{2\mu_0} \left| \vec{B}_{\mathrm{ext}} - \vec{B}_i \right|^2$ describes the energy, which is needed to expel the magnetic field from the superconductor up to a residual field of $\vec{B}_i$. This energy is maximal in the case of the Meissner-phase ($\vec{B}_i = 0$). Minimizing the Gibbs

free energy functional with respect to ψ^* results in the first Ginzburg-Landau equation

$$\alpha\psi(\vec{r}) + \beta|\psi(\vec{r})|^2\psi(\vec{r}) + \frac{1}{2ms}\left|\left[-i\hbar\vec{\nabla} - q_s\vec{A}\right]\psi\right|^2 = 0. \qquad (2.40)$$

To obtain the superconducting order parameter $|\psi(\vec{r})|^2$ and the magnetic field $\vec{B}(\vec{r}) = \vec{\nabla}\times\vec{A}$ near a vortex core, the first Ginzburg-Landau equation as well as Ampère's law,

$$\mu_0\vec{j} = \vec{\nabla}\times\vec{B} = \mu_0\frac{iq_s\hbar}{2m_s}\left\{\psi^*\vec{\nabla}\psi - \psi\vec{\nabla}\psi^*\right\} - \frac{q_s}{m_s}|\psi|^2\vec{A} \qquad (2.41)$$

has to be solved. This is quite complicated and results in no analytical expression due to the $\beta|\psi(\vec{r})|^2\psi(\vec{r})$ term in Eq. (2.40). The result of a numerical integration for a single vortex is shown in Fig. 2.5.
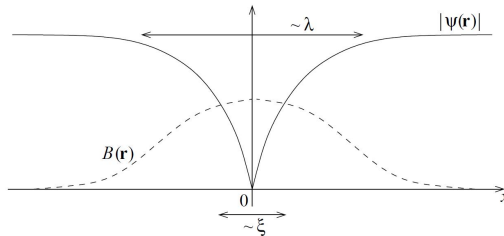
Figure 2.5.: Spatial dependence of $|\psi(\vec{r})|$ and the magnetic field $B(\vec{r})$ near a vortex core. Picture taken from Ref. [12].

$\psi(\vec{r})$, and hence $|\psi(\vec{r})|^2$, are zero at the vortex core. $\psi(\vec{r})$ increases with increased distance from the vortex core. The coherence length ξ determines the typical length scale, on which the superconducting order parameter reaches his full value. The magnetic field has a finite value near the core with a maximum value at the core. With increased distance from the vortex core, the magnetic field decreases on a length scale of the London penetration depth λ.

By knowing, in principle, the spatial dependence of the magnetic field near a single vortex, on can calculate the magnetic field at each point of a vortex lattice by summing up all vortices. As this magnetic field in the superconductor has spatial variations, one can calculate a internal magnetic field distribution $n(B)$.

The vortices usually arrange in a triangular lattice with a hexagonal unit cell. The position vector of a vortex in the hexagonal arrangement, under the assumption of $\vec{B}_{ext} = B_{ext}\vec{e}_z$, is given by

$$\vec{r} = \frac{d}{2}\left\{[2m + n]\vec{e}_x + \sqrt{3}n\vec{e}_y\right\}, \qquad (2.42)$$

with $m,n\in\mathbb{Z}$ and the unit vectors $\vec{e}_x$ and $\vec{e}_y$ along the x- and y-axis. Therefore, the vortex lattice is located in a plane perpendicular to the applied external magnetic field. The inter-vortex spacing d is given by

$$d = \sqrt{\frac{2\Phi_0}{\sqrt{3}\langle B\rangle}}, \qquad (2.43)$$

where $\langle B \rangle$ denotes the average local magnetic field and Φ_0 the magnetic flux quantum. The magnetic field can be calculated using the Fourier expansion:

$$B_z(\vec{r}) = \langle B \rangle \sum_{\vec{G}} e^{-i\vec{G}\vec{r}} B_{\vec{G}}(\lambda, \xi), \tag{2.44}$$

where $\vec{G}$ denotes the reciprocal lattice vector and is given by

$$\vec{G} = \frac{2\pi}{d} \left\{ m\vec{e}_x - \frac{1}{\sqrt{3}}[m + 2n]\vec{e}_y \right\}, \tag{2.45}$$

with $m,n \in \mathbb{Z}$. Applying this calculations on a single crystal transforms the coordinate system from Fourier to real space like $(x,y,z)^{\mathrm{T}} \longmapsto (a,b,c)^{\mathrm{T}}$ with the crystallographic a-, b-, and c-axis. Then $\vec{r}$ denotes the position vector, as described in Eq. (2.42), in the ab-plane, which is perpendicular to the applied external field $\vec{B}_{\mathrm{ext}} = B_{\mathrm{ext}}\vec{e}_z$, which is applied along the crystallographic c-axis. $B_{\vec{G}}(\lambda, \xi)$ are the corresponding Fourier coefficients. For small applied fields, $B_{c1} < B_{\mathrm{ext}} \ll B_{c2}$, and $\lambda_{ab} \gg \xi_{ab}$, $B_{\vec{G}}(\lambda, \xi)$ is given by [13]

$$B_{\vec{G}}(\lambda, \xi) = \frac{e^{-\frac{1}{2}\xi_{ab}^2 G^2}}{1 + G^2\lambda_{ab}^2}, \tag{2.46}$$

including a Gaussian cut-off, which is introduced to suppress the divergence of $B_z(\vec{r})$ for $r \to 0$. Taking the field-dependence of the order parameter into account, Eq. (2.46) becomes [14, 15]

$$B_{\vec{G}}(\lambda, \xi) = \frac{e^{-\frac{1}{2}\frac{\xi_{ab}^2 G^2}{1-b}}}{1 + \frac{G^2\lambda_{ab}^2}{1-b}} \tag{2.47}$$

with the reduced field $b = \langle B \rangle / B_{c2}$.

The probability distribution $n(B)$ inside the Shubnikov phase for a perfect flux-line lattice can be calculated from the known spatial variation of the internal magnetic field $B_0(\vec{r})$ using

$$n_0(B) = \frac{\int \mathrm{d}r^3 \, \delta(B - B_0(\vec{r}))}{\int \mathrm{d}r^3}, \tag{2.48}$$

where $\delta(x)$ is the Dirac delta function and is shown in Fig. 2.6.

The corresponding time evolution of the muon spin polarisation with $\vec{B}_{\mathrm{ext}} = B_{\mathrm{ext}}\vec{e}_z$ and $\vec{P}(0) = \vec{e}_x$ is given by

$$P_x(t) = \int_0^\infty \mathrm{d}B \, n(B) \cos(\gamma_\mu B t). \tag{2.49}$$

Vortex disorder

The ideally (unperturbed) flux-line lattice results in a magnetic field distribution, which is described by Eq. (2.48) with a periodic field $B_0(\vec{r})$. In a non-perfect vortex lattice with
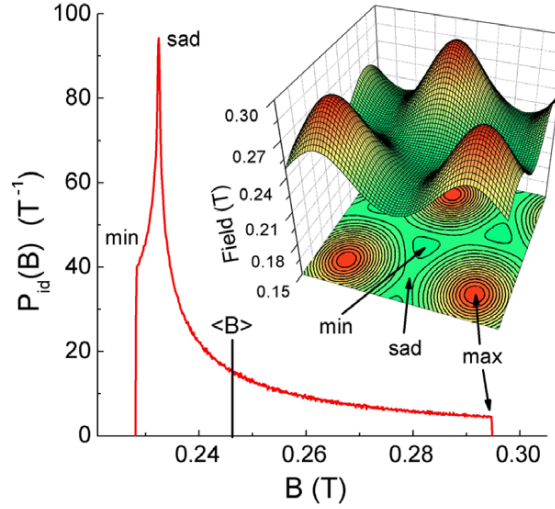
Figure 2.6.: Spatial dependence of the magnetic field and magnetic field distribution $P(B)$ for an ideal hexagonal vortex lattice, calculated by using Eq. (2.47) and (2.48), respectively. $\lambda = 50$ nm, $\xi = 20$ nm, $\langle B \rangle = 246.8$ mT, $b = 0.3$, and $d = 69.5$ nm are used. Picture taken from [16].

random perturbations of the flux-lines, the magnetic field is given by

$$B(\vec{r}) = B_0(\vec{r}) + \delta B(\vec{r}), \qquad (2.50)$$

with the field perturbation $\delta B(\vec{r})$, which results in a general expression for the magnetic field distribution [17]

$$n(B) = \frac{\int \mathrm{d}r^3 \; p(B - B_0(\vec{r}); \vec{r})}{\int \mathrm{d}r^3} = \frac{\int \mathrm{d}r^3 \; p(\delta B(\vec{r}); \vec{r})}{\int \mathrm{d}r^3}, \qquad (2.51)$$

where $p(\delta B(\vec{r}); \vec{r})$ is the probability to find the deviation δB at the position $\vec{r}$. As $B_0(\vec{r})$ is a periodic function of the flux-line lattice, one may replace the dependence of $p(B - B_0(\vec{r}); \vec{r})$ from $\vec{r}$ by a dependence of the periodic field value, which leads to [17]

$$n(B) = \frac{\int \mathrm{d}r^3 \; p(B - B_0(\vec{r}); B_0(\vec{r}))}{\int \mathrm{d}r^3}. \qquad (2.52)$$

For small perturbations, i.e., $B \approx B_0$, Eq. (2.52) becomes

$$n(B) = \frac{\int \mathrm{d}r^3 \; p(B - B_0(\vec{r}); B(\vec{r}))}{\int \mathrm{d}r^3}. \qquad (2.53)$$

This equation can be expressed in a more enlightening way [17]:

$$n(B) = \int \mathrm{d}\delta B \; p(\delta B(\vec{r}); B(\vec{r})) \; n_0(B - \delta B). \qquad (2.54)$$

Therefore, for small perturbations δB, the magnetic field distribution $n(B)$ is given by a convolution of the unperturbed magnetic field distribution $n_0(B)$ of the perfect flux-line lattice with a function, which describes the perturbation of the vortices. For the case of randomly weak perturbed vortices, the function $p(\delta B(\vec{r}); B(\vec{r}))$ is approximated with a Gaussian distribution [17],

$$p(\delta B, B) = \frac{1}{\sqrt{2\pi}\sigma(B)} \exp\left(-\frac{1}{2} \frac{\delta B^2}{\sigma_{\mathrm{VD}}(B)^2} \right), \tag{2.55}$$

with a field-dependent standard deviation $\sigma_{\mathrm{VD}}(B)$ due to the vortex disorder. This leads to the magnetic field distribution

$$n(B) = \frac{1}{\sqrt{2\pi}\sigma_{\mathrm{VD}}(B)} \int \mathrm{d}(\delta B)\, n_0(B - \delta B) \exp\left(-\frac{1}{2} \frac{\delta B^2}{\sigma_{\mathrm{VD}}(B)^2} \right) \tag{2.56}$$

which is a convolution of the unperturbed magnetic field distribution with a Gaussianly distributed perturbation. The time evolution of the muon spin polarisation $P(t)$ and the magnetic field distribution $n(B)$ are connected via a Fourier transformation. Using the property of the Fourier transformation, that the Fourier transform of any convolution is the product of the Fourier transformations of the original functions, under the assumption of a field-independent $\sigma(B)$, $P(t)$ is given by

$$P_x(t) = \mathrm{e}^{-\frac{1}{2}\sigma_{\mathrm{VD}}^2 t^2} \int_0^\infty \mathrm{d}B\, n_0(B) \cos(\gamma_\mu B t). \tag{2.57}$$

with $\vec{B}_{\mathrm{ext}} = B_{\mathrm{ext}}\vec{e}_z$ and $\vec{P}(0) = \vec{e}_x$ (as in Eq. (2.49)).

To investigate $P_x(t)$, it is often assumed, that $n(B)$ is a sum of N Gaussian distributions [16], which leads to

$$P_x(t) = \sum_i^N \left\{ p_i \cdot \cos(\gamma_\mu B_i t + \varphi) \cdot \mathrm{e}^{-\frac{1}{2}\sigma_i^2 t^2} \right\} \cdot \mathrm{e}^{-\frac{1}{2}\sigma_{\mathrm{VD}}^2 t^2} \mathrm{e}^{-\frac{1}{2}\sigma_{\mathrm{N}}^2 t^2}, \tag{2.58}$$

where σ_{VD} is the relaxation rate due to the vortex disorder. σ_{N} is the relaxation rate due to the dipole-dipole interaction of the muon spin with randomly oriented nuclear moments. p_i is the weighting of the N single Gaussian distributions with $\sum_i^N p_i = 1$ and φ the initial phase of the muon beam. B_i is the first moment and σ_i the relaxation rate of the ith Gaussian component. The corresponding magnetic field distribution is given by

$$n(B) = \frac{1}{\sqrt{2\pi}} \sum_i^N \frac{p_i}{\sigma_i} \exp\left(-\gamma_\mu^2 \frac{[\langle B \rangle - B_i]^2}{2\sigma_i^2} \right), \tag{2.59}$$

with the first moment $\langle B \rangle$. By analysing the time evolution of the muon spin polarisation in the superconducting state using Eq. (2.58), the total magnetic field distribution is obtained.

2. Muon spin relaxation

The first moment of this distribution is given by

$$\langle B \rangle = \sum_i^N p_i B_i \tag{2.60}$$

and the second moment by [16]

$$\langle \Delta B^2 \rangle_t = \sum_i^N p_i \left\{ \left[\frac{\sigma_i}{\gamma_\mu} \right]^2 + [B_i - \langle B \rangle]^2 \right\}. \tag{2.61}$$

This second moment is composed of the second moment of the magnetic field distribution as well as contributions from the vortex disorder and the nuclear magnetic moments [16]:

$$\langle \Delta B^2 \rangle_t = \langle \Delta B^2 \rangle + \left[\frac{\sigma_{\mathrm{VD}}}{\gamma_\mu} \right]^2 + \left[\frac{\sigma_{\mathrm{N}}}{\gamma_\mu} \right]^2. \tag{2.62}$$

The contribution from the nuclear magnetic moments can be measured at temperatures above the superconducting transition temperature. Unfortunately, it is not possible to separate $\langle \Delta B^2 \rangle$ and $\sigma_{\mathrm{VD}}^2 / \gamma_\mu^2$ in the course of a multi-Gaussian analysis of $P(t)$. Taking into account, that the second moment $\langle \Delta B^2 \rangle$ is related to the magnetic penetration depth by [13]

$$\frac{1}{\lambda^2} = \sqrt{\frac{\langle \Delta B^2 \rangle}{C}}, \tag{2.63}$$

λ can be calculated using the approximation $\sigma_{\mathrm{VD}} = \beta / \lambda^2$ [16]:

$$\lambda = \left[\frac{1}{C} \frac{\gamma_\mu^2 + C\beta^2}{\gamma_\mu^2 \langle \Delta B^2 \rangle_t - \sigma_{\mathrm{N}}^2} \right]^{0.25}. \tag{2.64}$$

By setting $\beta = 0$, vortex disorder is neglected and, therefore, the calculated value for λ is a lower boundary. For the calculation of C, a useful approximation is given by Brand [13]:

$$C = 7.5 \cdot 10^{-4} [1 - b]^2 \left[1 + 3.9[1 - b^2] \right] \Phi_0, \tag{2.65}$$

where Φ_0 is the magnetic flux quantum and $b = \langle B \rangle / B_{c2}$.

Temperature dependence of the London penetration depth λ_{LPD}

The London penetration depth λ_{LPD} is related to the superfluid density n_s via

$$\lambda_{\mathrm{LPD}} = \sqrt{\frac{m_s}{\mu_0 n_s q_s^2}}, \tag{2.66}$$

where m_s is the mass and q_s the charge of the superfluid charge carriers. Eq. (2.66) describes λ_{LPD} for a perfect superconductor. Impurities and non-local effects can change λ_{LPD}. To connect the London penetration depth λ_{LPD} with the measured magnetic penetration depth, λ, λ_{LPD} has to be related to the quasiparticle mean-free path l and the

coherence length ξ. In the clean local (or London) limit with $\lambda_{\mathrm{LPD}} \gg l \gg \xi$, λ_{LPD} and λ are of equal value. This limit is valid for high-temperature superconductors [18]. In the dirty local limit, taking impurity scattering into account, with $\lambda_{\mathrm{LPD}} \gg l \approx \xi$, the measured λ is enhanced compared to λ_{LPD} and is given by [19]

$$\lambda = \lambda_{\mathrm{LPD}} \sqrt{1 + \frac{\xi}{l}}, \qquad (2.67)$$

which is appropriate for alloy superconductors [18]. In the extreme dirty limit with $l \ll \xi$, the measured magnetic penetration depth is given by [19]

$$\lambda = \lambda_{\mathrm{LPD}} \sqrt{\frac{\xi}{l}}. \qquad (2.68)$$

Non-local effects occur for $\xi \gg \lambda_{\mathrm{LPD}}$. They are described within the phenomenological Pipard model. The enhancement is given by [19]

$$\lambda \approx \left[\lambda_{\mathrm{LPD}}^2 \xi\right]^{\frac{1}{3}}. \qquad (2.69)$$

Therefore, the real values of the magnetic penetration depth λ may differ from λ_{LPD}. Apart from that, informations about the size, the number and the symmetry of the superconducting gaps can be obtained by the temperature dependence of $\lambda(T)$. The temperature dependence of the magnetic penetration depth λ can be calculated for a single isotropic gap $\Delta(T)$ by [19]

$$\frac{\lambda^2(0)}{\lambda^2(T)} = 1 - 2 \int_{\Delta(t)}^{\infty} \mathrm{d}E \left[-\frac{\partial n_{\mathrm{F}}(E)}{\partial E}\right] \frac{E}{\sqrt{E^2 - \Delta^2(T)}} = 1 + D(\Delta, T), \qquad (2.70)$$

where $n_{\mathrm{F}}(E)$ is the Fermi-Dirac distribution and $\frac{E}{\sqrt{E^2-\Delta^2(T)}}$ is the density of states. In general, no analytical expression for the temperature dependence of the superconducting gap is specifiable. $\Delta(T)$ can be calculated by self-consistently solving the gap equation

$$\int_0^{\infty} \mathrm{d}E \left\{ \frac{\tanh\left(\frac{1}{2k_{\mathrm{B}}T}\sqrt{E^2 + \Delta^2}\right)}{\sqrt{E^2 + \Delta^2}} - \frac{1}{E} \tanh\left(\frac{E}{2k_{\mathrm{B}}T_c}\right) \right\} = 0, \qquad (2.71)$$

with Boltzmann's constant k_{B} and the superconducting transition temperature T_c. Alternatively, an appropriate approximation can be used, which is, for example, given by [20]

$$\Delta(T) = 1.76\Delta(0) \tanh\left(1.82 \left[1.018 \frac{T_c - T}{T}\right]^{0.51}\right). \qquad (2.72)$$

For numerical convenience, the integral in Eq. (2.70) may be approximated by [21]

$$D(\Delta, T) = -2 \int_{\Delta(T)}^{\infty} \mathrm{d}E \left[-\frac{\partial n_F}{\partial E} \right] \frac{E}{\sqrt{E^2 - \Delta^2(T)}}$$
$$\approx \left[\cosh \left(\frac{\Delta(T)}{2k_B T} \right) \right]^{-2} \sqrt{\frac{\pi \Delta(T)}{8k_B T} + \frac{1}{1 + \frac{\pi \Delta(T)}{8k_B T}}}. \tag{2.73}$$

Eq. (2.70) describes the dependence of the magnetic penetration depth from one single superconducting gap. Multiband superconductors such as MgB_2 or the iron pnictides may have more than one gap, and theses gaps may have different sizes. In this case, the temperature dependence of the different gaps should be calculated using the Eliashberg theory [20]. In the limit of non-interacting bands, however, one can treat the superconducting gaps within a phenomenological α model [20–22]

$$\frac{\lambda^2(0)}{\lambda^2(T)} = w[1 - D(\Delta_1, T)] - [1 - w] \cdot [1 - D(\Delta_2, T)], \tag{2.74}$$

where w is a phenomenological weighting factor of the two gaps. $D(\Delta_i, T)$ is given by Eq. (2.73) and $\Delta(T)$ by Eq. (2.72).

3. Mössbauer spectroscopy

3.1. Introduction

The recoil energy-free nuclear resonance fluorescence spectroscopy, which is often called Mössbauer spectroscopy, was discovered by Rudolph Mössbauer who received the physics Nobel price in 1961 [23]. The Mössbauer spectroscopy technique uses the transition between an excited and the ground state of a nucleus to investigate the electromagnetic properties of its environment. The most often used nucleus, also exclusively in this thesis, is ^{57}Fe. Therefore, the theoretical descriptions in this chapter are referred to ^{57}Fe.

This chapter is organized in the following way: First, a semi-classical description of the resonance absorption (Sec. 3.2) is given followed by a quantum mechanical treatment (Sec. 3.3-3.5). Secondly, the hyperfine interaction of the nucleus with its electromagnetic environment is discussed in Sec. 3.6.

3.2. The Mössbauer effect

The energy of a free ^{57}Fe nucleus in the first excited state, before the emission of a photon, is given by

$$E_i = E_{\text{es}} + \frac{\vec{p}^2}{2M}, \tag{3.1}$$

where E_{es} denotes the energy of the excited spin $\frac{3}{2}^-$ state, $\vec{p}$ the momentum and M the mass of the ^{57}Fe nucleus. The energy of a ^{57}Fe nucleus after the emission of a photon is given by

$$E_f = E_{\text{gs}} + \frac{\left[\vec{p} - \hbar\vec{k}_\gamma\right]^2}{2M}, \tag{3.2}$$

where E_{gs} denotes the energy of the spin $\frac{1}{2}^-$ ground state and $\vec{k}_\gamma$ the momentum of the photon. Therefore, the energy E_γ of the emitted photon can be calculated by using the Eq. (3.1) and (3.2):

$$E_\gamma = E_i - E_f := \hbar\omega = \hbar\omega_0 + \hbar\vec{k}_\gamma \frac{\vec{p}}{M} - \frac{\hbar^2 \vec{k}^2}{2M}, \tag{3.3}$$

with $E_{\text{es}} - E_{\text{gs}} = \hbar\omega_0 = 14.4$ keV. The absorption of a photon can be treated analogously, leading to

$$E_\gamma = E_i - E_f := \hbar\omega = \hbar\omega_0 + \hbar\vec{k}_\gamma \frac{\vec{p}}{M} + \frac{\hbar^2 \vec{k}^2}{2M}. \tag{3.4}$$

3. Mössbauer spectroscopy

In the rest frame of the nucleus, the energy of the photon is given by

$$E_\gamma = \hbar\omega_0 \pm \underbrace{\frac{\hbar^2 \vec{k}_\gamma^2}{2M}}_{E_\mathrm{R}} \tag{3.5}$$

and is shifted by the recoil energy E_R compared to the bare transition energy $\hbar\omega_0$. Therefore, the nucleus, which absorbs the photon, will gain E_R. This results in a separation of the two transition lines (absorption and emission) by $2E_\mathrm{R}$.
A nuclear state has an energy uncertainty Γ_nat, which is connected to its mean lifetime τ over

$$\Gamma_\mathrm{nat} \cdot \tau = \hbar. \tag{3.6}$$

The ground state is stable and hence $\tau \to 0$, which results in $\Gamma_\mathrm{nat} \to 0$. Therefore, the energy of the ground state is well-defined. The excited $\frac{3}{2}^-$-state has mean life-time of $\tau = 141$ ns corresponding to $\Gamma_\mathrm{nat} = 4.7$ neV. Hence, the energy is not well-defined, but Lorentz distributed [24]:

$$P(E)\mathrm{d}E = \frac{\Gamma}{2\pi} \frac{1}{[E - E_\mathrm{es}]^2 + \frac{\Gamma^2}{4}} \mathrm{d}E, \quad \text{with} \quad \int P(E)\mathrm{d}E = 1, \tag{3.7}$$

where E_es denotes the energy of the excited state.
The absorption of an emitted photon is possible, if there is a sufficient overlap of the transition lines, which is the case, if $2E_\mathrm{R} \leq \Gamma$. The separation of the two energy bands is $2E_\mathrm{R} \approx 3.9$ meV , which is $\approx 1.2 \cdot 10^6\ \Gamma_\mathrm{nat}$ [25]. As a consequence, resonance absorption is not possible in free nuclei (as well as in gases and liquids).
In the case of a solid state, the recoil energy can be partitioned into

$$E_\mathrm{R} = E_\mathrm{translation} + E_\mathrm{vibration}. \tag{3.8}$$

The translational part refers to the linear momentum, which is transferred to the whole lattice system due to the strong bonding of the nucleus in the lattice. This chemical bonds correspond to a binding energy of typically 10 eV and are much larger than the recoil energy [25]. Therefore, the nucleus can not recoil alone. Instead, the whole lattice has to recoil together. As the mass of the lattice system, M_lattice, is much larger then the mass of a free nucleus M, $E_\mathrm{translation} << \Gamma_\mathrm{nat}$. Thus, $E_\mathrm{translation}$ is negligible. The vibrational part describes the excitation of phonons. For resonance absorption, no phonon excitation should take place. The recoilless fraction f describes the probability of a zero-phonon process (the phonon system remains unchanged). Therefore, in a solid state, resonance emission and absorption of a photon can only take place, if $f > 0$.

3.3. Recoilless fraction

The Mössbauer effect is based on the probability of a recoil-free absorption of a photon. Therefore, it is necessary to know this probability, which is called recoilless fraction f. The simplest model system to describe the oscillation excitations of the nucleus is the

harmonic oscillator. Without any loss of generality, the harmonic oscillator is chosen to be one-dimensional. The corresponding Hamiltonian is

$$\mathcal{H} = \frac{\hat{p}^2}{2m} + \frac{1}{2}m\omega^2\hat{x}^2, \tag{3.9}$$

where $\hat{x}$ denotes the position operator and $\hat{p}$ the momentum operator. The Hamiltonian can be described in the second quantization formalism by introducing the annihilation operator $\hat{a}$ and the creation operator $\hat{a}^\dagger$:

$$\hat{a} = \sqrt{\frac{m\omega}{2\hbar}}\left\{\hat{x} + \frac{i}{m\omega}\hat{p}\right\} \qquad \text{and} \qquad \hat{a}^\dagger = \sqrt{\frac{m\omega}{2\hbar}}\left\{\hat{x} - \frac{i}{m\omega}\hat{p}\right\}. \tag{3.10}$$

Both operators are connected to $\hat{x}$ and $\hat{p}$ via

$$\hat{x} = \sqrt{\frac{\hbar}{2m\omega}}\left\{\hat{a}^\dagger + \hat{a}\right\} \qquad \text{and} \qquad \hat{p} = i\sqrt{\frac{\hbar m\omega}{2}}\left\{\hat{a}^\dagger - \hat{a}\right\}. \tag{3.11}$$

The harmonic oscillator Hamiltonian in second quantization is given by

$$\mathcal{H} = \hbar\omega\left\{\hat{a}^\dagger\hat{a} + \frac{1}{2}\right\}. \tag{3.12}$$

The particle number operator $\hat{n}$ is defined as

$$\hat{n} = \hat{a}^\dagger\hat{a} \tag{3.13}$$

and has the eigenstates (Fock states) $|n\rangle$, which are also eigenstates of the Hamiltonian:

$$\mathcal{H}|n\rangle = E_n|n\rangle, \qquad n \in \mathbb{N}. \tag{3.14}$$

An arbitrary excited state $|n\rangle$ can be created out of the ground state $|0\rangle$ by applying the creation operator n times:

$$|n\rangle = \frac{1}{\sqrt{n!}}\left[\hat{a}^\dagger\right]^n|0\rangle. \tag{3.15}$$

These states form a complete orthonormal set. A coherent (or Glauber) state $|\alpha\rangle$ can be constructed as a superposition of all Fock states $|n\rangle$ and is defined as [26]

$$|\alpha\rangle = e^{-\frac{1}{2}|\alpha|^2}\sum_n \frac{\alpha^n}{\sqrt{n!}}|n\rangle, \qquad \alpha \in \mathbb{C}, \tag{3.16}$$

and hence has an indefinite number of phonons. The coherent state is fully described by the complex number α and is the state, which shows the most resemblance with the classical harmonic oscillator states. For further information the interested reader is referred to the book "Coherent States in Quantum Physics" of Jean-Pierre Gazeau [27].

Recoilless fraction

A nucleus, which is in the ground state $|0\rangle$ with a momentum $\hbar k'$, absorbs a photon, which has a momentum $\hbar k$. The momentum of the nucleus after the absorption of the photon is $\hbar [k + k']$ due to momentum conservation. The ground state $|0\rangle$ is no eigenstate to the momentum operator $\hat{p}$ (or $\hat{k}$) and thus has to be expanded in an orthonormal basis set $|k'\rangle$:

$$|0\rangle = \sum_{k'} |k'\rangle \langle k'|0\rangle. \tag{3.17}$$

The final state $|F\rangle$ of the nucleus after the absorption of the photon is given by

$$|F\rangle = \sum_{k'} |k' + k\rangle \langle k'|0\rangle. \tag{3.18}$$

The corresponding displacement operator to $|k\rangle$ is $\mathrm{e}^{ik\hat{x}}$, which is proven in Appendix A. Applying the displacement operator on an arbitrary state $|k'\rangle$ gives

$$\mathrm{e}^{ik\hat{x}} |k'\rangle = |k' + k\rangle \tag{3.19}$$

and, therefore, the final state is given by

$$|F\rangle = \sum_{k'} |k' + k\rangle \langle k'|0\rangle = \mathrm{e}^{ik\hat{x}} |0\rangle , \tag{3.20}$$

which is no eigenstate of the Hamiltonian. Expanding $|F\rangle$ in the complete set of eigenstates $|n\rangle$ gives

$$|F\rangle = \sum_{n} |n\rangle \langle n|F\rangle = \sum_{n} |n\rangle \langle n| \mathrm{e}^{ik\hat{x}} |0\rangle. \tag{3.21}$$

The probability $P(|n\rangle)$, to find the nucleus in the state $|n\rangle$ after the absorption of a photon, is given by

$$P(|n\rangle) = \left| \langle n| \mathrm{e}^{ik\hat{x}} |0\rangle \right|^2 . \tag{3.22}$$

The recoilles fraction f of the Mössbauer effect is then the probability of the nucleus to remain in the ground state $|0\rangle$ after the absorption of the photon:

$$f = P(|0\rangle) = \left| \langle 0| \mathrm{e}^{ik\hat{x}} |0\rangle \right|^2 . \tag{3.23}$$

As mentioned earlier, $\mathrm{e}^{ik\hat{x}}$ is a displacement operator. In general, a unitary displacement operator $D(\alpha)$ is defined as

$$D(\alpha) = \mathrm{e}^{\alpha \hat{a}^\dagger - \alpha^* \hat{a}} \qquad \alpha \in \mathbb{C}. \tag{3.24}$$

Therefore, $\mathrm{e}^{ik\hat{x}}$ can be expressed in terms of $\hat{a}^\dagger$ and $\hat{a}$, using Eq. (3.11), by

$$ik\hat{x} = \alpha \hat{a}^\dagger - \alpha^* \hat{a}, \qquad \alpha = ik\sqrt{\frac{\hbar}{2M\omega}}, \tag{3.25}$$

where M denotes the mass of the nucleus. As $\mathrm{e}^{ik\hat{x}}$ is a displacement operator, the generated final state $|F\rangle$ is a coherent state:

$$\mathrm{e}^{ik\hat{x}}|0\rangle = \mathrm{e}^{\alpha\hat{a}^\dagger - \alpha^*\hat{a}}|0\rangle = |\alpha\rangle = \mathrm{e}^{-\frac{1}{2}|\alpha|^2}\sum_n \frac{\alpha^n}{\sqrt{n!}}|n\rangle. \tag{3.26}$$

Applying Eq. (3.26) to Eq. (3.23), the recoilless fraction f is given by

$$f = \left|\langle 0|\,\mathrm{e}^{-\frac{1}{2}|\alpha|^2}\sum_n \frac{\alpha^n}{\sqrt{n!}}|n\rangle\right|^2 \xrightarrow{\langle n_i|n_j\rangle = \delta_{ij}} f = \mathrm{e}^{-|\alpha|^2}. \tag{3.27}$$

α is determined in Eq. (3.25) and, therefore, f can be expressed by

$$f = \mathrm{e}^{-|\alpha|^2} = \exp\left(-\frac{\hbar k^2}{2M\omega}\right). \tag{3.28}$$

Using the property of the harmonic oscillator, that the average kinetic energy is one half of the total energy, and that the oscillator stays in the ground state $|n=0\rangle$ during the recoilless transition, the average squared displacement $\langle x^2\rangle$ can be determined by

$$\frac{1}{2}M\omega\langle x^2\rangle = \frac{1}{2}\left\{\frac{1}{2}\hbar\omega\right\} \rightarrow \langle x^2\rangle = \frac{\hbar}{2M\omega}, \tag{3.29}$$

which leads to the well-known expression for the recoilless fraction

$$f = \mathrm{e}^{-k^2\langle x^2\rangle}. \tag{3.30}$$

3.4. Temperature dependence of the recoilless fraction and second-order Doppler effect

The lifetime of the excited state is $\tau \approx 10^{-7}$ s, while the time of a lattice vibration is of the order of $t_{\mathrm{lattice}} \approx 10^{-13}$ s. Therefore, the average velocity $\langle v\rangle$ and the average displacement $\langle u\rangle$ of the oscillating nucleus is zero. However, $\langle u^2\rangle$ and $\langle v^2\rangle$ are non-zero and given by [25]

$$\langle u^2\rangle = \frac{\hbar}{2M}\int \mathrm{d}\omega\, \frac{1}{\omega}\coth\left(\frac{1}{2}\frac{\hbar\omega}{k_{\mathrm{B}}T}\right)g(\omega) \tag{3.31}$$

and

$$\langle v^2\rangle = \frac{3\hbar}{M}\int \mathrm{d}\omega\, \omega\coth\left(\frac{1}{2}\frac{\hbar\omega}{k_{\mathrm{B}}T}\right)g(\omega), \tag{3.32}$$

where M denotes the mass of the nucleus and $g(\omega)$ the phonon densitiy of states (DOS). To calculate $\langle u^2\rangle$ and $\langle v^2\rangle$, $g(\omega)$ has to be approximated. A useful model for the phonon

DOS is the Debye model, which leads to

$$\langle u^2 \rangle = \frac{3\hbar^2}{4Mk_B\theta_D} \left\{ 1 + 4 \left[\frac{T}{\theta_D} \right]^2 \int_0^{\theta_D/T} \frac{x}{e^x - 1} dx \right\} \tag{3.33}$$

$$\langle v^2 \rangle = \frac{9k_B\theta_D}{8M} \left\{ 1 + 8 \left[\frac{T}{\theta_D} \right]^4 \int_0^{\theta_D/T} \frac{x^3}{e^x - 1} dx \right\}. \tag{3.34}$$

Temperature dependence of the recoilless fraction

The temperature dependence of the recoilless fraction can be calculated by inserting Eq. (3.33) in Eq. (3.30), which leads to

$$f(T) = \exp\left(-\frac{3E_R}{2k_B\theta_D} \left\{ 1 + 4 \left[\frac{T}{\theta_D} \right]^2 \int_0^{\theta_D/T} \frac{x}{e^x - 1} dx \right\} \right), \tag{3.35}$$

where E_R denotes the recoil energy, k_B Boltzmann's constant, and θ_D the Debye temperature. However, $f(T)$ can be directly calculated by applying the coherent state formalism of the harmonic oscillator to excited states, as it was shown by Bateman *et al.*, resulting in Eq. (3.35) [28]. Eq. (3.35) shows, that the recoilless fraction increases with decreasing temperature, but is always $f < 1$, even in the theoretical case of zero temperature. This is illustrated in Fig. 3.1 for typical values of θ_D.
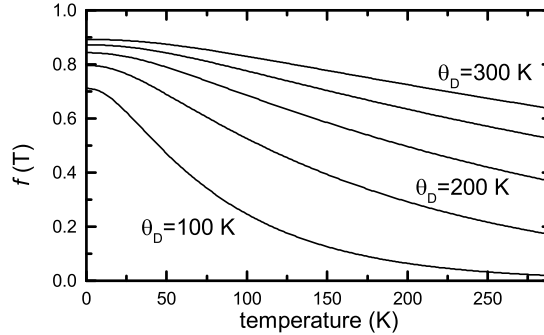
Figure 3.1.: Temperature dependence of the recoilless fraction $f(T)$ for Debye temperatures $\theta_D = 100\text{-}300$ K.

Second-order Doppler effect

The nucleus vibrates with a mean-squared velocity $\langle v^2 \rangle$, as described in Eq. (3.32), which leads to a modulation of the frequency of the emitted or absorbed photon. By applying Einstein's special theory of relativity, the frequency modulation in the laboratory reference frame is given by

$$\omega = \omega_0 \frac{\sqrt{1 - \frac{v^2}{c^2}}}{1 - \cos(\vartheta)\frac{v}{c}}, \tag{3.36}$$

where v denotes the velocity of the nucleus, c the speed of light and ϑ the angle between the photon direction and the velocity direction of the nucleus. Under the assumption of $v \ll$ c, Eq. (3.36) can be expanded as

$$\omega = \omega_0 \left\{ 1 + \frac{v}{\text{c}} \cos(\vartheta) - \frac{v^2}{2\text{c}^2} + \dots \right\}. \tag{3.37}$$

The term $\omega_0 \left\{ 1 + \frac{v}{\text{c}} \cos(\vartheta) \right\}$ describes the first-order Doppler effect, which is used to modulate the frequency of the photon in a Mössbauer spectroscopy experiment. The term $-\omega_0 \frac{v^2}{2\text{c}^2}$ describes the frequency modulation due to the time dilatation and is called second-order Doppler shift.
The average velocity $\langle v \rangle$ of the nucleus is zero, so the first-order Doppler effect vanishes. Consequently, Eq. (3.37) becomes

$$\langle \Delta\omega \rangle = \langle \omega - \omega_0 \rangle = -\omega_0 \frac{\langle v^2 \rangle}{2\text{c}^2} \qquad \text{or} \qquad \delta_\text{R} = \langle \Delta E \rangle = -E_0 \frac{\langle v^2 \rangle}{2\text{c}^2}. \tag{3.38}$$

The temperature dependence of the second-order Doppler shift $\delta_\text{R}(T)$ is determined by the temperature dependence of the mean-squared velocity $\langle v^2 \rangle$, which is described by Eq. (3.34), and leads to

$$\delta_\text{R}(T) = -\frac{9}{16} \frac{k_\text{B} E_\gamma}{M_\text{eff}\, \text{c}^2} \left\{ \theta_\text{D} + 8T \left[\frac{T}{\theta_\text{D}} \right]^3 \int_0^{\theta_\text{D}/T} \frac{x^3}{\text{e}^x - 1} \text{d}x \right\}$$

$$\hat{=} -\frac{9}{16} \frac{k_\text{B}}{M_\text{eff}\, \text{c}} \left\{ \theta_\text{D} + 8T \left[\frac{T}{\theta_\text{D}} \right]^3 \int_0^{\theta_\text{D}/T} \frac{x^3}{\text{e}^x - 1} \text{d}x \right\} \tag{3.39}$$

where the first equation computes the result in terms of energies and the second equation in terms of velocities. M_eff denotes the effective vibrating mass and E_γ the transition energy between the excited and ground state (for ^{57}Fe: 14.4 keV).

3.5. Mössbauer effect in a solid

As described on a classical level in Sec. 3.2, the energy transfer by the emission or absorption of a photon by a nucleus in a solid is negligible. A quantum mechanical derivation of this property is given in this chapter. Let the lth nucleus be displaced from its equilibrium position $\vec{r}_0$ by a distance $\vec{u}(l)$ due to the thermal motion of the nucleus, which leads to the position $\vec{r}_l = \vec{r}_0 + \vec{u}(l)$. The nucleus undergoes a transition from the initial state $|i\rangle$ to the final state $|f\rangle$ by the emission of a photon with the momentum $\hbar\vec{k}$. As the nucleus is bound in the lattice, the lattice may undergo a transition from the initial phonon state $|n_i\rangle$ to the final phonon state $|n_f\rangle$. The nuclear force, which causes the transition $|i\rangle \to |f\rangle$, is extremely short-ranged. The bonding forces in a lattice are weak, but long-ranged, compared to the nuclear force. Therefore, these two processes can be treated independently. As the nuclear transition is independent from the displacement of the nucleus, it will be neglected in the further treatment and focused on the phonon transition. Similar

3. Mössbauer spectroscopy

to Eq. (3.22), the probability of a phonon transition of the lattice after the emission of a photon by the nucleus is given by

$$p(n_f, n_i) = \left| \langle n_f | \mathrm{e}^{i\vec{k}\vec{r}_l} | n_i \rangle \right|^2, \qquad \text{with} \qquad \sum_f p(n_f, n_i) = 1. \qquad (3.40)$$

To calculate the transition energies, a sum rule is derived [29]. It is assumed for the further treatment, that the interactions between the atoms are independent from their velocities and depend on their positions only. Calculating the commutator of the lattice Hamiltonian with $\mathrm{e}^{i\vec{k}\vec{r}_l}$ gives

$$\left[\mathcal{H}, \mathrm{e}^{i\vec{k}\vec{r}_l} \right] = \left[\frac{\hat{p}}{2m}, \mathrm{e}^{i\vec{k}\vec{r}_l} \right] = \mathrm{e}^{\vec{k}\vec{r}_l} \left\{ \frac{\hbar^2 k^2}{2m} + \frac{\hbar\vec{k}}{m}\hat{\vec{p}} \right\}, \qquad (3.41)$$

as the kinetic energy operator is the only operator not commuting with $\mathrm{e}^{\vec{k}\vec{r}_l}$. m is the mass of the lth nucleus. The double commutator is then given by

$$\left[\left[\mathcal{H}, \mathrm{e}^{i\vec{k}\vec{r}_l} \right], \mathrm{e}^{-i\vec{k}\vec{r}_l} \right] = -\frac{\hbar^2 k^2}{m} = -2E_{\mathrm{R}}. \qquad (3.42)$$

Taking into account the properties of sum rules [30], Lipkin's sum rule is derived [25, 29]:

$$\sum_f [E_f - E_i] p(n_f, n_i) = E_{\mathrm{R}}, \qquad (3.43)$$

where E_f and E_i are the energies of the states n_f and n_i and E_{R} is the recoil energy of a free nucleus. Eq. (3.43) describes the average energy of all transitions between the phonon states n_f and n_i. There is a finite probability $p(n_{f=i}, n_i)$ for a transition, where no energy is transferred from the nucleus to the lattice, and therefore $E_f = E_i$. This probability is similar to the recoilless fraction f in Eq. (3.23). All other transitions cause a recoil. There is a finite probability of transitions with recoil, where the transferred energy is greater than the recoil energy E_{R}. Therefore, by allowing to excite higher frequency modes of the phonon spectra, the probability $p(n_{f=i}, n_i)$ of the zero-energy-transfer transition increases to maintain the average recoil energy E_R. To clarify this fact, an idealized example in the form of a two-level system is given. Let the phonon system be in the state $|n_0\rangle$ that can be excited in the state $|n_1\rangle$, where the corresponding energies are E_0 and E_1 with $E_1 - E_0 > E_R$. Applying this to Eq. (3.43) gives

$$\begin{aligned} E_R &= \sum_f [E_f - E_i] p(n_f, n_i) = \sum_{f=0}^{1} [E_f - E_0] p(n_f, n_0) \\ &= [E_0 - E_0] p(n_0, n_0) + [E_1 - E_0] p(n_1, n_0) \\ &= [E_1 - E_0] p(n_1, n_0) \end{aligned} \qquad (3.44)$$

and, therefore, the probability to excite the phonon to the state $|n_1\rangle$ is given by

$$p(n_1, n_0) = \frac{E_R}{E_1 - E_0} < 1, \qquad E_1 \ - \ E_0 \ > \ E_R \ . \tag{3.45}$$

Using $\sum_f p(n_f, n_i) \ = \ 1$, the probability of a transition with zero energy transfer ($|n_0\rangle \rightarrow |n_0\rangle$) is given by

$$p(n_0, n_0) = 1 - \frac{E_R}{E_1 - E_0}. \tag{3.46}$$

By increasing the energy of the excited phonon mode E_1, the probability $p(n_0, n_0)$ increases, which leads to an increased Mössbauer effect.

In the Debye approximation, $p(n_i, n_i)$ is given by [29]

$$p(n_i, n_i) = \exp\left(-\frac{3}{2}\frac{\hbar^2 k^2}{2m k_B \theta_D}\right), \tag{3.47}$$

where m is the mass of the nucleus emitting or absorbing the photon, $\hbar k$ the momentum of the photon, k_B Boltzmann's constant and θ_D the Debye temperature.

3.6. Hyperfine interaction

The nucleus interacts with its electromagnetic environment. The corresponding Hamilton operator is given by

$$\begin{aligned}
\mathcal{H}_{hf} &= \mathcal{H}_{el} + \mathcal{H}_Z \\
&= \int \rho(\vec{r})\Phi(\vec{r}) \ \mathrm{d}^3 r - \vec{\mu}\vec{B},
\end{aligned} \tag{3.48}$$

where the former term describes the energy of the nuclear charge distribution in the electric potential of its surrounding. The latter term describes the interaction of the nuclear magnetic moment with a magnetic field.

3.6.1. Electric interaction

To calculate $\mathcal{H}_{el}$, it is useful to perform a Taylor expansion of the electric potential around $\vec{r} = 0$ resulting in

$$\Phi(\vec{r}) = \Phi(\vec{r}') \ |_{\vec{r}'=0} +\vec{r}\left[\vec{\nabla}'\Phi(\vec{r}')\right]_{\vec{r}'=0} + \frac{1}{2}\left\{\vec{r}\vec{\nabla}'\left[\vec{r}\vec{\nabla}'\Phi(\vec{r}')\right]_{\vec{r}'=0}\right\} + \dots \ . \tag{3.49}$$

3. Mössbauer spectroscopy

Therefore, $\mathcal{H}_{el}$ can be written as

$$\mathcal{H}_{el} = \int \rho(\vec{r}) \left\{ \Phi(\vec{r}') \mid_{\vec{r}'=0} + \vec{r} \left[\vec{\nabla}' \Phi(\vec{r}') \right]_{\vec{r}'=0} + \frac{1}{2} \left\{ \vec{r}\vec{\nabla}' \left[\vec{r}\vec{\nabla}' \Phi(\vec{r}') \right]_{\vec{r}'=0} \right\} \right\} \mathrm{d}^3 r \qquad (3.50)$$

$$= \underbrace{\int \rho(\vec{r}) \Phi(0) \mathrm{d}^3 r}_{=E_0 = Ze\Phi(0)} + \underbrace{\int \rho(\vec{r}) \vec{r} \left[\vec{\nabla}' \Phi(\vec{r}') \right]_{\vec{r}'=0} \mathrm{d}^3 r}_{=E_1} + \underbrace{\int \rho(\vec{r}) \frac{1}{2} \left\{ \vec{r}\vec{\nabla}' \left[\vec{r}\vec{\nabla}' \Phi(\vec{r}') \right]_{\vec{r}'=0} \right\} \mathrm{d}^3 r}_{=E_2}$$

by neglecting terms of the order of $\mathcal{O}(\vec{\nabla}^3)$ and higher.

E_0 is the Coulomb energy of a point charge and hence constant. It contributes to the potential energy of the lattice, but can be neglected for the further treatment of the hyperfine interactions.

E_1 describes the dipole interaction of the electric dipole moment of the nuclear charge distribution with an electric field $\vec{E} = -\vec{\nabla}\Phi$. The nuclear states have a defined parity, i.e. $|\psi(\vec{r})|^2 = |\psi(-\vec{r})|^2$. Therefore, the static electric dipole moment of the nucleus has to be zero and E_1 vanishes.

E_2 is the so-called quadrupole term. By adding a nutritious zero, E_2 can be written as

$$E_2 = \frac{1}{6} \sum_{i,j} \left\{ \Phi_{ij} \int \mathrm{d}^3 r \, \rho(\vec{r}) \left[3r_i r_j - \delta_{ij} \vec{r}^2 \right] + \delta_{ij} \Phi_{ij} \int \mathrm{d}^3 r \, r^2 \rho(\vec{r}) \right\}, \qquad (3.51)$$

with

$$\Phi_{ij} = \left(\frac{\partial^2 \Phi}{\partial r_i \, \partial r_j} \right)_0. \qquad (3.52)$$

This expression can be simplified in the principal axis system of the electric potential:

$$E_2 = \frac{1}{6} \int \mathrm{d}^3 r \, \rho(\vec{r}) r^2 \sum_i^3 \Phi_{ii} + \frac{1}{6} \sum_i^3 \Phi_{ii} \int \mathrm{d}^3 r \, \rho(\vec{r}) \left[3r_i^2 - r^2 \right]. \qquad (3.53)$$

The z-axis is chosen in a way, that Φ_{zz} has the highest absolute value of the components of Φ_{ii}. With

$$\int \mathrm{d}^3 r \, \rho(\vec{r}) r^2 = Ze \left\langle r^2 \right\rangle \qquad (3.54)$$

and

$$\sum_i^3 \Phi_{ii} = \Delta\Phi(0) = -\frac{\rho(0)}{\varepsilon_0} \qquad (3.55)$$

as well as the definition of the nuclear quadrupole moment

$$eQ_{ii} = \int \mathrm{d}^3 r \, \rho(\vec{r}) \left[3r_i^2 - r^2 \right], \qquad (3.56)$$

Eq. (3.53) can be written as

$$E_2 = \underbrace{-\frac{Ze}{6\varepsilon_0}\rho(0)\langle r^2\rangle}_{=\text{ monopole shift}} + \underbrace{\frac{e}{6}\sum_i^3 V_{ii}Q_{ii}}_{=\text{ quadrupole interaction}} \quad . \tag{3.57}$$

Center shift

The monopole shift is composed of two effects. One has nuclear origin and depends on the average squared radius $\langle r^2\rangle$. In the case of ^{57}Fe, the excited spin $\frac{3}{2}^-$ state has a smaller $\langle r^2\rangle$ value than the spin $\frac{1}{2}^-$ ground state [24]. This effect depends only on the main quantum number. Therefore, it is independent of the other interactions and results in a constant shift of the spectra. The second effect is based on the finite probability density of the s-electrons at the nucleus. The center shift δ is defined as the difference of the monopole shift of source (S) and absorber (A) and can be calculated using

$$\delta = \frac{Ze^2c}{6\varepsilon_0\hbar\omega_0}\left\{|\psi_A(0)|^2 - |\psi_S(0)|^2\right\}\underbrace{\left[\langle r_{\text{es}}^2\rangle - \langle r_{\text{gs}}^2\rangle\right]}_{<0}, \tag{3.58}$$

with the electronic charge density at the nucleus $-e|\psi(0)|^2$, the average squared radius $\langle r^2\rangle$ and the unperturbed transition energy $\hbar\omega_0$ between excited (es) and ground state (gs). Therefore, the center shift depends on the used radioactive source. In this thesis, δ is given against α-Fe.

The temperature dependence of the center shift is the sum of the temperature-independent chemical shift δ_{C} and a temperature-dependent contribution $\delta_{\text{R}}(T)$ (in Debye-approximation) due to the second-order Doppler shift (see section 3.4 for more details)

$$\delta(T) = \delta_{\text{C}} + \delta_{\text{R}}(T), \tag{3.59}$$

$$\delta_{\text{R}}(T) = -\frac{9}{16}\frac{k_{\text{B}}}{M_{\text{eff}}\,c}\left\{\theta_{\text{D}} + 8T\left[\frac{T}{\theta_{\text{D}}}\right]^3\int_0^{\theta_{\text{D}}/T}\frac{x^3}{e^x-1}dx\right\} \tag{3.60}$$

where M_{eff} denotes the effective mass of the ^{57}Fe atom, c the speed of light, k_{B} Boltzmann's constant, and θ_{D} the Debye-temperature [24].

Quadrupole interaction

The quadrupole interaction describes the interaction of the nuclear quadrupole moment eQ_{ii} with an electric field gradient $V_{ii} = \Phi_{ii} - \frac{1}{3}\Delta\Phi$. As V_{ii} is traceless, two parameter are sufficient to describe the system: V_{zz}, which is chosen to be

$$V_{zz} \geq V_{yy} \geq V_{xx}, \tag{3.61}$$

and the asmmetry parameter η, which is defined as

$$\eta = \frac{V_{xx} - V_{yy}}{V_{zz}}. \tag{3.62}$$

The classical expression in Eq. (3.57) can be transformed, using the Wigner-Eckhart-theorem, into the form

$$\mathcal{H}_{\mathrm{el}} = \frac{eQ_{zz}V_{zz}}{4I\left[2I - 1\right]} \left\{ 3\hat{I}_z^2 - \hat{I}^2 + \frac{\eta}{2} \left[\hat{I}_+^2 + \hat{I}_-^2 \right] \right\}, \tag{3.63}$$

with nuclear spin operator $\hat{I}$ and the displacement operators $\hat{I}_+$ and $\hat{I}_-$.

3.6.2. Magnetic hyperfine interaction

The interaction of a magnetic field $\vec{B}$ with a magnetic moment $\vec{\mu}$ can be described by the Zeeman-Hamilton operator

$$\mathcal{H}_\mathrm{Z} = -\vec{\mu}\vec{B} = -\gamma\vec{I}\vec{B}, \tag{3.64}$$

where $\gamma = g\frac{\mu_\mathrm{N}}{\hbar}$ denotes the gyromagnetic ratio with μ_N being the nuclear magneton and g the Landé factor. By choosing, without any loss of generality, $\vec{B} = B_z\vec{e}_z$, the eigenvalues of the Hamilton operator $\mathcal{H}_Z$ can be obtained by computing the expectation value

$$\begin{aligned} \langle\mathcal{H}_\mathrm{Z}\rangle &= E_\mathrm{Z} \\ &= \langle I, m| - \mu_z B_z |I, m\rangle \\ &= -\gamma B_z \hbar m, \end{aligned} \tag{3.65}$$

where m is the magnetic quantum number. Therefore, the magnetic field breaks the degeneracy in m and leads to $[2I+1]$ substates.

The magnetic moment of the excited state is μ_es = -0.153(4) μ_N and of the ground state μ_gs = +0.0903(7) μ_N [31]. Therefore, as both magnetic moments are not equal, eight transitions between the excited and ground state are possible. Taking into account the dipole selection rules ($\Delta m = \pm 1, 0$), only six transitions are allowed.

The magnetic field at the nucleus is given by

$$\vec{B} = \vec{B}_\mathrm{loc} + \vec{B}_\mathrm{el}, \tag{3.66}$$

where $\vec{B}_\mathrm{loc}$ denotes the so-called "local field" due to an applied external field. This contribution is neglected in the further treatment of the magnetic field, as no external fields were applied in this work. The second term describes the electronic contribution and is given by [24]

$$\vec{B}_\mathrm{el} = -g_\mathrm{el}\mu_0\mu_\mathrm{B} \sum_i \left\{ \frac{1}{4\pi}\frac{\vec{l}_i}{r_i^3} + \frac{1}{4\pi}\left[\frac{\vec{s}_i}{r_i^3} - \frac{3\vec{r}_i[\vec{s}_i\vec{r}_i]}{r_i^5}\right] + \frac{2}{3}\delta(\vec{r}_i)\vec{s}_i) \right\}, \tag{3.67}$$

where μ_B denotes the Bohr magneton, g_el the electronic Landé factor, $\vec{l}_i$ the angular momentum, and $\vec{s}_i$ the spin of the ith electron at a position vector $\vec{r}_i$. The first term describes the so-called orbital field due to the orbital momentum of unpaired electrons. The second term describes the dipole-dipole interaction of the magnetic moment of the nucleus with the total spin magnetic moment of the valence electrons. The third term is the Fermi contact term and describes the finite spin density of the s-electrons at the nucleus.

Combined electric and magnetic hyperfine interaction

The Hamiltonian for the combined electric and magnetic interaction is given by [24]

$$
\mathcal{H}_{\mathrm{hf}} = \frac{eQ_{zz}V_{zz}}{4I\left[2I-1\right]}\left\{3\hat{I}_z^2 - \hat{I}^2 + \frac{\eta}{2}\left[\hat{I}_+^2 + \hat{I}_-^2\right]\right\}
$$
$$
- g\frac{\mu_{\mathrm{N}}}{\hbar}B\left\{\frac{\hat{I}_+\mathrm{e}^{-i\Phi} + \hat{I}_-\mathrm{e}^{+i\Phi}}{2}\sin(\theta) + \hat{I}_z\cos(\theta)\right\}, \tag{3.68}
$$

using Eq. (3.63) and Eq. (3.64). Φ denotes the polar angle and θ the azimuth angle between the principal axis of the EFG and the magnetic hyperfine field. Calculating the transition matrix elements is more difficult, compared to the bare electric or magnetic interaction, due to the non-diagonal structure of the Hamiltonian. The corresponding eigenstates of $\mathcal{H}_{\mathrm{hf}}$ are mixed states of the bare m substates and can be calculated by diagonalizing $\mathcal{H}_{\mathrm{hf}}$. This calculations were performed by using the MöSSFIT-software [32]. The hyperfine interactions are summarized in Fig. 3.2.
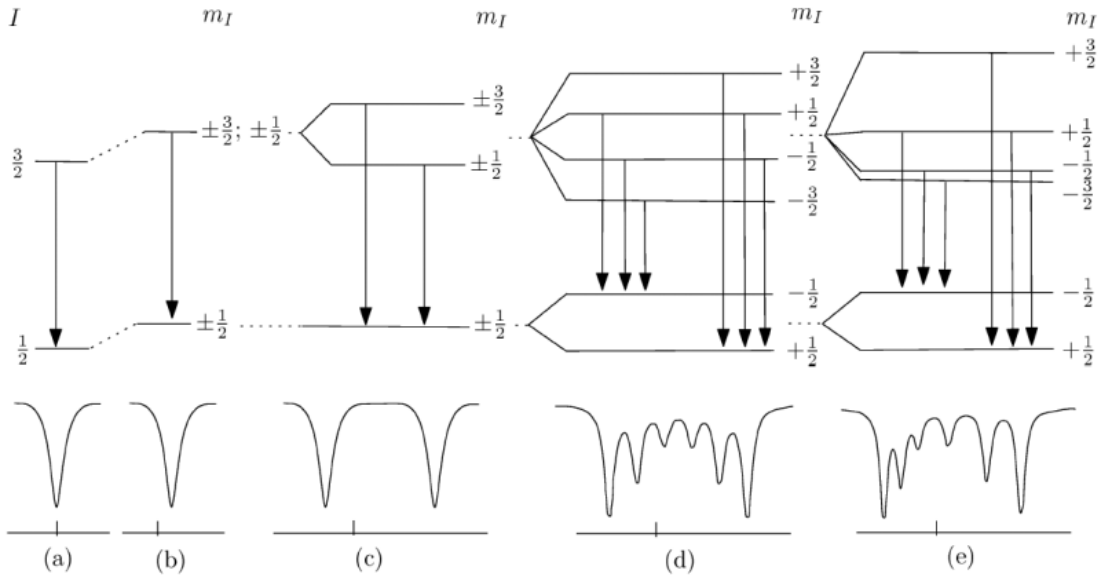
Figure 3.2.: Influence of the hyperfine interactions on the energy levels of the excited spin 3/2 state and the spin 1/2 ground state (top row) and the corresponding Mössbauer spectra (lower row). I denotes the nuclear spin and m_I the magnetic quantum number. (a) Bare transition without any hyperfine interaction. (b) Change of the energy levels of both states due to the isomer shift. (c) Splitting of the excited state in two degenerated sub states due to the interaction of the nuclear spin with an electric field gradient. (d) The interaction of the nuclear spin with a magnetic field breaks the degeneracy in m and leads to $[2I+1]$ sub states. Due to the dipole selection rules, only six transitions are allowed. (e) Combined magnetic and electric hyperfine interaction.

3.7. Experimental set up and measurement principle

The used experimental setup in transmission geometry is shown in Fig. 3.3. For Möss-bauer spectroscopy in scattering geometry or conversion electron spectroscopy as well as additional informations about the transmission geometry, the interested reader is referred to the books "*Nukleare Festkörperphysik: kernphysikalische Messmethoden und ihre An-wendungen*" by G. Schatz and A. Weidinger or "*Grundlagen und Anwendungen der Möss-bauerspektroskopie*" by D. Barb.

In transmission geometry, the transmission signal of the emitted γ quanta is recorded. The energy of the γ quanta can be changed via the Doppler effect by moving the radioactive source. Therefore, the recorded spectra is the transmission of the γ quanta through the sample as a function of the velocity, which is equal to an energy. If the energy of the emitted γ quant is equal to the energy difference between an excited and ground state of the ^{57}Fe in the sample, the γ quant can be absorbed, which corresponds to a minima in the transmission spectrum. Typical Mössbauer spectra are shown in Fig. 3.2.
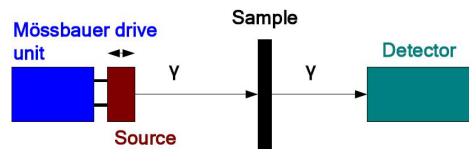
Figure 3.3.: Schematic of the experimental setup in transmission geometry.

3. Mössbauer spectroscopy

4. Iron-based superconductors

Iron-based superconductors such as Th_7Fe_3, U_6Fe, and $Lu_2Fe_3Si_5$ with superconducting transition temperatures of T_c = 1.8 K, 3.9 K, and 6.1 K, respectively, are known for over 50 years [33–35]. However, beginning with the discovery of superconductivity in $LaO_{1-x}F_xFeAs$ with a superconducting transition temperature of T_c = 26 K in 2008 [5] the expression iron-based superconductors refers mainly to this class of high-temperature superconductors, namely the iron pnictides respectively iron chalcogenides.

The phase diagram of $LaO_{1-x}F_xFeAs$ is shown in Fig. 4.1. The parent compound
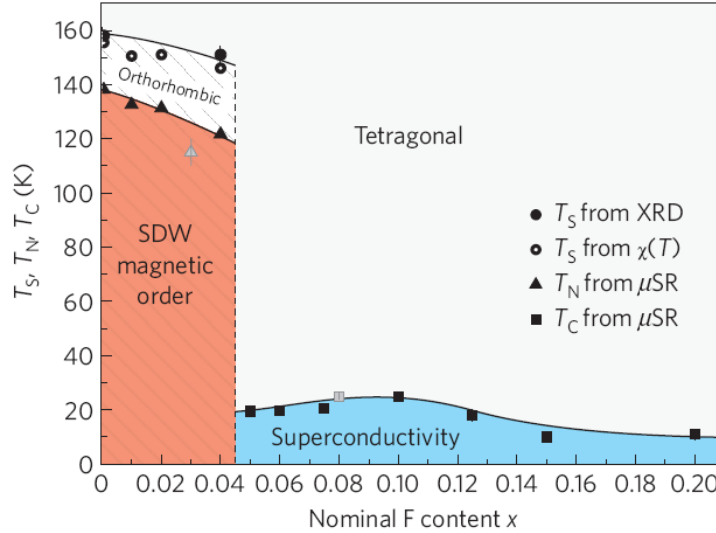
Figure 4.1.: Phase diagram of $LaO_{1-x}F_xFeAs$. The spin density wave (SDW) magnetic order as well as the tetragonal-to-orthorhombic phase transition is suppressed as a function of F doping and superconductivity emerges. Taken from Ref. [36].

LaOFeAs shows a tetragonal-to-orthorhombic phase transition at T_S = 156 K and a subsequent long-range antiferromagnetic spin density wave (SDW) order below T_N = 138 K [36, 37]. This is one of the most important differences between the iron pnictides and the long-known Fe-based superconductors such as U_6Fe, where the iron is non-magnetic. The magnetic order as well as the structural phase transition in $LaO_{1-x}F_xFeAs$ are suppressed as a function of the F doping [36]. Superconductivity emerges close to or after the suppression of the magnetic order. This suggests a competition of the superconducting and magnetically ordered ground states. Measurements of the phonon density of states using inelastic neutron scattering methods as well as linear-response calculations showed, that a phonon mediation of the superconductivity can be ruled out [38, 39]. This indicates an un-

conventional pairing mechanism, e.g. via magnetic fluctuations due to the close proximity of superconductivity and magnetism [40].

LaO$_{1-x}$F$_x$FeAs represents one example of several structural modifications of the iron pnictides and chalcogenides. The first commonality among this Fe-based compounds is the iron-pnictogen (FePn) respectively iron-chalcogen (FeChn) layer, which is shown for different families in Fig. 4.2. In the "1111" family, the FePn layer is separated by rare-earth-
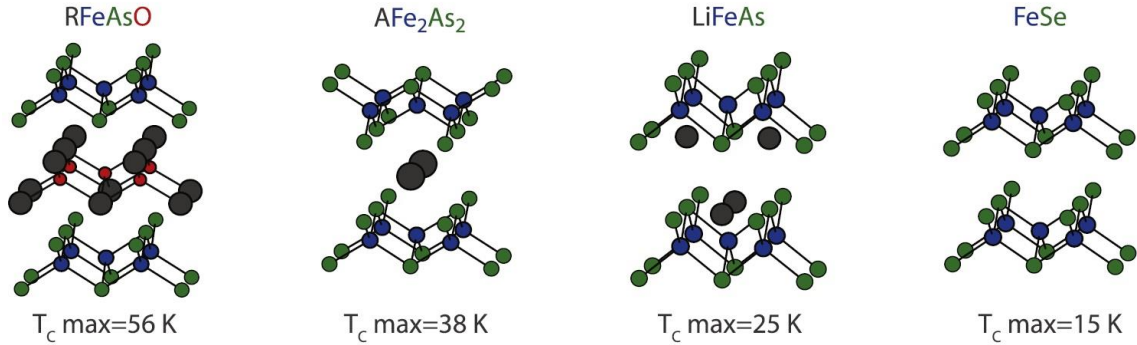
Figure 4.2.: Crystal structure of iron-based superconductors. From left to right the different "families" including the highest superconducting transition temperature T_c: 1111, 122, 111 and 11. Taken from Ref. [41].

oxygen layers. In the "122" family, alternating FePn layers are separated by alkaline-earth metal layers. In the "111" family, the alkaline metal is located in the FePn plane. In the "11" family, no separation of the FeChn layers is present.

In this work, I studied Ca$_{1-x}$Na$_x$Fe$_2$As$_2$ and Fe$_{1+y}$Te. For this reason, I will give a short overview about the 122 and 11 family. A more detailed description of the properties of Ca$_{1-x}$Na$_x$Fe$_2$As$_2$ and Fe$_{1+y}$Te is given in the corresponding chapters (Sec. 5 and 6). For information about the 1111 and 111 iron pnictides as well as additional informations about the 122 iron pnictides and 11 iron chalcogenids, the interested reader is referred to the reviews of Lumsden and Christianson [41], Johnston [42], Johrendt [43], Hirschfeld *et al.* [44], and Stewart [45].

The so-called "122" compounds are one class of the recently discovered iron-based superconductors. In 1980, Pfister and Nargosen reported the successful growth of single crystals of ternary transition-metal arsenides [48]. They prepared the ternary arsenides AET_2As$_2$ (AE = Ca, Sr, Ba, and T = Cr, Fe, Co, Ni, Cu). These compounds form in the tetragonal ThCr$_2$Si$_2$ structure with the space group $I4/mmm$. They consist of edge-sharing TAs$_4$ tetrahedra forming a TAs plane, which is separated by AE atoms.

The superconducting Fe-based 122 compounds can be summarized by the chemical formula $AE_{1-x}A_x$(Fe$_{1-y}T_y$As$_{1-z}$P$_z$)$_2$ with the alkaline-earth metals AE (= Ca, Sr, Ba), the alkaline metals A (= Na, K, Rb, Cs), and the transition metals T (= Co, Ni, Rh, Ru, Mn). The undoped AEFe$_2$As$_2$ compounds show antiferromagnetic (π, 0) spin density wave order with T_N = 140 K (Ba [49]), 205 K (Sr [50]), and 170 K (Ca [49, 51]). The magnetic phase transition is accompanied by a tetragonal-to-orthorhombic phase transition. The orthorhombic phase has the space group $Fmmm$ and is characterized by the structural order parameter $\delta = (a\text{-}b)/(a+b)$, which is the orthorhombic splitting of the crystallographic
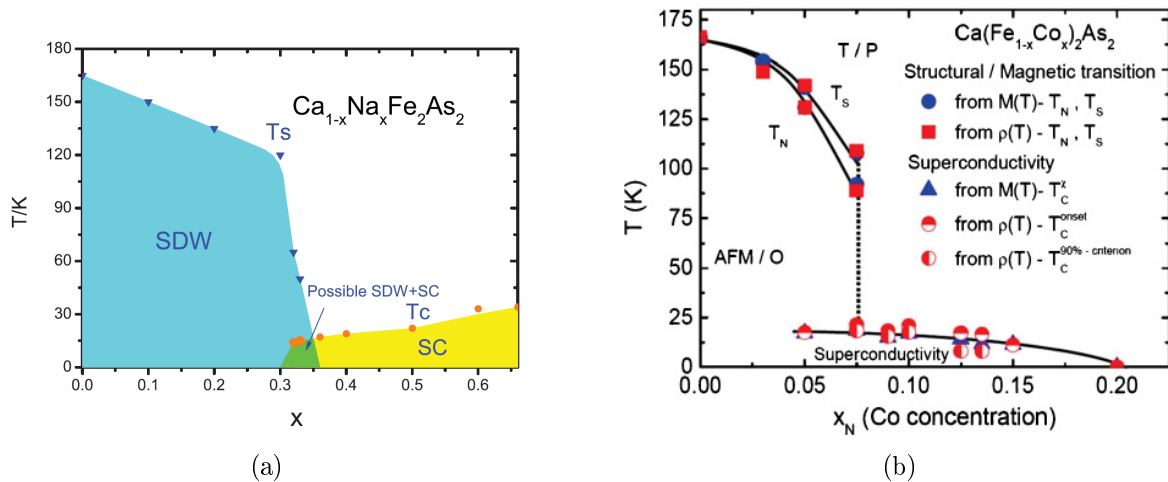
Figure 4.3.: (a) Phase diagram of $Ca_{1-x}Na_xFe_2As_2$, taken from Ref. [46]. Please note, that the shown Na-substitution levels are of nominal character (except for $x = 0.66$). (b) Phase diagram of $Ca(Fe_{1-x}Co_xAs)_2$, taken from Ref. [47].

a- and b-axis. The magnetic and structural phase transition are first-order indicating a strong magneto-structural coupling [50, 52, 53].

The fully substituted AFe$_2$As$_2$ compounds, i.e., hole-doped by one electron per formula unit, are superconductors with $T_c = 3.8$ K (K [54]), 2.6 K (Cs [54]), and 2.6 K (Rb [55]) and remain in the tetragonal structure down to lowest temperatures. The substitution of an alkaline-earth metal by an alkaline metal results in a suppression of the magnetic and structural order parameter as well as the magnetic and structural transition temperatures and superconductivity emerges. This is shown for the case of $Ca_{1-x}Na_xFe_2As_2$ in Fig. 4.3(a). Similar to the $AE{\rightarrow}A$ substitution, the Fe$\rightarrow T$ substitution results in a suppression of the magnetic and structural order parameter as well as the magnetic and structural transition temperatures and superconductivity emerges. This is shown for $Ca(Fe_{1-x}Co_x)_2As_2$ in Fig. 4.3(b). In both cases, a substitution level regime is found, where magnetic order and superconductivity coexist. However, there is a difference between the Fe and the AE substitution. The suppression of the magnetic order is much stronger for substitution in the FeAs plane than for substitution of the interlayer AE atoms.

The iron chalcogenides, known as "11"-compounds, are by structural means the simplest compounds of the iron-based superconductors as the FeChn layers are not separated by alkaline (earth) metals or rare-earth-oxide layers such as in the 111, 122, or 1111 compounds. The basic elemental formula of this class can be written as $Fe_{1+y}Te_{1-x}Se_x$ and the corresponding phase diagram is shown in Fig. 4.4. α-FeSe is a stoichiometric superconductor with $T_c = 8$ K [57]. Sales et $al.$ found traces of superconductivity with $T_c \sim 14$ K in a wide substitution range of $x \in (0;1]$ [58]. However, only stoichiometries near $x \sim 0.5$ and for small y values show bulk superconductivity [58]. For higher excess-iron values y, superconductivity is completely suppressed [56]. The other end of the phase diagram, $Fe_{1+y}Te$, is known since 1974 [59]. The magnetic order in $Fe_{1+y}Te$ is different than the observed magnetic structures in the 122 and 1111 compounds resulting in an exceptional position of $Fe_{1+y}Te$ in the class of the iron-based superconductors, as it shows $(\pi/2, \pi/2)$
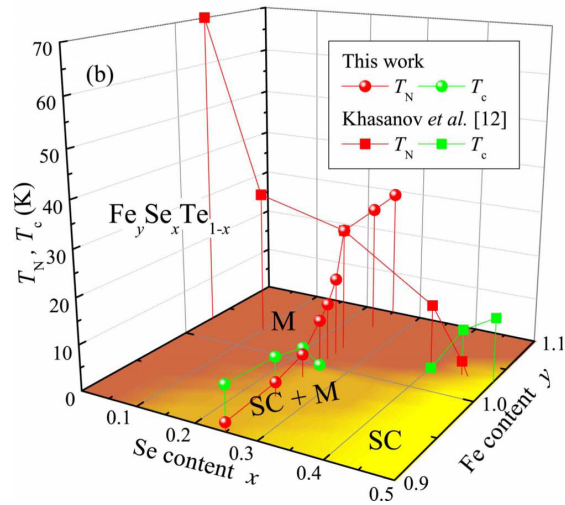
Figure 4.4.: Phase diagram of $Fe_{1+y}Te_{1-x}Se_x$. Taken from Ref. [56]

SDW order [60].
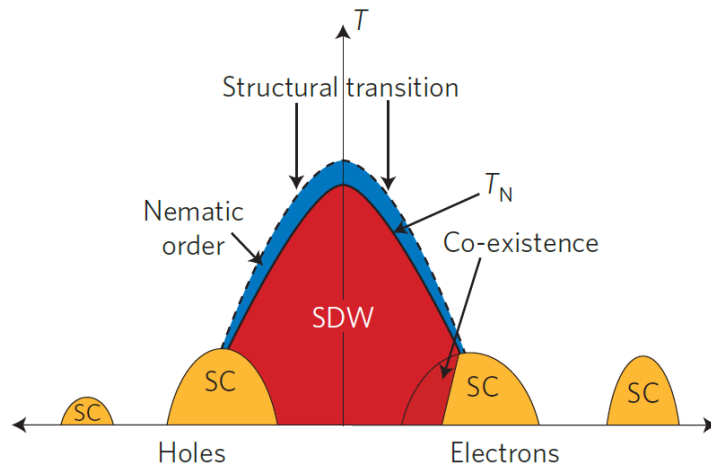
Figure 4.5.: Generic phase diagram of the iron pnictides. Taken from Ref. [61].

A generic phase diagram for the iron pnictides is shown in Fig. 4.5 [61]. Starting from an antiferromagnetically ordered parent compound, such as LaOFeAs or $BaFe_2As_2$, the magnetic order is suppressed and superconductivity emerges by hole or electron doping. However, also isovalent doping such as Fe→Ru or As→P substitution, as well as application of hydrostatic pressure can cause the suppression of magnetic order and appearance of superconductivity. Remarkably, a region in the phase diagram appears, where both magnetic order and superconductivity are present. One possibility is, that both phases are separated as it is the case in $LaO_{1-x}F_xFeAs$ or $Ba_{1-x}K_xFe_2As_2$ [62]. A second possibility is a coexistence on a nanoscopic scale as in $SmO_{1-x}F_xFeAs$ with superconducting domains with a size of the superconducting coherence length [63, 64]. A third possibility is a homogeneous superconducting state coexisting with a homogeneous magnetic order as it was

found in $Ba_{1-x}Na_xFe_2As_2$ [65]. This implies, that the same electrons at the Fermi surface are both superconducting and magnetically ordered. Local probes such as muon spin relaxation or Mössbauer spectroscopy are necessary to decide, which type of coexistence is present.

4.1. From SDW to SC

For a deeper understanding of the superconductivity in the iron-based superconductors it is crucial to understand the development of the superconducting state out of the spin density wave state of the parent compounds $AEFe_2As_2$. The subsequent description of this development can easily applied to the other families of the iron-based superconductors.

The 122 parent compounds $CaFe_2As_2$, $SrFe_2As_2$, and $BaFe_2As_2$ reveal electrical resistivity values of 0.1-1 mΩcm indicating semi-metallic behaviour [49, 66, 67]. For comparison, metals exhibit electrical resistivities of $1 - 10$ μΩcm, which are 2-3 orders of magnitude smaller. These 122 compounds are multi-band materials with five Fe $3d$ bands crossing the Fermi energy [43, 44]. In the non-magnetic state, two or more hole bands near (0,0) and two electron pockets near (0,π) and (π,0) cross the Fermi level in the unfolded Brillouin zone. Therefore, two electron and at least two hole Fermi surfaces (FS) are present. A schematic FS is shown in Fig. 4.6. These multiple FSs with a high density of states (DOS) at the FS, $N(E_F)$, and enable various possibilities of electronic ordering, such as SDW, charge-density wave (CDW), or superconductivity [68–70].
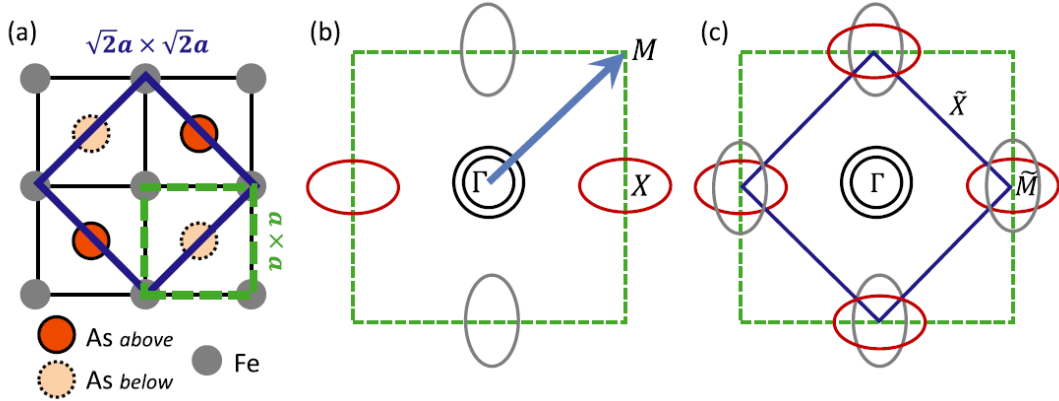
Figure 4.6.: (a) Schematic FeAs lattice showing the 1-Fe unit cell (green $a \times a$) and the 2-Fe unit cell (blue $\sqrt{2}a \times a\sqrt{2}$). (b) Fermi surface topology in the unfolded BZ (1-Fe unit cell) with an antiferromagnetic ordering vector $\vec{Q}_{AFM} = (\pi, 0) = \Gamma \rightarrow X$. The blue arrow denotes the folding vector (π, π). (c) Fermi surface topology in the folded BZ (2-Fe unit cell) with an antiferromagnetic ordering vector $\vec{Q}_{AFM} = (\pi, \pi) = \Gamma \rightarrow \tilde{M}$. Picture taken from Ref. [44].

$CaFe_2As_2$, $SrFe_2As_2$, and $BaFe_2As_2$ show magnetic order below with the respective transition temperatures T_N = 170 K [49, 51], 205 K [50], and 140 K [49]. The iron

magnetic moments show commensurate antiferromagnetic order along the orthorhombic *a*- and *c*-axis and ferromagnetic order along the orthorhombic *b*-axis. This is the so-called "stripe order" due to the ferromagnetic stripes along the crystallographic *b*-axis. This corresponds to a commensurate magnetic ordering vector $\vec{Q}_{\text{AFM}} = (\frac{1}{2}, \frac{1}{2}, 1)_{\text{T}} = (1,0,1)_{\text{O}}$ in reciprocal lattice units, where the subscripts denotes the tetragonal (T) and orthorhombic (O) unit cell. As the magnetic unit cell is the same as the orthorhombic unit cell, it is useful to use the orthorhombic description of $\vec{Q}_{\text{AFM}}$. Due to the semi-metallic behaviour, a spin density wave description of the magnetic order is commonly used.

SDW order requires the presence of FS nesting. In the case of perfect FS nesting, which is the case, if the FSs are cylinders of equal radii in a compensated metal, the SDW state fully gaps the FS. As a consequence, a formation of another state (e.g. SC or CDW) is not possible. However, angle-resolved photoemission spectroscopy (ARPES) experiments reveal a non-perfect FS nesting in the 122 parent compounds [71–73]. The electron pockets show an elliptic and the hole pockets a circular cross section [71–74]. Despite the different shapes of the pockets, there radii are of similar values in the undoped compounds [75]. If one shifts the hole pockets by $(\pi,0)$, a sufficient overlap of the electron and hole pockets is found and it is appropriate to speak of quasi-nesting. By entering the SDW state below T_{N}, a reconstruction of the FS occurs as well as an opening of an electronic excitation gap at parts of the FS [76]. At the parts of the FS without a SDW gap, another state such as SC or CDW may develop. Furthermore, the form of the hole pockets around the Γ point changes from cylindrical and quasi two-dimensional above T_{N} to a three-dimensional ellipsoid below T_{N}, while the electron pockets around X show a two-dimensional "propeller"-like structure [73]. This reconstruction was observed in ARPES experiments by Kondo *et al.* [76]. They observed long parallel segments of the FS along k_z indicating intensive nesting in the magnetically ordered state.

Upon doping, the FSs may change. It was shown, that the hole pocket expands and the electron pocket shrinks upon hole doping [21, 77, 78]. The size of the hole-pockets at Γ increases due to the increased amount of holes per Fe, while the propeller blades of the electron pockets are reduced. This evolution reduces the quasi-nesting of the FSs and consequently weakens the SDW state.

It was shown by Fernandes *et al.* [79], Vorontsov *et al.* [69], and Schmiedt *et al.* [80], that a SDW can coexist with superconductivity. The simplest model to describe the electronic structure considers one electron and one hole band [69]. In this case, the double degeneracy of the electronic states at the center and corners of the BZ is neglected. However, the double degeneracy does not seems to be essential for neither the superconductivity nor magnetism [81–92]. The result of their calculations is, that a commensurate SDW can coexist with a superconducting $s^{\pm}$ state in a certain parameter range, if the electron pocket has a finite ellipticity and a difference in the chemical potentials of the electron and hole pockets is present. If only one condition is fulfilled, both states are separated by a first-order transition. An incommensurate SDW may coexist with a superconducting $s^{\pm}$ state, if the electron pocket has a finite ellipticity. A difference in the chemical potentials of the electron and hole pockets is not mandatory. For the superconducting s^{++} state, the situation is completely different, as no coexistence phase for SDW and SC is found [69, 79]. Even in the presence of a FS in the SDW state, s^{++} SC does not emerge.

In summary, there is an effective "attraction" between the SDW and the superconducting $s^{\pm}$ state resulting in a coexistence region for certain parameters, while an effective "repulsion" is present for s^{++} SC resulting in no coexistence.

4. Iron-based superconductors

5. Mössbauer and muon spin relaxation spectroscopy of $Ca_{1-x}Na_xFe_2As_2$

5.1. The system $Ca_{1-x}Na_xFe_2As_2$

For a deeper understanding of the magnetic properties of $Ca_{1-x}Na_xFe_2As_2$ observed by Mössbauer spectroscopy and μSR, it is useful to discuss thermodynamic and structural properties of the compounds.

Calcium has an electron configuration of $[Ar]4s^2$ and Sodium of $[Ne]3s^1$. Therefore, the substitution of Calcium by Sodium introduces holes in the system. The ionic radius of Na^+ (1.18 Å) is larger compared to Ca^{2+} (1.12 Å) [93]. At room temperature, $Ca_{1-x}Na_xFe_2As_2$ forms in the tetragonal $ThCr_2Si_2$ structure with space group $I4/mmm$, which is shown in Fig. 5.1(a). Ca and Fe occupy the 2a and 4d crystallographic sites, which have fixed positions (0|0|0) and (0|0.5|0.25), respectively. As occupies the 4e crystallographic site, which has a variable position (0|0|z). Within the Na-substitution level range $x \in [0.00;0.67]$, z varies between 0.3658 and 0.3645 [46]. The a- and c-axis parameter as a function of x are shown in Fig. 5.1(b) [46].

The increase of the c-axis parameter with increased Na-substitution level x is a direct consequence of the larger ionic radius of Na^+ than Ca^{2+}. The shrinked a-axis parameter with increased x is attributed to the hole-doping character of the substitution [95]. The anion height above the Fe layer increases from 1.357 Å to 1.401 Å for $x = 0.00$ and 0.66, respectively, due to the larger radius of Na than Ca [46]. Additionally, the Fe-As intralayer distance remains nearly constant upon Na-substitution with $d_{Fe-As} = 2.374(3)$ Å [46]. The Fe-Fe intralayer distance slightly decreases from $d_{Fe-Fe} = 2.751$ Å to 2.716 Å for $x = 0$ and 0.66, respecitvely [46]. In summary, the Fe-As tetrahedron is slightly compressed upon Na substitution compared to $CaFe_2As_2$, while the c-axis parameter is enhanced due to the larger radius of the substituent.

$CaFe_2As_2$ shows a tetragonal-to-orthorhombic transition at 170-173 K [51, 96]. In the orthorhombic $Fmmm$ phase, Ca and Fe occupy the 2a and 8f sites, which have the positions (0|0|0) and (0.25|0.25|0.25), respectively. As occupies the 8i site, which has the position (0,0,z). However, the anion height z seems to be independent of the structure and is of equal value for the tetragonal and orthorhombic phase [46, 51]. The orthorhombic unit cell is rotated by 45° with respect to the tetragonal basal plane axes. The orthorhombic phase is characterized by the structural order parameter $\delta_s = (a-b)/(a+b)$, which is the orthorhombic splitting of the crystallographic a- and b-axis. For $CaFe_2As_2$, $\delta_s(10 \text{ K}) = 0.005(1)$ is obtained [96], which is similar to $SrFe_2As_2$ and $BaFe_2As_2$, where

<div style="text-align:center">(a)   (b)</div>
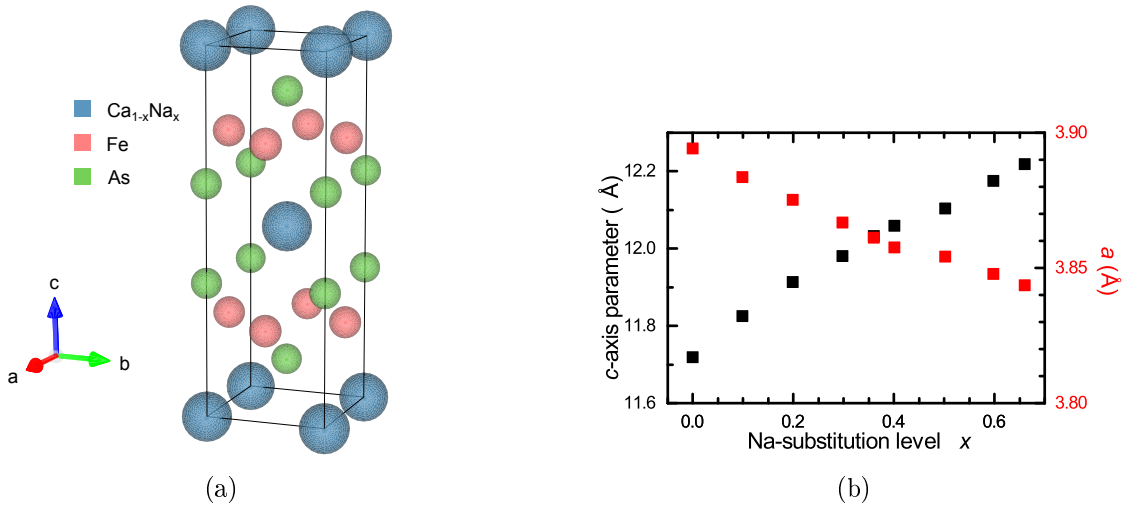
Figure 5.1.: (a) Crystal structure of $Ca_{1-x}Na_xFe_2As_2$ in the tetragonal phase. Picture is created using [94]. (b) Lattice parameters as a function of the Na-substitution level x in the tetragonal phase. With increased x, c increases while a shrinks. The c/a ratio increases as a function of x and the volume V increases with increasing x. Data taken from Ref. [46].

$\delta_s(20 \text{ K}) = 0.005$ [97] and 0.004 [49] are observed, respectively. However, investigations of the crystallographic structure at low temperatures and therefore in the magnetically ordered state as well as in the superconducting state for finite x are still lacking. Taking into account the Na-substitution level dependence of δ_s for $Sr_{1-x}Na_xFe_2As_2$ [98] and $Ba_{1-x}Na_xFe_2As_2$ [99], where a suppression of the structural order parameter as well as reduction of the structural phase transition temperature is observed, it is self-evident to assume a similar behaviour in $Ca_{1-x}Na_xFe_2As_2$. Therefore, the crystallographic structure in $Ca_{1-x}Na_xFe_2As_2$ with a finite x in the magnetically ordered phase is assumed to be orthorhombic *Fmmm* with a reduction of δ_s as a function of x.

5.2. Experimental details

Platelet single crystals of $Ca_{1-x}Na_xFe_2As_2$ were investigated using ^{57}Fe-Mössbauer and muon spin relaxation (μSR) spectroscopy. Samples with $x = 0.00$, 0.35, 0.50, and 0.67 were grown by Luminita Harnagea using the self-flux technique as described in Ref. [47, 100] and characterized using energy-dispersive x-ray spectroscopy (EDX), x-ray diffraction (XRD), susceptibility, magnetization, and specific-heat measurements. The stoichiometry of the examined samples are $x = 0.00$, 0.35, 0.50, and 0.67 as determined by EDX. Characterization of the magnetic properties were performed using SQUID magnetometry.

The μSR experiments were performed at the πM3 beamline of the Swiss Muon Source at the Paul Scherrer Institut, Villigen, Switzerland, using the GPS and DOLLY spectrometer. The muon spin relaxation was measured in temperatures ranging from 1.6 up to 300 K in zero (ZF) and transverse (TF) magnetic fields up to 120 mT. The initial muon

spin polarization was rotated by $\approx$ -45° with respect to the z-direction determined by TF-μSR. I measured the x = 0.35 and 0.50 samples, Hemke Maeter measured the sample with x = 0.67 and Hubertus Luetkens measured the sample with x = 0.00. The μSR data was analysed using the MUSRFIT software [101].

I performed the Mössbauer spectroscopy (MBS) experiments together with Til Goltz and Sirko Kamusella at the Institut für Festkörperphysik, TU Dresden, in transmission geometry in a temperature range between 4.2 and 300 K using a CryoVac Konti IT cryostat. As a γ-source, ^{57}Co in Rhodium matrix was used. For the MBS experiments, the single crystals were cleaved to ensure sufficient transmission of the γ-beam. This was necessary, as the γ-radiation was nearly 100 % absorbed in the case of uncleaved crystals due to its large thicknesses. The data were analysed using the MOESSFIT software [32].

In μSR and MBS experiments, the single crystals were aligned with the crystallographic c-axis along the γ-/muon-beam direction.

5.3. Magnetic-susceptibility measurements
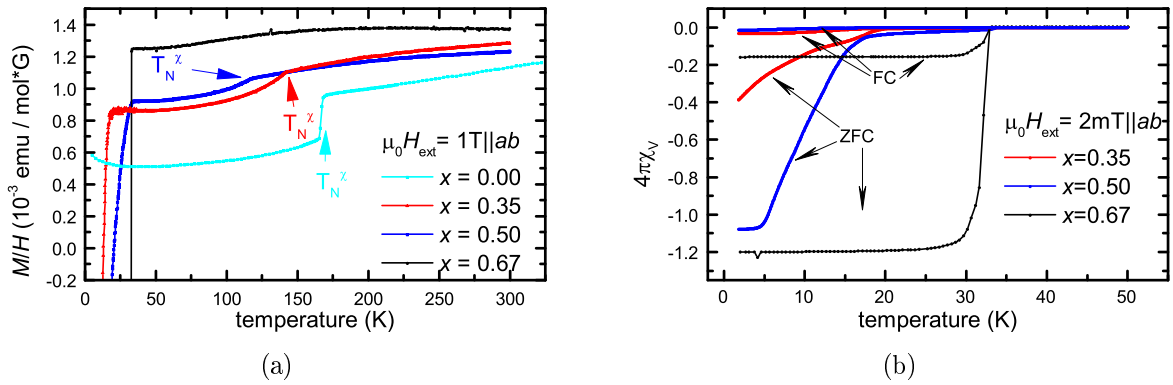
Figure 5.2.: Temperature dependence of the magnetic susceptibility of $Ca_{1-x}Na_xFe_2As_2$ (with x = 0.00, 0.35, 0.50, and 0.67). The measurements were performed at applied fields of (a) 1 T and (b) 2 mT parallel to the ab-plane. T_N^χ = 167 K, 143 K, and 119 K for x = 0.00, 0.35, and 0.50, respectively, are the magnetic transition temperatures determined by the magnetic susceptibility measurements. Zero (ZFC) and field-cooled (FC) measurements show superconductivity in parts of the sample (x = 0.35, T_c = 17 K) and bulk superconductivity (x = 0.50 and 0.67 with T_c = 17 K and 34 K, respectively).

Magnetic-susceptibility measurements in an applied field of 1 T parallel to the ab-plane are shown in Fig. 5.2(a). For x = 0.00, 0.35, and 0.50, a nearly linear decrease of the magnetic susceptibility is observed in the paramagnetic region, which is found also for many other iron-based supercondcutors [102–104]. The kinks at 167 K (x = 0.00), 143 K (x = 0.35), and 119 K (x = 0.50) indicate the magnetic transition temperature T_N^χ. For x = 0.67, a nearly linear decrease of the magnetic susceptibility is also observed above the superconducting transition temperature T_c = 34 K. The slope of the decrease changes at $\approx$ 150 K. This change may be attributed to the onset of antiferromagnetic fluctuations.

Magnetic-susceptibility measurements in an applied field of 2 mT parallel to the *ab*-plane are shown in Fig. 5.2(b). For $x = 0.35$, below 17 K a broad superconducting transition occurs. As the diamagnetic shielding is not fully developed, only parts of the sample show superconductivity. For $x = 0.50$, a two-step superconducting transition occurs. Below 34 K, a slightly negative magnetic susceptibility is measured, which indicates a superconducting phase in a small volume of the sample. Below 17 K, a broad second transition occurs, where bulk superconductivity is formed resulting in the full superconducting response. For the further treatment of the $x = 0.50$ sample, 17 K will be considered as the superconducting transition temperature. This two-step behaviour as well as the broad transition indicates an inhomogeneous sample. The sample with $x = 0.67$ shows bulk superconductivity below 34 K. The sharp transition indicates a homogeneous sample.

5.4. Results and discussion

5.4.1. Magnetic order in $Ca_{1-x}Na_xFe_2As_2$

ZF-μSR spectra for $x = 0.00$, 0.35, and 0.50 are shown in Fig. 5.3 for both detector pairs 3,4 and 2,1. To analyse the ZF time spectra, the function

$$
\begin{aligned}
P(t) = &V_{\mathrm{mag}} \sum_{i=1}^{2} p_i \left\{ a_{1,i} \cos(2\pi f_{\mu,i} t + \phi) \mathrm{e}^{-\lambda_{\mathrm{T},i} t} + a_{2,i} \mathrm{e}^{-\lambda_{\mathrm{L},i} t} \right\} \\
&+ [1 - V_{\mathrm{mag}}] G_{\mathrm{GKT}}(t, \sigma_{\mathrm{nm}})
\end{aligned}
\tag{5.1}
$$

with two magnetically inequivalent muon stopping sites was used. V_{mag} denotes the magnetic volume fraction (MVF), λ_{T} the transverse and λ_{L} the longitudinal relaxation rate, f_μ the muon spin precession frequency, and $G_{\mathrm{GKT}}(t, \sigma_{\mathrm{nm}})$ the static Gauss-Kubo-Toyabe function.

In the paramagnetic temperature regime, a weak Gauss-Kubo-Toyabe damping of $P(t)$ is observed caused by the dipole-dipole interaction of the muon spin with randomly oriented dense nuclear magnetic moments in absence of ordered electronic moments for all investigated stoichiometries. The obtained relaxation rates are $\sigma_{\mathrm{nm}} = 0.067$ MHz, 0.052 MHz, and 0.074 MHz for $x = 0.00$, 0.35, and 0.50, respectively. TF-μSR experiments were performed by applying a magnetic field of 5 mT perpendicular to the initial muon spin polarization to study the temperature dependence of the magnetic volume fraction. To describe the magnetic phase transition, two temperatures are defined. $T_{\mathrm{N}}^{\mathrm{onset}}$ is defined as the highest temperature with a finite V_{mag}. $T_{\mathrm{N}}^{100\%}$ is defined as as the highest temperature with $V_{\mathrm{mag}} = 100\ \% \mathrel{\hat=} 1$. The resulting temperature dependence of the magnetic volume fraction is shown in Fig. 5.4.

$T_{\mathrm{N}}^{\mathrm{onset}}$, $T_{\mathrm{N}}^{100\%}$, and $\Delta T = T_{\mathrm{N}}^{\mathrm{onset}}$ - $T_{\mathrm{N}}^{100\%}$, which are obtained by analysing the temperature dependence of the magnetic volume fraction, are summarized in Tab. 5.1.

A reduction of the magnetic transition temperatures with increased Na-substitution level is observed. Additionally, $\Delta T = T_{\mathrm{N}}^{\mathrm{onset}}$ - $T_{\mathrm{N}}^{100\%}$ increases with increased Na-substitution level, which is caused by the higher degree of disorder in the Na-substituted systems compared to $CaFe_2As_2$ in combination with an increased gradient of the $T_{\mathrm{N}}(x)$ curve
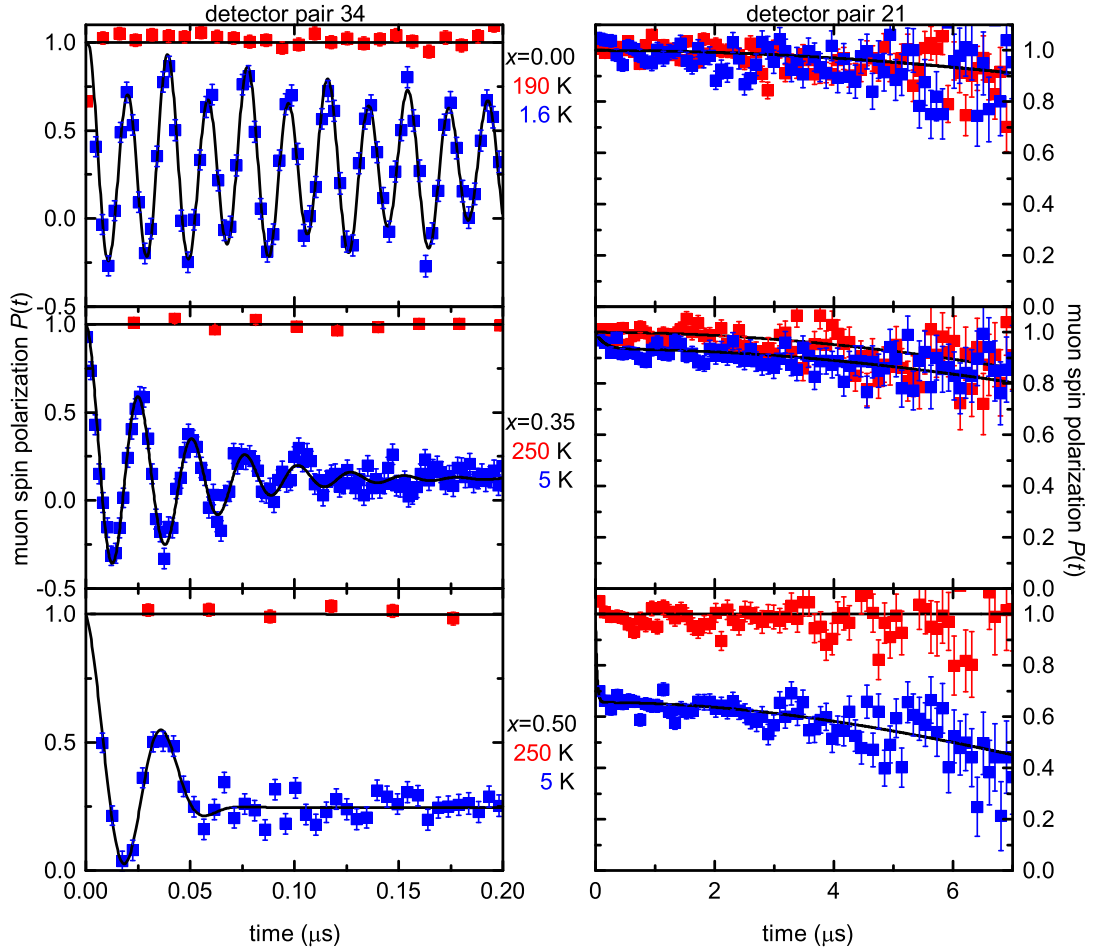
Figure 5.3.: Time evolution of the muon spin polarization for representative temperatures in the paramagnetic and magnetically ordered temperature regime for $x = 0.00$ (upper row), 0.35 (middle row), and 0.50 (lower row). The measurements were performed using detector pair 3,4 (left column) and 2,1 (right column). See Sec. 2.5 for more details of the experimental setup. Lines are best fits to Eq. (2.37). Please note the different time scales.
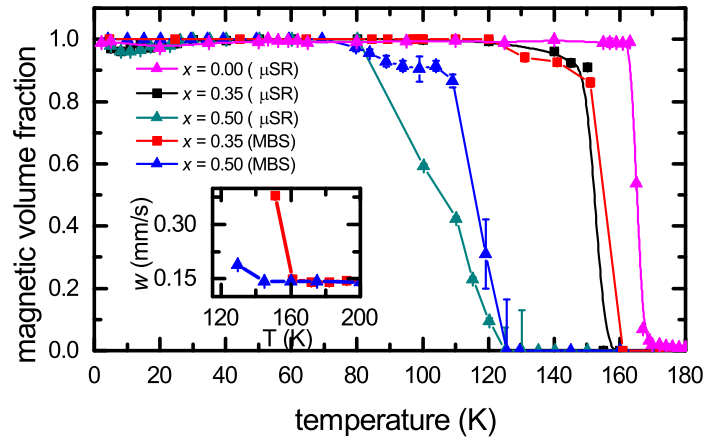
Figure 5.4.: Temperature and Na-substitution level dependence of the magnetic volume fraction for $x = 0.00$, 0.35, and 0.50. A reduction of the onset of the magnetic ordering temperature as well as a broadening of the phase transition is observed with increased Na-substitution level. The onset of the magnetic order is determined by i) the appearance of a well-defined muon spin precession in the μSR experiments and ii) an abrupt increase of the paramagnetic linewidth w, which is shown in the inset, in the Mössbauer spectroscopy.

with increasing x.

In the magnetically ordered temperature regime, the detector pairs 3,4 and 2,1 study different muon spin components. Analysing detector pair 3,4 studies the muon spin component perpendicular to the crystallographic c-axis. In the magnetically ordered state, two magnetically inequivalent muon (A, B) sites are obtained. This is consistent with calculations by Yuri Pashkevich [105], who found two magnetically inequivalent muon stopping sites. The calculations were performed at $SrFe_2As_2$ in the *Fmmm* structure using a modified Thomas-Fermi approach, which results in the muon stopping sites $(0.00|0.00|0.20)$ and $(0.19|0.19|0.40)$, where the former is the main muon site A. The two muon sites show a temperature and Na-substitution level independent occupation ratio of P_A:P_B= 80:20 as it is found in $BaFe_2As_2$ [106]. In $SrFe_2As_2$, an occupation ration of P_A:P_B= 70:30 is observed [50]. This indicates, that the muon stopping sites in $SrFe_2As_2$ may be slightly different from those in $BaFe_2As_2$ and $CaFe_2As_2$. However, it is self-evident due to the same structure to assume, that the muon stopping sites in $CaFe_2As_2$ and $BaFe_2As_2$ are not completely different from those in $SrFe_2As_2$ and only small corrections to the two calculated positions occur. For $x = 0.00$, the signal fraction corresponding to muons stopping at site A show a well-defined sinusoidal oscillation below 167 K. This indicates static long-range commensurate magnetic order. The signal fraction corresponding to muons stopping at site B show an exponential relaxation below 167 K and a well-defined sinusoidal oscillation below 60 K. This indicates a broad field distribution at temperatures between 60 K and 167 K at the muon stopping site B suppressing a coherent oscillation of the muon spins, which is contrary to the observations in $BaFe_2As_2$, where two well-defined sinusoidal oscillation frequencies are obtained at all temperatures below T_N [106]. Below 60 K, the

x	$T_{\mathrm{N}}^{100\%}$	$T_{\mathrm{N}}^{\mathrm{onset}}$	$\Delta T = T_{\mathrm{N}}^{\mathrm{onset}}$ - $T_{\mathrm{N}}^{100\%}$
0.00	163(2) K	167(2) K	4(4) K
0.35	140(3) K	161(2) K	21(5) K
0.50	80(3) K	125(3) K	45(6) K

Table 5.1.: Summary of the magnetic transition temperatures obtained by Mössbauer (MBS), TF- and ZF-muon spin relaxation experiments, of the investigated $\mathrm{Ca_{1-x}Na_xFe_2As_2}$ compounds with $x = 0.00$, 0.35, and 0.50. $T_{\mathrm{N}}^{\mathrm{onset}}$ denotes the temperature, where magnetic order starts to develop and a finite magnetic volume fraction is observed. $T_{\mathrm{N}}^{100\%}$ denotes the temperature, where a magnetic volume fraction of 100 % is observed. The obtained magnetic transition temperatures by both techniques for $x = 0.35$ and 0.50 are equal within error bars.

two precession frequencies have a temperature independent ratio of $f_A/f_B = 1.9$. The temperature dependence of f_A is shown in Fig. 5.5(a) with $f_A(T{\rightarrow}0) = 52.0$ MHz.

(a)   (b)
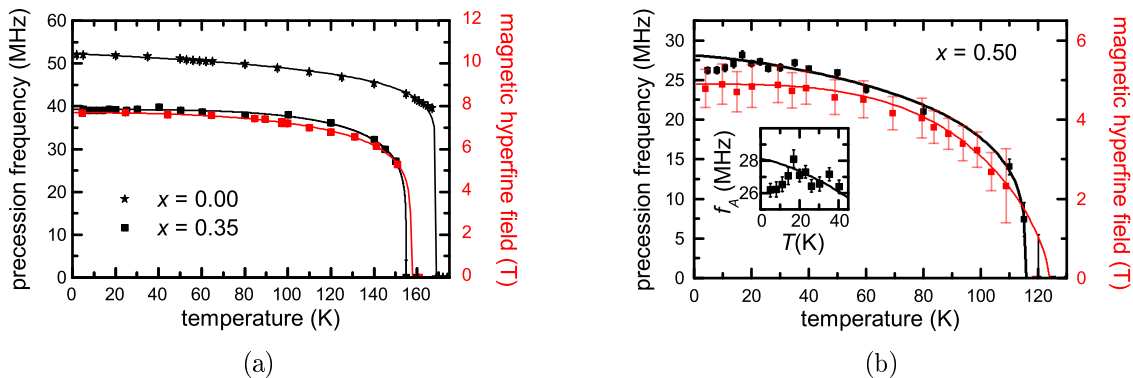
Figure 5.5.: Temperature dependence of the magnetic order parameter for (a) $x = 0.00$ and 0.35 and (b) $x = 0.50$ including best order parameter fits according to Eq. (5.2). For reasons of clarity, only frequency f_A, which corresponds to the 80 % occupation probability, is shown. The Mössbauer hyperfine field in 5.5(b) is the average value of the Gaussian-distributed hyperfine field with one standard deviation as error bar. The inset in 5.5(b) shows the low-temperature regime, where superconductivity occurs below $T_c = 17$ K.

For $x = 0.35$ and 0.50, two well-defined sinusoidal precession frequencies with temperature-independent ratios of $f_A/f_B \approx 4$ and 8, respectively, are observed below $T_{\mathrm{N}}^{\mathrm{onset}}$. The temperature dependencies of the corresponding f_A are shown in Figs. 5.5(a) and 5.5(b). A reduction of the muon spin precession frequency and, therefore, of the magnetic order parameter with increased Na-substitution level is observed. Additionally, the damping of the muon spin oscillation increases with increased Na-substitution level, which can be seen in the ZF time spectra in Fig. 5.3. This indicates a broader field distribution at the muon site, which is consistent with a higher degree of disorder due to the Na substitution. The magnetic-susceptibility measurements, which were introduced in Sec. 5.3,

prove a superconducting phase in parts of the sample volume ($x = 0.35$) or in the whole sample volume ($x = 0.50$). To study the interaction of the magnetic and superconducting order parameter, f_A is analysed using a temperature-dependent phenomenological order parameter (M) fit of the form [107]

$$M(T) = M(T = 0) \cdot \left[1 - \left(\frac{T}{T_N} \right)^\alpha \right]^\beta \qquad (5.2)$$

above and below the superconducting transition temperature $T_c = 17$ K for $x = 0.35$ and 0.50. For $x = 0.35$, a fit to Eq.(5.2) above T_c for $f_A(T)$ represents the data in the whole temperature range with $f_A(T{\to}0) = 39.3$ MHz. Therefore, no interaction between the magnetic and superconducting order parameter is detectable.

For $x = 0.50$, the muon spin precession frequency is reduced by approximately 7 % below 17 K with $f_A(T{\to}T_c) = 27.5$ MHz. As both order parameters compete for the same electrons at the Fermi surface, this reduction of the magnetic order parameter proves the microscopic coexistence of magnetic order and superconductivity. Both order parameters are weakly coupled compared to $Ba_{1-x}Na_xFe_2As_2$, where a reduction of the muon spin precession frequency and, therefore, of the magnetic order parameter of ≈ 65 % is observed [65]. A theoretical study of the order parameter interaction is presented in Sec. 5.4.2.

Analysing detector pair 2,1 studies the muon spin component parallel to the crystallographic c-axis. Down to lowest temperatures, most parts of the signal shows a Gauss-Kubo-Toyabe depolarization. Only a small fraction of muons experiencing a fast exponential damping corresponding to a loss in the asymmetry respectively a fast depolarization. This fast depolarization increases with increased Na-substitution level, which can be seen in the ZF time spectra in Fig. 5.3. For $x = 0.00$, no difference in the ZF time spectra and, therefore, no loss in the asymmetry is observed. In contrast, for $x = 0.35$ and 0.50 a fast depolarization of 5 % and 35 % of the signal is observed, respectively. Taking into account the well-defined muon spin precession seen in detector pair 3,4 and the mainly Gauss-Kubo-Toyabe depolarization in detector pair 2,1, one can conclude, that the magnetic field at the muon site points essentially in the direction of the crystallographic c-axis with an increased magnetic field component in the ab-plane as a function of the Na-substitution level. This is consistent with Fe moments located in the ab-plane and a tilting out of the ab-plane as a function of the Na-substitution level. Additionally, no change in the time spectra for $x = 0.50$ below 50 K is observed, and, hence, a spin reorientation below the superconducting transition temperature can be ruled out as a possible origin of the 7 % reduction of the muon spin precession frequency below T_c.

The Na-substitution dependence of the muon spin precession-frequency ratio. f_A/f_B changes from 1.9 to 4 and 8 for $x = 0.00$, 0.35, and 0.50, respectively. This change is more drastic compared to other 122 compounds. In the following, first the undoped 122 compounds are discussed and afterwards the effect of Na and K doping. The ionic radii and electronic configuration of the alkaline (earth) metals used in 122 compounds are shown in Fig. 5.6. The c-axis parameter increases nearly linear as a function of the ionic radius.

Ca is the smallest and Cs the largest ion [93]. As a consequence, the crystallographic c-axis is shortest for $CaFe_2As_2$ [46] and longest for $CsFe_2As_2$ [54]. However, only $CaFe_2As_2$, $SrFe_2As_2$, and $BaFe_2As_2$ show magnetic order, while $NaFe_2As_2$, KFe_2As_2, $RbFe_2As_2$, and
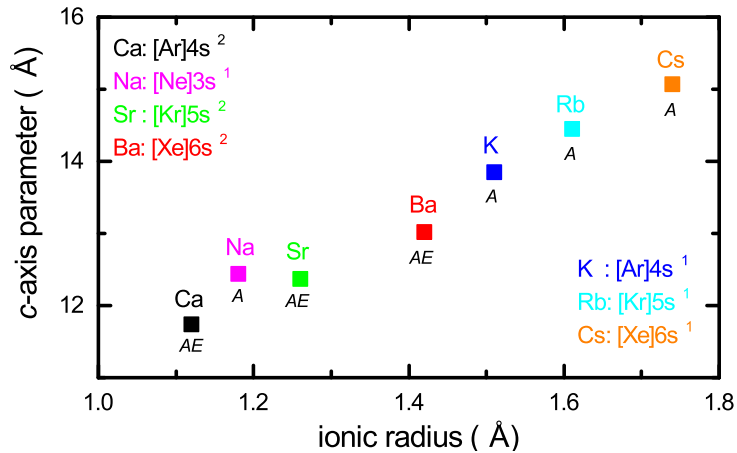
Figure 5.6.: *c*-axis parameter of various $A\mathrm{Fe_2As_2}$ and $AE\mathrm{Fe_2As_2}$ compounds (A = Na, K, Rb, Cs, AE = Ca, Sr, Ba) as a function of the ionic radii of the alkaline (earth) metals. A nearly linear increase of c as a function of the ionic radius is observed. Please note, that $\mathrm{NaFe_2As_2}$ is only metastable [108]. Additionally, the electronic configuration of the alkaline (earth) metal is shown. The ionic radii are taken from Ref. [93]. The *c*-axis parameter of the $A\mathrm{Fe_2As_2}$ and $AE\mathrm{Fe_2As_2}$ compounds are taken from: Ca [51], Na [108], Sr [54, 109], Ba [110], K [54, 110], Rb [55], Cs [54].

$\mathrm{CsFe_2As_2}$ are superconducting. Therefore, only $\mathrm{CaFe_2As_2}$, $\mathrm{SrFe_2As_2}$, and $\mathrm{BaFe_2As_2}$ are discussed further.

In Fig. 5.7(a), f_A and f_A/f_B are shown as a function of the *c*-axis parameter, which is proportional to the ionic radii. The muon spin precession frequency f_A (f_B) is highest for $\mathrm{CaFe_2As_2}$ with 52 MHz (27.4 MHz) and decreases to 44 MHz (12.9 MHz) and 29 MHz (7.1 MHz) for $\mathrm{SrFe_2As_2}$ [50] and $\mathrm{BaFe_2As_2}$ [111], respectively. f_A/f_B is lowest for $\mathrm{CaFe_2As_2}$ with 1.9 and increases to 3.4 for $\mathrm{SrFe_2As_2}$ [50] and 4.1 for $\mathrm{BaFe_2As_2}$ [111]. The muon spin interacts with the ordered electronic moments via dipole-dipole and transferred Fermi-contact interaction. Both interactions are sensitive to the distance between the muon spin and the iron ordered moments. Therefore, the nearly linear c dependence of f_A, f_B, and f_A/f_B implies, that the change of the frequency in the undoped compounds has a structural origin due to the increased distance between the FeAs layers.

The substitution of the alkaline-earth metals by alkaline metals, which introduces holes in the system, reveals an interesting behaviour. As shown in Fig. 5.6, the ionic radii scale like Ca < Na < Sr < Ba < K [93]. The influence of the alkaline metal substitution on the structural parameter is shown in Fig. 5.7(b), where the *c*-axis parameter normalized to the *c*-value of the corresponding undoped compound is shown. By substituting an alkaline-earth metal by an alkaline metal with a smaller ionic radius (Ba→Na [112], Sr→Na [98]), the change in the *c*-axis parameter is much smaller than by substituting with an alkaline metal with a larger ionic radius (Ca→Na [46], Ba→K [110], Sr→K [113, 114]). The increase of the *c*-axis parameter due to the substitution with a larger ion is intuitive as it results in a negative chemically induced pressure on the lattice. By the substitution with

(a)   (b)
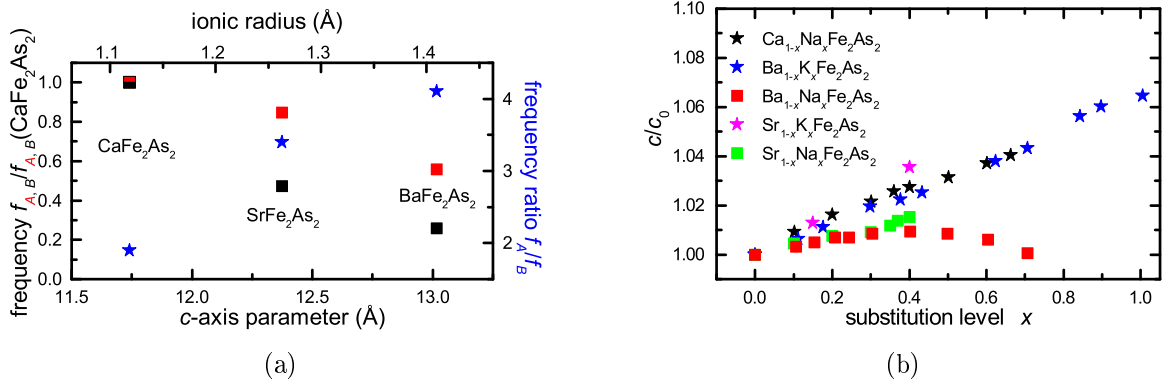
Figure 5.7.: (a) Normalized frequency f_A (red) and f_B (black) and the frequency ratio f_A/f_B (blue) as a function of the c-axis parameter and ionic radii of the alkaline-earth metals for the undoped compounds. f_A and f_B are normalized to the corresponding values of $CaFe_2As_2$ (52 MHz and 27.4 MHz). The linear reduction of f_A and f_B as well as the linear increase of f_A/f_B as a function of c, which is proportional to the ionic radius of the alkaline-earth metal, indicates a structural origin. f_B is reduced stronger than f_A as a function of c. Data taken from: $SrFe_2As_2$ [50] and $BaFe_2As_2$ [111]. (b) Substitution level x dependence of the c-axis parameter normalized to the c-axis parameter value of the corresponding undoped compound. Stars denote the substitution with a larger ion, while rectangles denote the substitution with a smaller ion. The substitution of an alkaline-earth metal by an alkaline metal with a smaller ionic radius (Ba→Na [112], Sr→Na [98]) results in a smaller change of the c-axis parameter compared to the substitution with an alkaline metal with a larger ionic radius (Ca→Na [46], Ba→K [110], Sr→K [113, 114]).

a smaller ion one would intuitively expect a reduction of the c-axis parameter due to the chemically induced pressure. Adding the oxidation state to the chemical formula results in $AE_{1-x}^{2+}A_x^+(FeAs)_2^{2-}$. The bonding between the $AE_{1-x}^{2+}A_x^+$- and the FeAs layer is of ionic character [115]. However, it is shown by Li and Ni, that the charge transfer from the AE atom to the FeAs layer is nearly twice as much as from the A atom [115]. Therefore, by substituting an alkaline-earth metal by an alkaline metal results in a weakening of the bonding of the $AE_{1-x}^{2+}A_x^+$- and $(FeAs)_2^{2-}$- layers [115]. This results in an increased c-axis parameter. As shown in Fig. 5.7(b), the c-axis parameter of $Ba_{1-x}Na_xFe_2As_2$ first increases up to $x \approx 0.4$ and than decreases for higher x. Therefore, after a critical Na-substitution level, the increase of the c-axis parameter due to the weakening of the bonds is exceeded by the reduction of the c-axis parameter due to the smaller ionic radius of the Na compared to Ba.

The frequency ratio f_A/f_B for different Na- and K-substitution levels is shown in Fig. 5.8(a). $BaFe_2As_2$ shows a ratio of 4.1 [111], which increases to 4.47 for $Ba_{0.77}K_{0.23}Fe_2As_2$ [111] or 4.5 for $Ba_{0.7}Na_{0.3}Fe_2As_2$ [65]. $SrFe_2As_2$ shows a ratio of 3.4 [50], which changes to 3.6 for $Sr_{0.5}Na_{0.5}Fe_2As_2$ [116].

(a)   (b)
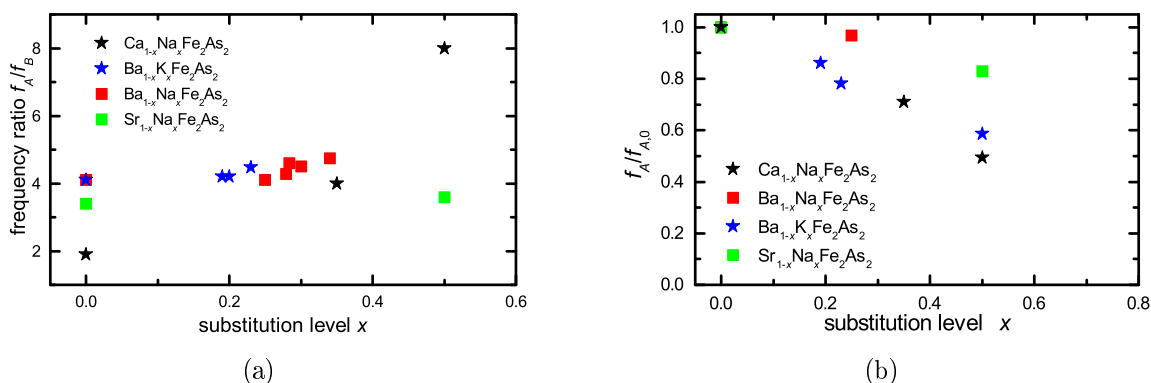
Figure 5.8.: (a) Frequency ratio f_A/f_B as a function of the substitution level x. The change in the frequency ratio in $Ca_{1-x}Na_xFe_2As_2$ is much larger compared to the doped Ba- and Sr-122 compounds. Substituting an alkaline-earth metal by an alkaline metal with a smaller ionic radius (Ba→Na [65], Sr→Na [116]), the change of the precession frequency ratio f_A/f_B occurs at higher substitution levels than by substituting with an alkaline metal with a larger ionic radius (Ca→Na, Ba→K [116]). A stronger change of f_A/f_B is observed for the latter case. (b) Substitution level x dependence of f_A normalized to the value for the corresponding undoped compound, $f_{A,0}$. It is shown, that the reduction of f_A is stronger for the case of the substitution of the alkaline-earth metal with a large ion than for the substitution with a smaller ion. In both figures, stars denote the substitution with a larger ion (Ca→Na, Ba→K [116]), while rectangles denote the substitution with a smaller ion (Ba→Na [65], Sr→Na [116]).

Therefore, by substituting an alkaline-earth metal by an alkaline metal with a smaller ionic radius (Ba→Na [65], Sr→Na [116]), the change of the precession frequency ratio

f_A/f_B occurs at higher substitution levels than by substituting with an alkaline metal with a larger ionic radius (Ca→Na, Ba→K [116]).

The reduction of the frequency f_A (normalized to the frequency value of the corresponding undoped compound) as a function of A substitution is shown in Fig. 5.8(b). The reduction of f_A for Ba→K and Ca→Na is of similar value, but stronger than for Ba→Na and Sr→Na. In conclusion, the changes in the frequency f_A and the frequency ratio f_A/f_B as a function of the alkaline (earth) metal substitution indicate a structural origin. However, an influence due to the hole-doping character of the alkaline metal substitution cannot be ruled out.

Now we turn to the Mössbauer results. Mössbauer spectra for characteristic temperatures in the paramagnetic and magnetically ordered states for $x = 0.35$ and 0.50 are shown in Fig. 5.9.
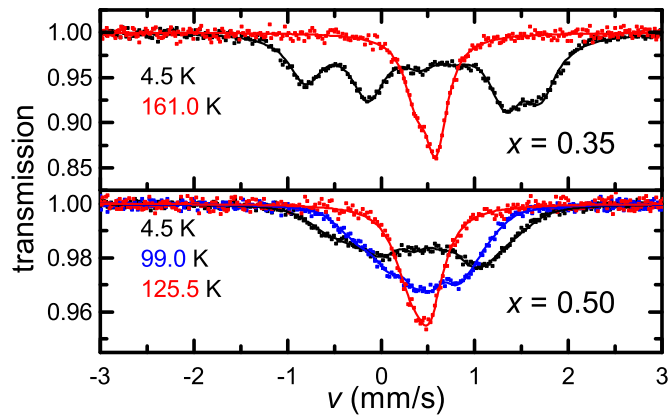
Figure 5.9.: Mössbauer spectra for representative temperatures in the paramagnetic and magnetically ordered temperature regime for $x = 0.35$ and 0.50. Lines are best fits.

In the paramagnetic state, an asymmetric doublet structure is observed for both samples, which is analysed using one doublet pattern. This shows, that all Fe nuclei experience the same electromagnetic environment. The asymmetry of the doublet $A_{doublet}$ is based on the angle φ between the incident γ-ray direction and the principal axis of the electric field gradient (EFG) and is described by [24]

$$A_{doublet}(\varphi) = \frac{1 + \cos^2(\varphi)}{\frac{2}{3} + \sin^2(\varphi)}. \tag{5.3}$$

As the experiment was performed using a mosaic of single crystals, the obtained value of φ is an effective value and can differ from the real value. It was shown by Alzamora *et al.* [117], that spectra, which are measured using a mosaic of single crystals, are more asymmetric than spectra, which are measured using one single crystal. This effect of an increased asymmetry is the case in the performed measurements, as the cleaving of the crystals leads to a distribution of orientation.

In the paramagnetic temperature regime, the space group is $I4/mmm$. The Fe nuclei are located at the 4d sites and have the point symmetry $\overline{4}m2$. This ensures axial symmetry (asymmetry parameter $\eta = 0$) and a finite EFG, whose principal axis is directed along the crystallographic c-direction. For $x = 0.00$, $V_{zz} = 12(1)$ V/Å^2 is reported [117]. At room temperature, a value of $V_{zz} = 11.2(5)$ V/Å^2 for $x = 0.35$ and 0.50 is obtained. With decreasing temperature, V_{zz} increases slightly to 13.0(5) V/Å^2 above the magnetic transition as it is shown in Fig. 5.10(a).
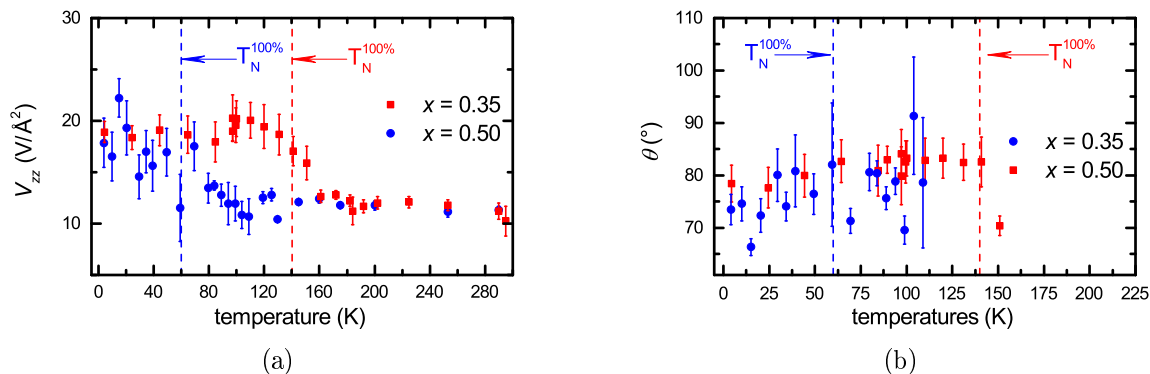
Figure 5.10.: (a) Temperature dependence of the main component of the EFG, V_{zz}. The step below 161 K for $x = 0.35$ and the gradual increase below 125 K for $x = 0.50$ corresponds to the magneto-structural phase transition. (b) Temperature dependence of the angle θ between the principal axis of the EFG and the magnetic hyperfine field B_{hf}. The vertical red and blue dashed lines in both pictures illustrate the highest temperatures, where 100 % of the sample show magnetic order.

With the onset of magnetic order, V_{zz} increases to 19(2) V/Å^2 and 18(3) V/Å^2 at $T_N^{100\%}$ for $x = 0.35$ and 0.50,respectively, and remains constants within error bars down to lowest measured temperatures. This increase can be assigned to a tetragonal-to-orthorhombic phase transition as it was seen und described for other 122 compounds including the parent compound CaFe$_2$As$_2$ [51, 52, 96, 118]. In the magnetically ordered state, the space group is assumed to be $Fmmm$ and, hence, has no axial symmetry, as all three crystallographic axes are inequivalent ($a{\neq}b{\neq}c$). In the experiments, no finite asymmetry parameter η was obtained within the resolution of the Mössbauer spectroscopy. Therefore, for the analysis of the spectra, η was set to zero. The temperature dependence of the angle θ between the principal axis of the EFG and the magnetic hyperfine field B_{hf} is shown in Fig. 5.10(b). For $x = 0.00$, $\theta = 94(4)°$ is reported [117]. Hence, the magnetic hyperfine field is located in the ab-plane, as the principal axis of the EFG is directed along the crystallographic c-axis [51, 117]. This supports the μSR result, that the iron magnetic moments are located in the ab-plane. For $x = 0.35$ and 0.50, $\theta = 80(5)°$ and 71(5)°, respectively, in the fully magnetically ordered state are obtained. Therefore, by increasing the Na-substitution level, a tilting of the iron magnetic moments out of the ab-plane occurs. This is consistent with the increase of the magnetic signal fraction in the 2,1-detector pair in the μSR experiments. Additionally, no change in θ is observed below

the superconducting transition temperature for $x = 0.50$ excluding a spin reorientation.

The onset temperature of the magnetic ordering, T_N^{onset}, is indicated by an abrupt increase of the Mössbauer linewidth w due to the appearance of a magnetic hyperfine field. This increase is shown in the inset of Fig. 5.4 resulting in $T_N^{onset} = 161$ K and $T_N^{onset} = 125$ K for $x = 0.35$ and 0.50, respectively. As described in Tab. 5.1, the temperature dependences of the magnetic volume fraction obtained by Mössbauer spectroscopy and μSR result in equal $T_N^{100\%}$. In the magnetically ordered state, a well-resolved sextet is observed in the Mössbauer spectra for $x = 0.35$, as it is shown in Fig. 5.9 at $T = 4.5$ K. This indicates static commensurate magnetic order with a well-defined hyperfine field. For $x = 0.50$, the sextet is less clear resolved and the spectra is modelled using a Gaussianly distributed magnetic hyperfine field. This takes into account the higher degree of disorder than in the sample with $x = 0.35$. Consistently, the μSR transverse relaxation rate λ^T is higher in $x = 0.50$ as can be seen by a much faster suppression of the ZF oscillation in Fig. 5.3.

For $CaFe_2As_2$, a magnetic hyperfine field of $B_{hf} = 10.14$ T at lowest temperatures is reported [117]. The temperature dependence of the obtained magnetic hyperfine field B_{hf} of $x = 0.35$ is shown in Fig. 5.5(a) with $B_{hf}(T\rightarrow 0) = 7.7$ T. In Fig. 5.5(b), the first moment of the Gaussian distribution of the magnetic hyperfine field for $x = 0.50$ is shown with $B_{hf}(T\rightarrow 0) = 4.9$ T. The temperature dependence of $B_{hf}(T)$ is analysed using Eq. (5.2). For $x = 0.35$, a fit to Eq. (5.2) above T_c for $B_{hf}(T)$ represents the data in the whole temperature range, i.e., also below the superconducting transition. Therefore, no interaction between the magnetic and superconducting order parameter is detectable. For $x = 0.50$, the magnetic hyperfine field shows no reduction and is well represented by Eq. (5.2) in contrast to the muon spin precession frequency, which shows a reduction of 7 %. The fact, that B_{hf} shows no signatures below T_c, may have several reasons: Either, because the reduction of 7 % is within the hyperfine field error bars or the muon precession frequency is changed due to a spin reorientation below T_c rather than a reduction of the magnetic order parameter. As mentioned earlier, a spin reorientation can be ruled out due to the fact, that the μSR time spectra, detected by detector pair 2,1, shows no changes below 50 K. It is also excluded by the Mössbauer spectroscopy data, as no change in θ is observed below the superconducting transition temperature

5.4.2. Landau theory of order-parameter coexistence

During the analysis of the magnetic order parameter in $Ca_{1-x}Na_xFe_2As_2$, the following question arises: When and with which magnitude is the magnetic order parameter reduced in 122 compounds in the case of a nanoscopic coexistence of long-range magnetic order and superconductivity? The simplest model to describe the problem is a Landau theory with coupled order parameters. The free energy functional in the absence of an external

field is given by [70, 119–121]

$$F[\psi, \vec{M}] = \int \mathrm{d}^3 r \left\{ \frac{\alpha}{2} |\psi(\vec{r})|^2 + \frac{\beta}{4} |\psi(\vec{r})|^4 + \frac{\gamma}{2} |\vec{\nabla}\psi(\vec{r})|^2 + \frac{d}{2} |\psi(\vec{r})|^2 |\vec{M}(\vec{r})|^2 \right. $$

$$\left. + \frac{a}{2} |\vec{M}(\vec{r})|^2 + \frac{b}{4} |\vec{M}(\vec{r})|^4 + \frac{g}{2} |\vec{\nabla}\vec{M}(\vec{r})|^2 \right\}, \tag{5.4}$$

where $\psi(\vec{r})$ is the superconducting and $\vec{M}(\vec{r})$ the magnetic order parameter. $\psi(\vec{r})$ is complex and described by an amplitude and a phase, while $\vec{M}(\vec{r})$ is a real three component tensor of first order. Following the common approaches, α and a are described as

$$a = a_0[T - T_{\mathrm{N}0}] \quad , \ a_0 > 0; \tag{5.5}$$

$$\alpha = \alpha_0[T - T_{c0}] \quad , \ \alpha_0 > 0, \tag{5.6}$$

where $T_{\mathrm{N}0}$ denotes the bare magnetic and T_{c0} the bare superconducting transition temperature. The bare transition temperature describes the decoupled case. $T_{c0} < T_{\mathrm{N}0}$ is assumed for the further treatment being the case in all 122 compounds, which are known at the time of writing of this thesis. This determines, that the bare magnetic transition temperature is equal to the measured magnetic transition temperature, $T_{\mathrm{N}0} = T_{\mathrm{N}}$. The superconducting transition temperature, T_c, which is measured in an experiment, might be reduced in the presence of magnetic order and, therefore, $T_c \leq T_{c0}$. To ensure, that the free energy has a definite minimum, $\beta > 0$, $b > 0$ and $d > -\sqrt{b\beta}$ are required. All interactions between the magnetic and superconducting order parameter are put into the term

$$\frac{d}{2} |\psi(\vec{r})|^2 |\vec{M}(\vec{r})|^2. \tag{5.7}$$

A negative d corresponds to a strengthening of both order parameters due to their interaction. This effect might be possible, but is beyond the scope of this discussion. Therefore, to ensure an order parameter competition, d is set to be strictly positive. Assuming the spatial homogeneity of both order parameters results in a vanishing of the gradient terms in Eq. (5.4). Minimizing the free energy functional with respect to ψ^* and $\vec{M}$ gives

$$0 = \alpha\psi + \beta|\psi|^2\psi + d|\vec{M}|^2\psi, \tag{5.8}$$

$$0 = a\vec{M} + b|\vec{M}|^2\psi + d|\psi|^2\vec{M}. \tag{5.9}$$

This system of equations has the following solutions resulting in different phases depending on the values of the parameters. The paramagnetic and normal conducting phase correspond to $\psi = 0$ and $\vec{M} = 0$ with $a, \alpha > 0$. The magnetic and normal conducting phase is given by $\psi = 0$ and $\vec{M}^2 = -a/b$ with $a < 0$ and $\alpha b > ad$. The paramagnetic and superconducting phase corresponds to $\psi = -\alpha/\beta$ and $\vec{M} = 0$ with $\alpha < 0$ and $a\beta > \alpha d$.

5. Mössbauer and muon spin relaxation spectroscopy of $Ca_{1-x}Na_xFe_2As_2$

The solution of coexistence of both order parameters is given by

$$|\psi|^2 = -\frac{\alpha b - ad}{b\beta - d^2} \quad , \; \alpha b < ad; \tag{5.10}$$

$$\vec{M}^2 = -\frac{a\beta - \alpha d}{b\beta - d^2} \quad , \; a\beta < \alpha d, \tag{5.11}$$

if the coupling is sufficiently small and fulfils the equation $b\beta - d^2 > 0$. The conditions $\alpha b < ad$ and $a\beta < \alpha d$ are a result of $|\psi|^2$ and $\vec{M}^2$ being real. At T_c, where $|\psi|^2 = 0$, Eq. (5.10) reduces to

$$|\psi(T_c)|^2 = 0 = \alpha(T_c)b - a(T_c)d = \alpha_0 b[T_c - T_{c0}] - a_0 d[T_c - T_N], \tag{5.12}$$

which results in an expression for the measured and bare superconducting transition temperature as a function of each other,

$$T_c = \frac{\alpha_0 b T_{c0} - a_0 d T_N}{\alpha_0 b - a_0 d}, \tag{5.13}$$

$$T_{c0} = \frac{a_o d}{\alpha_0 b} T_N + \left[1 - \frac{a_0 d}{\alpha_0 b}\right] T_c, \tag{5.14}$$

and the magnetic transition temperature. The temperature dependence of the magnetic order parameter in the coexistence region, using Eqs. (5.5), (5.6), (5.11) and (5.14) as well as basic maths, is consequently given by

$$\vec{M}_{co}^2(T) = \frac{1}{b\beta - d^2} \left\{ [\alpha_0 d - a_0 \beta]T + \left[a_0\beta - \frac{a_0}{b}d^2\right]T_N - \left[1 - \frac{a_0 d}{\alpha_0 b}\right]T_c \right\}, \tag{5.15}$$

for $T \leq T_c \leq T_N$. As the magnetic order parameter decreases below T_c with decreasing temperature, the first derivative of Eq. (5.15) must obey

$$\frac{d\vec{M}^2}{dT} > 0, \tag{5.16}$$

leading to the condition $\alpha_0 d > a_0 \beta$. To investigate the reduction of the magnetic order parameter in the coexistence region, the ratio of $\vec{M}_{co}^2$ and $\vec{M}_0^2$ at a given $T \leq T_c \leq T_N$ is calculated:

$$\frac{\vec{M}_{co}^2}{\vec{M}_0^2}(T) = \frac{1}{b\beta - d^2} \left\{ \frac{T}{T_N - T}\left[\frac{\alpha_0}{a_0}bd - b\beta\right] + \frac{T_N}{T_N - T}\left[b\beta - d^2\right] \right.$$
$$\left. - \frac{T_c}{T_N - T}\left[\frac{\alpha_0}{a_0}bd - d^2\right] \right\}. \tag{5.17}$$

The reduction, which is described by Eq. (5.17), is maximal for $T = 0$, resulting in

$$m_{\mathrm{red}} = \frac{\vec{M}_{\mathrm{co}}^2}{\vec{M}_0^2}(T=0) = 1 - \underbrace{\frac{d}{a_0}\frac{\alpha_0 b - a_0 d}{b\beta - d^2}}_{\Delta m(d,a_0,\alpha_0,b,\beta)}\frac{T_c}{T_{\mathrm{N}}}. \tag{5.18}$$

Several conclusions can be drawn from this equation. m_{red} is reduced as a function of T_c/T_{N} with the slope $\Delta m(d, a_0, \alpha_0, b, \beta)$. In the limit of zero coupling ($d \to 0$), $m_{\mathrm{red}} \to 1$, and $\Delta m \to 0$ and, therefore, no reduction of $\vec{M}_{\mathrm{co}}(0)$ occurs corresponding to the decoupled case. The interpretation of Δm is not straightforward, as Δm is non-trivially connected to the experimentally accessible parameters a_0/b and α_0/β.

Comparing the theoretical result with experimental data gives further insight. In Fig. 5.11, m_{red}, determined by neutron scattering and μSR experiments for various doped 122 compounds, is shown [65, 111, 122–131]. Additionally, the reduction of the structural order parameter $S = (a\text{-}b)/(a\text{+}b)$ is shown in Fig. 5.11. The reduction of the structural and magnetic order parameter reveals the same behaviour as a function of T_c/T_{N}, as both order parameters are strongly coupled in the 122 compounds [50–52, 132–135]. $m_{\mathrm{red, exp}}$ reveals a linear decrease as a function of T_c/T_{N} for $T_c/T_{\mathrm{N}} < 0.7$, which corresponds to a constant slope $\Delta m \approx 0.75$ in Eq. (5.18). $\Delta m = $ constant is a possible realization of the following parameter settings of d, a_0/b and α_0/β:

i) d, a_0/b and α_0/β are constant

ii) d and α_0/β are constant

iii) d and a_0/b are constant

iv) a_0/b and α_0/β are constant

v) a_0/b is constant

vi) α_0/β is constant

vii) d is constant

viii) no constant parameter.

The observed muon spin precession frequency in $\mathrm{Ca}_{1-x}\mathrm{Na}_x\mathrm{Fe}_2\mathrm{As}_2$ is proportional to the magnetic order parameter. Therefore, the ratio a_0/b can be calculated in the purely magnetic phase for $T \gg T_c$ in the vicinity of the magnetic phase transition using $M^2 = a_0/b \cdot [T_{\mathrm{N}} - T]$. $a_0/b \approx 16.2\ \mathrm{MHz}^2/\mathrm{K}$, $9.5\ \mathrm{MHz}^2/\mathrm{K}$, and $6.3\ \mathrm{MHz}^2/\mathrm{K}$ for $x = 0.00$, 0.35, and 0.50, respectively, are obtained. Therefore, a_0/b is not constant in the 122 compounds.

The superconducting order parameter can be calculated using Eq. (2.66) with $|\psi|^2 = 2n_s$ [19], which results in $|\psi|^2 = [T_c - T]\alpha_0/\beta \propto \lambda^{-2}$ and, therefore, $\alpha_0/\beta \propto \lambda^{-2}T_c^{-1}$. However, values of $\lambda = 200$ nm and $T_c = 34$ K in $\mathrm{Ca}_{0.33}\mathrm{Na}_{0.67}\mathrm{Fe}_2\mathrm{As}_2$ as well as $\lambda = 320$ nm and $T_c = 32$ K in $\mathrm{Ba}_{1-x}\mathrm{K}_x\mathrm{Fe}_2\mathrm{As}_2$ [136] indicate a non-constant parameter ratio α_0/β. In summary, it can be stated, that the cases i)-vi) are not realized in the 122 compounds.

a_0/b shows a linear decrease with increased doping level and hence can be approximated by $a_0^x/b^x = a_0^0/b^0 \, [1 - \Delta(a/b)]$, where a_0^0 and b^0 denote the corresponding parameter for the undoped magnetic compounds. For $Ca_{1-x}Na_xFe_2As_2$, $\Delta(a/b) = -20(2) \times x$, with the Na-substitution level $x \in [0.00; 0.67]$. The linearity of the doping dependence of $\alpha_0/\beta \propto \lambda^{-2}T_c^{-1}$ cannot be proven for the $Ca_{1-x}Na_xFe_2As_2$-series, as only λ values for $x = 0.50$ and 0.67 are available in the literature. For the doped $BaFe_2As_2$ compounds, more data is available. It can be shown, using the data published by Prozorov and Kogan [137] that α_0/β shows a linear doping dependence similar to a_0/b. Hence, it can be approximated using $\alpha_0/\beta = \alpha_0^0/\beta^0 \times \Delta(\alpha_0/\beta)$, where α_0^0 and β^0 denote the corresponding parameter for the undoped superconducting compounds. $\Delta(\alpha_0/\beta)$ is a linear function of the doping level x. However, due to the similar properties in the 122 compounds, it is assumed, that the doping dependence of a_0/b and α_0/β is always of linear type for each doping series. This linear doping dependence indicate a constant coupling d (case vii) in the 122 compounds. In Fig. 5.11, it is visible, that no reduction of the magnetic order parameter occurs for
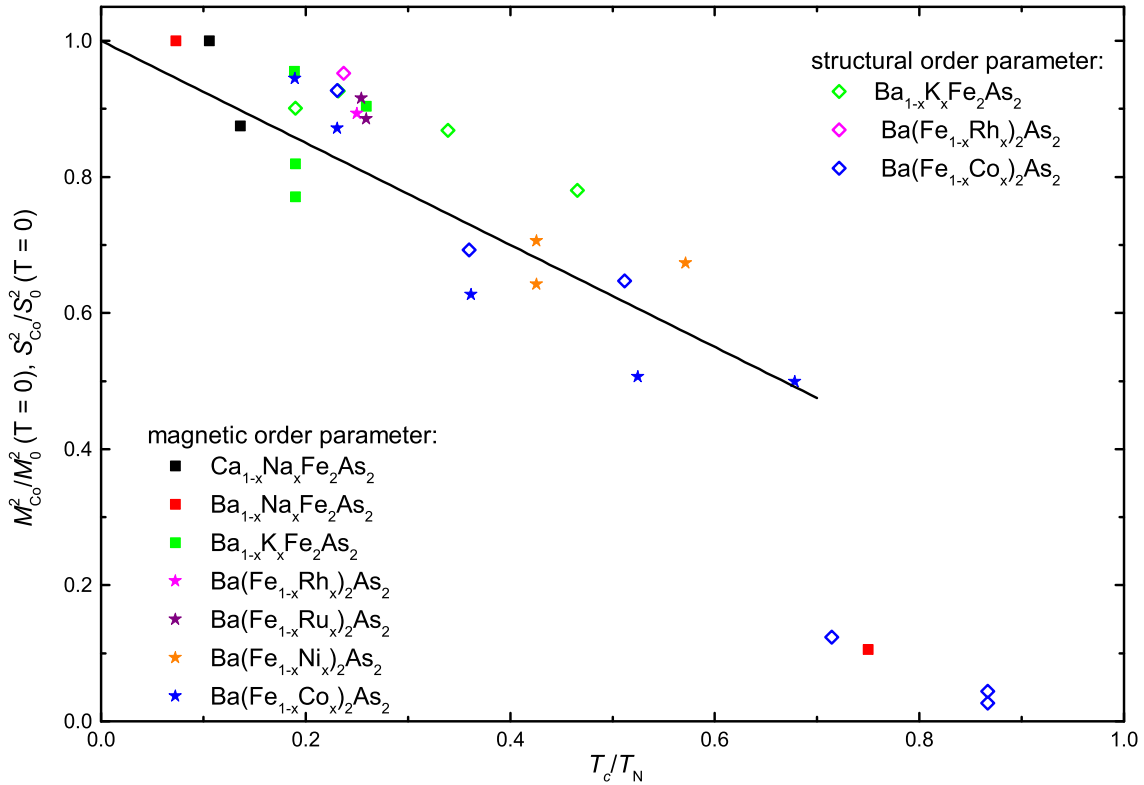
Figure 5.11.: Magnetic (M) and structural (S) order parameter reduction as a function of T_c/T_N. M_{co} and S_{co} denote the order parameter in the coexistence region, while M_0 and S_0 denote the bare order parameter. The solid line corresponds to Eq. (5.18). Data taken from Refs. $Ba_{1-x}Na_xFe_2As_2$ [65], $Ba_{1-x}K_xFe_2As_2$ [111, 122, 123], $Ba(Fe_{1-x}Ru_x)_2As_2$ [124], $Ba(Fe_{1-x}Rh_x)_2As_2$ [125, 126], $Ba(Fe_{1-x}Ni_x)_2As_2$ [127], and $Ba(Fe_{1-x}Co_x)_2As_2$ [125, 128–131].

$0 < T_c/T_N \approx 0.1$. This has several reasons. For $T_c/T_N \approx 0$, due to the experimental

resolution, a reduction of the order parameter may not be resolved. Additionally, the compounds may not show bulk superconductivity, but only in parts of the sample. This is, e. g., the case for $Ca_{0.65}Na_{0.35}Fe_2As_2$, where only parts of the volume are superconducting and no reduction of the magnetic order parameter is observed. Also, it is difficult to determine $M(T{\rightarrow}0)$ in the presence of a superconducting phase due to the reduction of the magnetic order parameter in the coexistence region. For the majority of the literature data, only $M(T_c)$ is available and used in Fig. 5.11. The resulting error can be estimated by the described μSR experiment on $Ca_{0.50}Na_{0.50}Fe_2As_2$. $M(T_c) = 27.5$ MHz and $M_{co}(T \rightarrow 0) = 26$ MHz are obtained by the experiment, while $M(T \rightarrow 0) = 28$ MHz is calculated using Eq. (5.2). The reduction is than given by $M_{co}(T \rightarrow 0)/M(T_c) \approx 5$ % and $M_{co}(T \rightarrow 0)/M(T \rightarrow 0) \approx 7$ %. The corresponding reduction of the magnetic order parameter is than given by $M_{co}^2(T \rightarrow 0)/M^2(T_c) \approx 0.89$ and $M_{co}^2(T \rightarrow 0)/M^2(T \rightarrow 0) \approx 0.86$. The difference between both reduction values is ≈ 3.5 %, which is of the order of the dot size in Fig. 5.11. This approximation is appropriate, if $M(T \rightarrow 0) \approx M(T_c)$, which is the case for $T_c/T_N \ll 1$. For $T_c/T_N \rightarrow 1$, $M(T \rightarrow 0) \approx M(T_c)$ is not secured. In this case, $M(T_c) < M(T \rightarrow 0)$ and, hence, m_{red} is overestimated. Therefore, the limitations of the data extraction cannot explain the systematic deviations of the data from Eq. (5.18) in the range $0.7 \lesssim T_c/T_N < 1$. This indicates a change of the slope in Eq. (5.18), which can be consistently described with case vii: For $T_c/T_N < 0.7$, a similar coupling strength $d \approx$ constant of the magnetic and superconducting order parameter results in $\Delta m = $ constant. With increasing T_c/T_N, Δm changes for $T_c/T_N > 0.7$ and hence the constant value of d is changed. However, if $T_c \approx T_N$, higher order terms in $\vec{M}$ and ψ may have to be considered.

In summary, a qualitative description of the reduction of the magnetic order parameter in the coexistence region as a function of T_c/T_N is given. For a quantitative treatment of the problem with Landau theory, the parameters α and a have to be calculated using a microscopic theory. This would also put the argumentation about the similar coupling strength of the superconducting and magnetic order parameter in the 122 compounds on a more robust basis.

5.4.3. Magneto-structural phase transition

When a nucleus absorbs a photon, the phonon system remains unchanged with a probability f, where f is the recoilless fraction. This probability depends on the phonon spectra. Therefore, by analysing f, informations about the phonon spectra can be obtained. As described in Sec. 3.4, the temperature dependence of f in Debye approximation is given by

$$f = \exp\left(-\frac{3E_R}{2k_B\theta_D}\left\{1 + 4\left[\frac{T}{\theta_D}\right]^2 \int_0^{\theta_D/T} \frac{x}{e^x - 1}dx\right\}\right), \qquad (5.19)$$

with the recoil energy E_R, Boltzmann's constant k_B and the Debye temperature θ_D. In the Mössbauer experiments, the area of the total spectrum A and the baseline I_0 are extracted from the Mössbauer spectra. The quantity $A_N = A/I_0$ is proportional to f [138]. Therefore, by analysing the temperature dependence of A_N, the temperature dependence of f can be obtained, but statements about absolute values of f cannot be

made. f is then given by

$$f = CA_N(T), \tag{5.20}$$

where C is a positive constant. The temperature dependence of $A_N(T)$, normalized to the value $A_N(T = 4.2$ K), for $x = 0.35$, 0.50, and 0.67 is shown in Fig. 5.12(a). For $x = 0.35$ and 0.50, $A_N(T)/A_N(4.2$ K) is well-described by Eq. (5.20) in the fully magnetically ordered state as well as in the paramagnetic state. The step at 161 K for $x = 0.35$ and the gradual increase between 60 K and 125 K is attributed to the splitting of former overlapping transition lines due to the magnetic phase transition, which leads to an increase of the effective absorption area [24, 139]. Debye temperatures of $\theta_D^{PM} = 200(32)$ K and 203(12) K as well as $\theta_D^{AFM} = 208(16)$ K and 219(28) K for $x = 0.35$ and 0.50, respectively, are obtained. For $x = 0.67$, Eq. (5.20) describes $A_N(T)/A_N(4.2$ K) for all investigated temperatures . The obtained Debye temperatures θ_D are summarized in Tab. 5.2.

x	θ_D^{PM}/K	θ_D^{AFM}/K
0.00	272	271
0.35	200(32)	208(16)
0.50	203(12)	219(28)
0.67	213(6)	

Table 5.2.: Debye temperatures θ_D obtained using Eq. (5.19) above (PM) and below (AFM) the magnetic phase transition. Data for $x = 0.00$ are taken from Ref. [140]

The Debye temperatures θ_D^{PM} and θ_D^{AFM} do not change within error bars at the phase transition. This shows, that the lattice dynamics does not change at the magneto-structural phase transition. Additionally, θ_D is constant for all finite x. Therefore, the lattice dynamics is independent of the Na-substitution level in the investigated substitution range $0.35 \leq x \leq 0.67$. In contrast to the undoped compound, CaFe$_2$As$_2$ with $\theta_D = 270$ K, the lattice is softer [140] . Therefore, the lattice dynamics change between the undoped compound $x = 0$ and the investigated Na-substitution range $0.35 \leq x \leq 0.67$.

To further study the properties of the magneto-structural phase transition, the temperature dependence of the center shift δ is analysed. δ is a measure for the electron density at the Fe nucleus. Comparing the room temperature values of δ, a Na-substitution level independent value of $\delta = 0.40(1)$ mm/s for $x = 0.35$, 0.50, and 0.67 is observed. The undoped compound shows an isomer shift of $\delta = 0.43$ mm/s [117]. Therefore, the electron density at the Fe nucleus is increased upon Na substitution. As described in Sec. 3.6.1, the temperature dependence of the center shift, which is shown in Fig. 5.12(b), is the sum of the temperature-independent chemical shift δ_C and a temperature-dependent contribution $\delta_R(T)$ due to the second-order Doppler shift,

$$\delta(T) = \delta_C + \delta_R(T), \tag{5.21}$$

$$\delta_R(T) = -\frac{9}{16} \frac{k_B}{M_{\text{eff}}\, c} \left\{ \theta_D + 8T \left[\frac{T}{\theta_D}\right]^3 \int_0^{\theta_D/T} \frac{x^3}{e^x - 1} dx \right\},$$

where M_{eff} denotes the effective vibrating mass of the ^{57}Fe atom. The chemical shift is
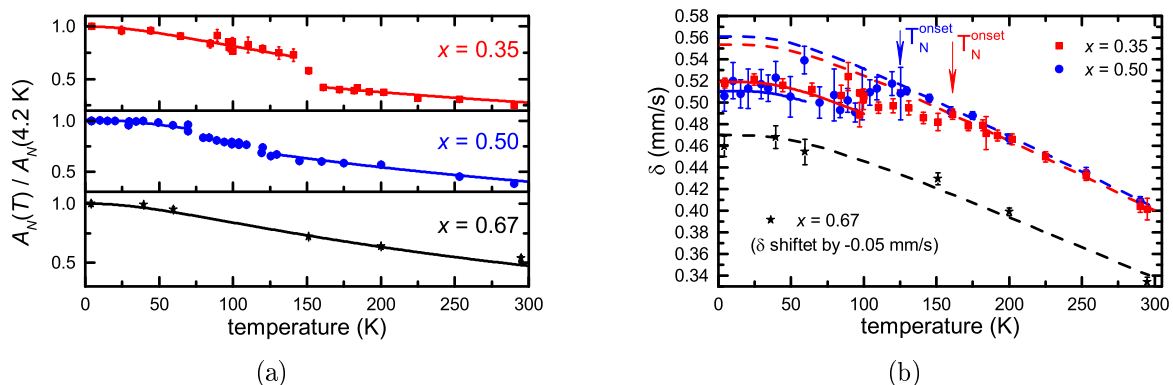
Figure 5.12.: (a) Temperature dependence of the relative recoilless fraction $A_N(T)/A_N(4.2 \text{ K})$ including best fits following Eq. (5.19). (b) Temperature dependence of the center shift. The solid lines are a fit in the paramagnetic temperature regime and the dashed lines are a fit in the magnetically ordered temperature regime using Eq. (5.21) with $\theta_\mathrm{D} = 200$ K and 203 K for $x = 0.35$ and 0.50, respectively. The deviation from $\delta^\mathrm{PM}(T)$ corresponds to the magneto-structural transition, which causes a change in the electron density at the nucleus. For $x = 0.67$, δ is shifted by -0.05 mm/s for illustration purposes.

calculated using $\delta_\mathrm{C} = \delta(0) - \delta_\mathrm{R}(0)$.

To study the influence of the magneto-structural phase transition on the center shift, its temperature dependence is analysed. Analysing $\delta(T)$ in the paramagnetic state with a fixed θ_D, which is obtained by Eq. (5.20), gives $\delta^\mathrm{PM}(T)$ and $M_\mathrm{eff}^\mathrm{PM}$ and $\delta_\mathrm{C}^\mathrm{PM}$ can be calculated. $\delta^\mathrm{PM}(T)$ reveals similar behaviour for both samples leading to $\delta_\mathrm{C}^\mathrm{PM} = 0.61(3)$ mm/s and $\delta_\mathrm{C}^\mathrm{PM} = 0.60(1)$ mm/s for $x = 0.35$ and 0.50. The effective vibrating mass has, within error bars, the same value $M_\mathrm{eff}^\mathrm{PM} = 60(1)$ u for both samples, which is slightly enhanced compared to the 57 u of a free ^{57}Fenucleus due to the bonding of the nucleus in the crystal lattice. Applying the resultant temperature dependence $\delta^\mathrm{PM}(T)$ to the full temperature range, one can see, that systematic deviations from the behaviour in the paramagnetic state occur below the magneto-structural phase transition.

Analysing the magnetically ordered state (AFM) with the same θ_D as in the paramagnetic state, $\delta^\mathrm{AFM}(T)$ is obtained and $M_\mathrm{eff}^\mathrm{AFM}$ and $\delta_\mathrm{C}^\mathrm{AFM}$ can be calculated. $M_\mathrm{eff}^\mathrm{AFM}$ has the same value as in the paramagnetic state. Therefore, $M_\mathrm{eff} = M_\mathrm{eff}^\mathrm{AFM} = M_\mathrm{eff}^\mathrm{PM}$ is defined. This constant M_eff indicates no significant change in the bonding of the nucleus due to the magneto-structural phase transition. Values of $\delta_\mathrm{C}^\mathrm{AFM} = 0.57(1)$ mm/s and $\delta_\mathrm{C}^\mathrm{AFM} = 0.56(1)$ mm/s are obtained for $x = 0.35$ and 0.50, respectively.

Both $\delta^\mathrm{PM}(T)$ and $\delta^\mathrm{AFM}(T)$ have the same temperature dependence due to the same θ_D and M_eff and only vary in the values of δ_C. The experimental data is described by $\delta^\mathrm{PM}(T)$ at temperatures above 161 K and 125 K and by $\delta^\mathrm{AFM}(T)$ at temperatures below 100 K and 60 K for $x = 0.35$ and 0.50, respectively. Therefore, a change of δ_C occur in this intermediate temperature regime. $\delta_\mathrm{C}^\mathrm{PM}$ is reduced to $\delta_\mathrm{C}^\mathrm{AFM} = 0.57(1)$ mm/s and 0.56(1) mm/s for $x = 0.35$ and 0.50, respectively. These reductions in the chemical shifts

correspond to an increase of the electron density at the nucleus [24]. The origin of the change of the electron density at the nucleus can be the structural and/or the magnetic phase transition. The change from a tetragonal to an orthorhombic structure changes the lattice parameters and hence the volume of the unit cell, which may change the chemical shift [24]. An increase of the volume and, hence, an increase of the Fe-As distance results in a decrease of the electron density at the nucleus corresponding to an increased δ_C [140]. This behaviour is, for example, observed in non-magnetic FeSe, which shows an increase of δ_C of 0.006(1) mm/s at the tetragonal-to-orthorhombic phase transition [141]. A magnetic phase transition may change the chemical shift, as it was observed in metallic iron at the Curie temperature, where no structural phase transition occurs [142]. The reduction of δ_C in metallic iron due to the magnetic phase transition is ≈ 0.3 mm/s [142]. This indicates, that the origin of the change of the chemical shifts is of both magnetic and structural nature. However, Mössbauer measurements on the undoped compound show either no change [117], an increase [140] or a decrease [143] of the chemical shift. The measurements on samples with $x > 0$ indicate, that a reduction of the isomer shift at the magneto-structural phase transition of $CaFe_2As_2$ is the most probable case. For $x = 0.67$, the temperature dependence of $\delta(T)$ can be properly described by Eq. (5.21) and a value of $\delta_C = 0.56(1)$ mm/s was obtained. Therefore, no signs of a magnetic or structural phase transition were obtained.

5.4.4. Optimally doped $Ca_{0.33}Na_{0.67}Fe_2As_2$
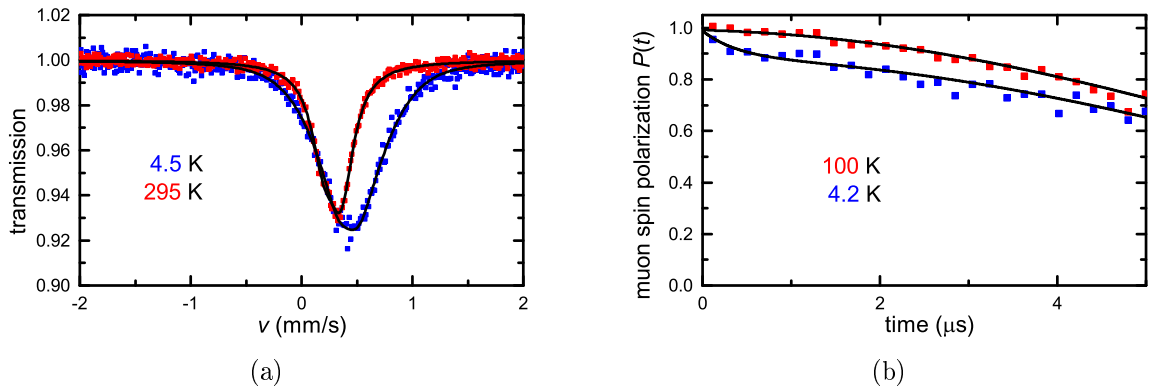
Figure 5.13.: (a) Mössbauer spectra and (b) μSR time spectra in the paramagnetic and superconducting phase.

For $Ca_{0.33}Na_{0.67}Fe_2As_2$, magnetic susceptibility measurements evidence bulk superconductivity below $T_c = 34$ K, as shown in Fig. 5.2(b). Mössbauer experiments where performed at temperatures below 60 K and above 151 K. The Mössbauer spectra, which are shown in Fig. 5.13(a) exhibit an asymmetric doublet structure with $V_{zz} = 10.3(2)$ V/Å² at 295 K. V_{zz} remains constant within error bars down to lowest temperatures excluding a structural phase transition. This V_{zz} value is ≈ 8 % smaller than for $x = 0.35$ and 0.50. Therefore, the deviation form the perfect FeAs₄ tetrahedron is smaller for $x = 0.67$. However, the superconducting transition is sensitive to the distortion of this tetrahedron and
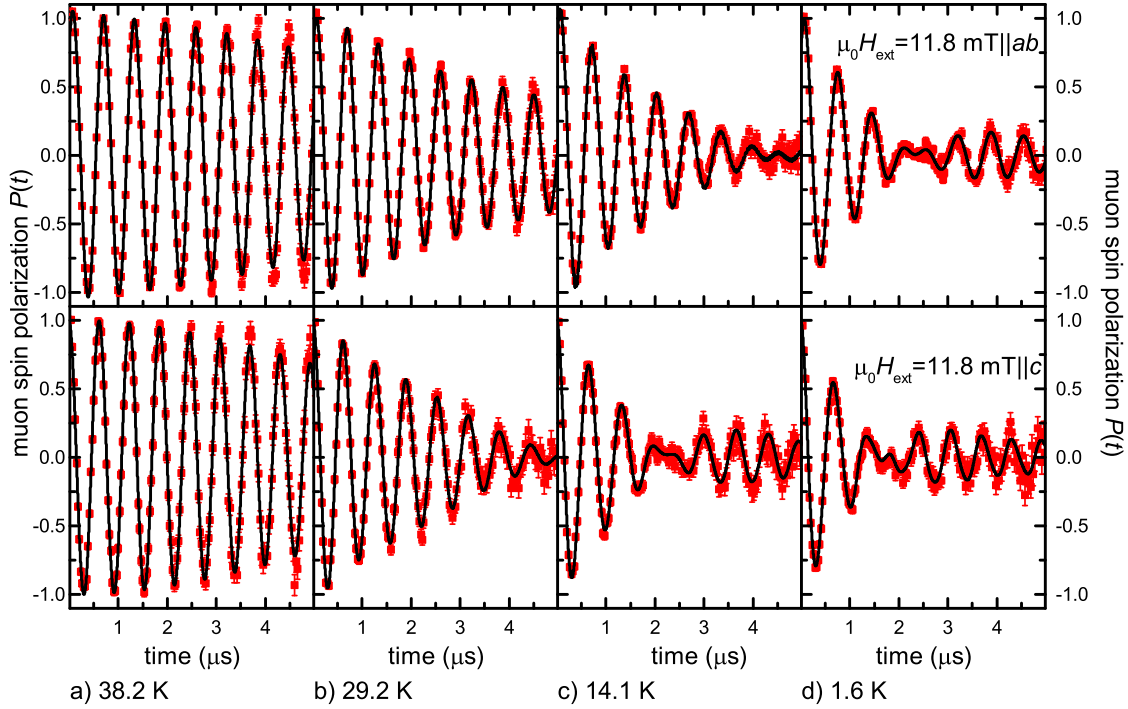
Figure 5.14.: TF-μSR spectra for $x = 0.67$ with $\mu_0 H_{ext}$=11.8 mT$\|ab$ (upper row) and $\mu_0 H_{ext}$=11.8 mT$\|c$ (lower row) for temperatures above and below the superconducting transition temperature, $T_c = 34$ K. The small Gaussian damping in spectrum (a) is attributed to the dipole-dipole interaction of the muon spin with randomly oriented dense nuclear moments. The additional damping in spectra (b)-(d) is caused by the formation of a vortex lattice in the superconducting state and the associated internal magnetic field distribution $n(B)$. It is clearly visible, that the damping of the muon precession is stronger in the $\mu_0 H_{ext} = 11.8$ mT$\|c$ case.
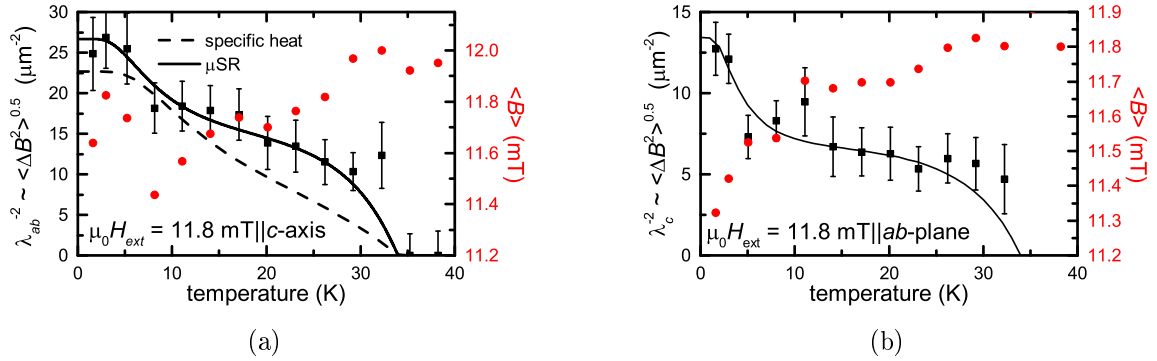
Figure 5.15.: Temperature dependence of the magnetic penetration depths (a) $\lambda_{ab}^{-2}(T)$ and (b) $\lambda_c^{-2}(T)$, which are proportional to the superfluid density, and the average magnetic field determined by TF-μSR. The reduction of the average magnetic field is caused by the diamagnetic shielding of the superconducting state. The solid line is the best fit with a phenomenological α model [20]. The dashed line illustrates the temperature dependence of λ^{-2} obtained by specific-heat measurements with the parameter $\Delta_1 = 2.35$ meV, $\Delta_2 = 7.5$ meV, W(Δ_1) = 0.75 and $\lambda(0) = 210$ nm [100, 144].

T_c is enhanced for less distorted tetrahedra [145].

The broadening of the Mössbauer spectra below 60 K cannot be explained by neither an increase of V_{zz} nor an increase of the linewidth w. Therefore, this broadening indicates the existence of small magnetic fields, which were modelled using a Gaussian distribution with the first moment $\langle B \rangle = 0$. The standard deviation of this Gaussian distribution is constant within error bars $\sigma(B) = 2.2(1)$ T above T_c and decreases in the superconducting phase to 1.7(1) T at 4.2 K. This indicates a competition between magnetism and superconductivity. Additionally, the spectra are nearly symmetric below 60 K and an angle $\theta = 55(5)°$ between the principal axis of the EFG and the magnetic hyperfine field, which is close to the magic angle, is obtained. ZF μSR experiments, which were measured for temperatures below 40 K and above 75 K, down to 5 K are shown in Fig. 5.3. The time evolution of the muon spin polarization exhibit a Gauss-Kubo-Toyabe depolarization above 75 K excluding any electronic magnetic order. Below 40 K, a weak exponential relaxation proves short-range magnetic order in small volume fractions with a MVF < 20 %. By combining both local probes, the onset temperature of the magnetic order is estimated to be $60 < T_N^{onset} < 75$ K. However, room-temperature Mössbauer measurements as well as the sharp superconducting transition observed via magnetic-susceptibility measurements indicate a homogeneous sample. This indicates, that the weak magnetism is diluted and disordered and persistent even in the optimal doping regime, as it was seen in other iron pnictides. [36, 63, 146]

For an investigation of the superconducting phase ($T_c = 34$ K), TF-μSR measurements were performed in external magnetic fields of $\mu_0H_{ext} = 11.8$ mT perpendicular and parallel to the crystallographic c-axis. The magnetic field was applied at $T > T_c$ and the corresponding time evolution of the muon spin polarization is shown in Fig. 5.14(a). The

damping above T_c is caused by the dipole-dipole interaction of the muon spin with randomly oriented dense nuclear moments. Subsequent cooling of the sample in the external field with $\mu_0 H_{c1} < \mu_0 H_{ext} < \mu_0 H_{c2}$ below the superconducting transition temperature causes the formation of a vortex lattice. The superconducting signal fraction is fully damped after 2-3 μs and ≈ 18 % residual signal fraction is still oscillating with a precession frequency equal to the applied field at times $t > 3$ μs. Identifying this ≈ 18 % signal fraction with the MVF obtained by ZF-μSR measurements, which is of equal value, show, that the internal magnetic fields are small compared to the 11.8 mT applied field.

The vortex lattice and the associated magnetic field distribution $n_{\perp,\|c}(B)$ causes an additional Gaussian damping. The corresponding time evolution of the muon spin polarization is shown in Fig. 5.14(b-d). Measuring the magnetic field distribution within the vortex lattice, the magnetic penetration depth can be obtained via Eq. (2.63). The resulting temperature dependence of the inverse squared magnetic penetration depth, $\lambda^{-2}(T)$, is shown in Fig. 5.15(a) and Fig. 5.15(b) together with the first moment $\langle B \rangle$ of the internal magnetic field distribution $n_{\perp,\|c}(B)$. $\langle B \rangle$ shows a reduction due to the diamagnetic shielding below the superconducting transition. For $\mu_0 H_{ext}{=}11.8$ mT$\|c$, $\langle B \rangle$ increases at lowest temperatures, which is unexpected in the superconducting phase. The effect may be caused by field induced magnetism [147–149], vortex disorder [147], or a decrease of the spin susceptibility, which is concealed by the diamagnetic shielding [150, 151].

$\lambda^{-2}(T)$ is modelled using the phenomenological α model including two independent superconducting gaps with s-wave symmetry [20]. The results are shown in Tab. 5.3. The obtained values for the larger superconducting energy gap are in reasonable agreement with recent ARPES and specific-heat measurements on single crystals from the same batch with the same composition [77, 100]. Using the measurements with $\mu_0 H_{ext}\|c$, the in-plane penetration depth $\lambda_{ab}(0){=}$ 194(17) nm can be directly calculated. For $\mu_0 H_{ext}\|ab$, contributions from both λ_{ac} and λ_{bc} are measured. Let λ_{eff} be the measured magnetic penetration depth for the case $\mu_0 H_{ext}\|ab$, and is given by $\lambda_{eff}{=}\sqrt{\lambda_{ac}\lambda_{bc}}$ [152]. Assuming $\lambda_a \approx \lambda_b$ and using $\lambda_{ab} = \sqrt{\lambda_a\lambda_b}$, $\lambda_{ac} = \sqrt{\lambda_a\lambda_c}$ and $\lambda_{bc} = \sqrt{\lambda_b\lambda_c}$, a value for λ_c can be estimated using $\lambda_c = \lambda_{eff}^2/\lambda_{ab}$, where a value of $\lambda_c(0){=}$ 280(46) nm is obtained. As disorder in the vortex lattice would artificially reduce the penetration depth due to the broadening of $n(B)$, λ_{ab} and λ_c describe strictly lower limits only (and λ^{-2} an upper limit).

	$\Delta_1(0)/$meV	$\Delta_2(0)/$meV	$w(\Delta_1)$	$\lambda(0)/$nm
$\mu_0 H_{ext}\perp c$	0.57(8)	6.7(1.3)	0.49(4)	280(46)
$\mu_0 H_{ext}\|c$	0.8(3)	6(1)	0.46(8)	194(17)
ARPES [77]	2.3	7.8		
spec. heat [100, 144]	2.35	7.5	0.75 [100]	210(10) [144]

Table 5.3.: Superconducting gap and penetration depth values obtained by a phenomenological α model analysis of λ^{-2} for an applied external field parallel and perpendicular to the crystallographic c-axis. $\Delta_i(0)$ denotes the zero temperature values of the gaps. $w(\Delta_1)$ and $w(\Delta_2){=}1{-}w(\Delta_1)$ are the corresponding weighting factors. $\lambda(0)$ denotes the zero temperature penetration depth.

Therefore, the obtained values for the magnetic penetration depths are reduced com-

pared to the values obtained by, e.g. specific-heat experiments. To illustrate this effect, the temperature dependence of $\lambda_{\text{spec. heat}}^{-2}(T)$ with the corresponding parameters ($\Delta_1 = 2.35$ meV, $\Delta_2 = 7.5$ meV, $w(\Delta_1) = 0.75$, and $\lambda(0) = 210$ nm) obtained by specific-heat measurements [100, 144] is plotted in Fig. 5.15(a). It is clearly visible, that $\lambda_{\text{spec. heat}}^{-2}(T) < \lambda_{\mu SR}^{-2}(T)$ for $T < T_c$. This underestimation of the magnetic penetration depth in the μSR experiments may result in a different temperature dependence of $\lambda^{-2}(T)$ and, therefore, in different gap sizes and weighting factors. Additionally, Johnston *et al.* considered the interband coupling of the superconducting bands and found an intermediate coupling strength [100]. The α model here used considers two non-interacting superconducting bands, which may also explain the different parameter values. However, taking into account the limitation of magnetic-penetration-depth measurements via μSR experiments and the used α model, the obtained parameter for $\Delta_1(0)$, $\Delta_2(0)$, $w(\Delta_1)$ and $\lambda(0)$ are in reasonable agreement with the values obtained by ARPES and specific-heat experiments.

The magnetic-penetration-depth anisotropy can be calculated under the assumption of $\lambda_a \approx \lambda_b$ by [136]

$$\gamma_\lambda = \frac{\lambda_c}{\lambda_{ab}}. \tag{5.22}$$

The temperature-independent value of $\gamma_\lambda = 1.5(4)$ is the smallest observed among the 122-pnictides [100], where values of 2 at T_c are obtained, which increase to 6 at 1 K [153], indicating a more three-dimensional behaviour in $Ca_{0.33}Na_{0.67}Fe_2As_2$. This result is consistent with the temperature-independent value of $\gamma = 1.85(5)$ for the anisotropy of the upper critical fields [154].

5.5. Summary and conclusion

In conclusion, [57]Fe-Mössbauer spectroscopy and muon spin relaxation experiments were performed to study the electronic phase diagram of $Ca_{1-x}Na_xFe_2As_2$ resulting in an updated phase diagram, which are shown in Figs. 5.16 and 5.17. The investigated samples have the Na-substitution levels $x = 0.00$, 0.35, 0.50, and 0.67. Upon Na substitution, the magnetic order is suppressed. For $x = 0.00$, a sharp magnetic transition is observed with a 4 K temperature difference between the onset of the magnetic order at 163 K and the fully ordered state at 167 K. This temperature difference increases to 21 K and 45 K while the onset temperatures are reduced to 161 K and 125 K for $x = 0.35$ and 0.50, respectively. The magnetic hyperfine field B_{hf} and the muon spin precession frequency, which are measures for the magnetic order parameter, are reduced as a function of x. This is shown in Fig. 5.16 together with the x-dependence of the angle between B_{hf} and the principal-axis of the EFG, θ. The decrease of θ as a function of x indicates a tilting of the the ordered magnetic moments out of the ab-plane. For $x = 0.35$, no reduction of the magnetic order parameter below the superconducting transition temperature is observed. In contrast, for $x = 0.50$, a reduction of the muon spin precession frequency of 7 % below T_c is observed. This originates in the competition of the superconducting and magnetic order parameter, as both states compete for the same electrons at the Fermi surface. In both $x = 0.35$ and 0.50, the coexistence of magnetic order and superconductivity is proven. For a deeper
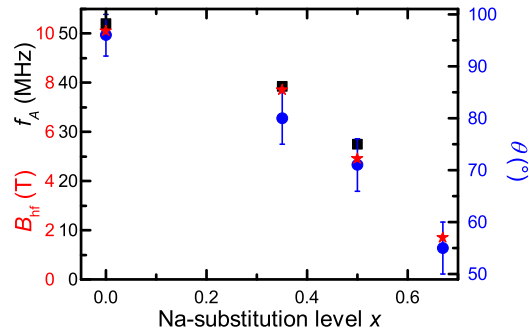
Figure 5.16.: Low-temperature saturation values of the magnetic hyperfine field B_{hf}, the muon spin precession frequency f_A, and θ, the angle between B_{hf} and the principal axis of the EFG, as a function of the Na-substitution level. Upon Na substitution, a reduction of the magnetic hyperfine field and the muon spin precession frequency is observed proving a reduction of the magnetic order parameter. The decrease of θ indicates a tilting of the magnetic moments out of the ab-plane as a function of the Na-substitution level.

understanding of the magnetic order parameter reduction in the coexistence region, Landau theory is applied finding a reduction of the magnetic order parameter as a function of T_c/T_N. The comparison of the Landau theory result with experimental data for various 122 compounds reveals a similar coupling strength of the magnetic and superconducting order parameter for $T_c/T_c < 0.7$. However, magnetic order is found in a much larger substitution level range compared to other iron-based superconductors.

For $x = 0.67$, diluted magnetic order is found. Therefore, the magnetism in $Ca_{1-x}Na_xFe_2As_2$ is persistent even at optimal doping. The superconducting state is investigated by measuring the temperature dependence of the London penetration depth, where two superconducting gaps with a weighting of nearly 50:50 are obtained. A temperature independent anisotropy of the magnetic penetration depth $\gamma_\lambda = 1.5(4)$ is obtained, which is much smaller compared to other 122 compounds indicating a more three dimensional behaviour of $Ca_{1-x}Na_xFe_2As_2$.

Magneto-structural properties of $Ca_{1-x}Na_xFe_2As_2$ are investigated using Mössbauer spectroscopy. In the paramagnetic state, a reduction of V_{zz} as a function of the Na-substitution level is observed from 12 V/Å^2 [117] to 9.1 V/Å^2 for $x = 0.00$ and 0.67, respectively. This is consistent with observations, that superconductivity emerges with highest T_c, when the FeAs$_4$ tetrahedron is least distorted [145]. The temperature dependence of V_{zz} shows an abrupt increase at T_N^{onset} indicating a magneto-structural phase transition. The analysis of the temperature dependence of the Debye-Waller factor reveals no change of the lattice dynamics at the magneto-structural phase transition. However, a reduction of the Debye temperature upon Na-substitution is observed indicating a softening of the lattice in the doped compounds compared to CaFe$_2$As$_2$. Furthermore, an increase of the electron density at the nucleus at the magneto-structural phase transition is observed.

The $Ca_{1-x}Na_xFe_2As_2$ substitution series is interesting and more stoichiometries are
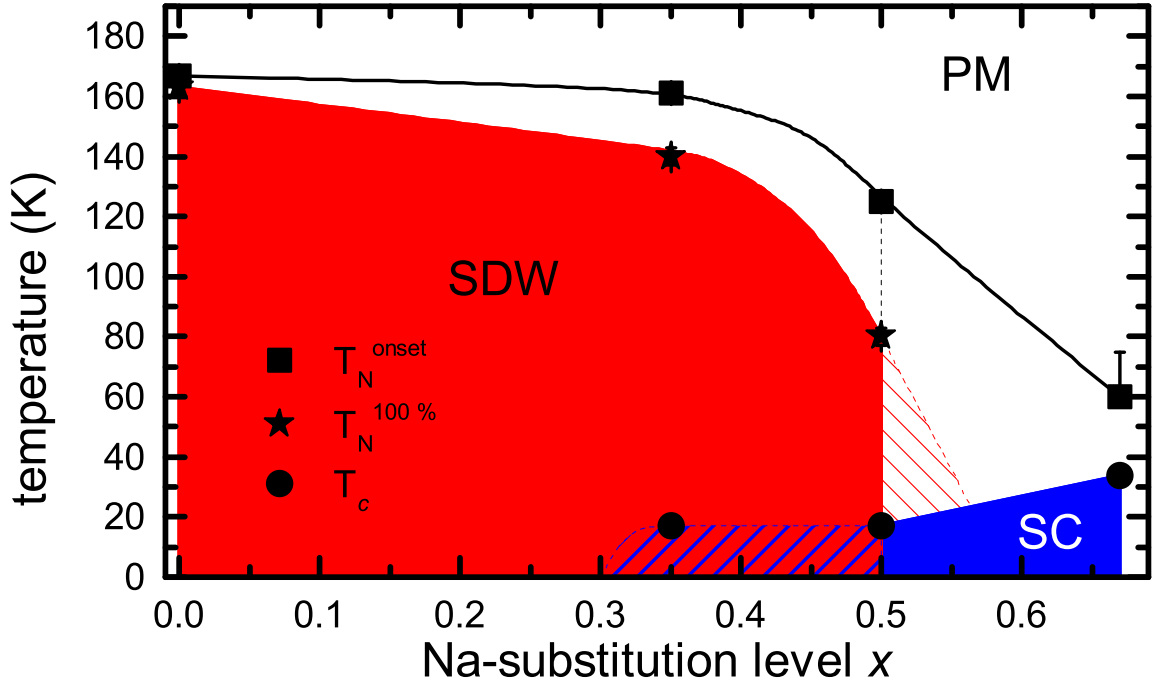
Figure 5.17.: Phase diagram of $Ca_{1-x}Na_xFe_2As_2$ obtained by μSR, Mössbauer spectroscopy, and magnetic susceptibility measurements. T_N^{onset} is the highest temperature with a finite magnetic volume fraction. $T_N^{100\%}$ is the highest temperature, where 100 % of the sample volume shows magnetic order. Mössbauer spectroscopy and μSR measurements result in equal values for T_N^{onset} and $T_N^{100\%}$ within error bars. T_c is the superconducting transition temperature. Above T_N^{onset}, a paramagnetic (PM) phase is observed. Below $T_N^{100\%}$, a antiferromagnetic spin density wave (SDW, red) is found. Below T_c, superconductivity (SC, blue) is found. The blue-red striped area marks the coexistence region of magnetic order and superconductivity with 100 % magnetic volume fraction. At optimal doping, diluted magnetism is found below T_N^{onset} coexisting with superconductivity.

needed to study the x-dependence of the frequency ratio f_A/f_B as well as the suppression of the magnetic order for $x > 0.00$. This would also answer the question, at which x the long-range magnetic order is changed to the diluted magnetism observed at optimal doping. Additionally, the determination of the low-temperature crystallographic structure of $Ca_{1-x}Na_xFe_2As_2$ for finite x is necessary to prove the assumption of a *Fmmm* phase.

5. *Mössbauer and muon spin relaxation spectroscopy of* $Ca_{1-x}Na_xFe_2As_2$

6. Mössbauer and muon spin relaxation spectroscopy of $Fe_{1+y}Te$

6.1. Properties of $Fe_{1+y}Te$

For a deeper understanding of the magnetic properties of $Fe_{1+y}Te$ observed by Mössbauer spectroscopy and μSR, it is useful to discuss thermodynamic and structural properties of the compounds.
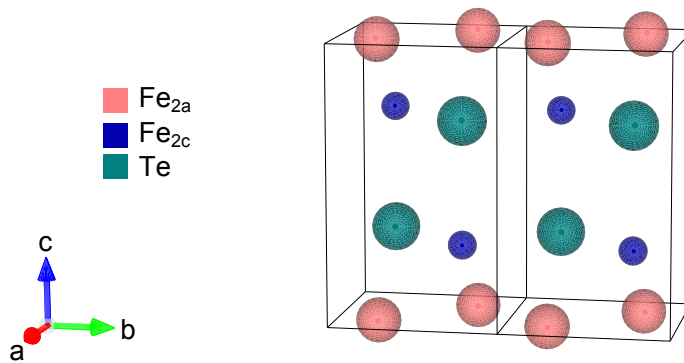
Figure 6.1.: Two unit cells of $Fe_{1+y}Te$ in the paramagnetic tetragonal structure, space group $P4/nmm$, are shown. Fe_{2a} denotes Fe occupying the crystallographic 2a site with an occupancy of 1. Fe_{2c} denotes Fe occupying the crystallographic 2c site with an occupancy proportional to the excess-iron level y. The picture is created using [94].

In the paramagnetic temperature regime, $Fe_{1+y}Te$ exhibits a tetragonal structure, which is shown in Fig. 6.1, with the space group $P4/nmm$ in a crystal structure intermediate between the PbO ($B10$) and Cu_2Sb ($C38$) types [155]. The iron atoms are located at the 2a and 2c sites. The former has the position $(0.75|0.25|0)$ and is fully occupied. The later has a variable position $(0.25|0.25|z)$ with $z \approx 0.72$ and is occupied with a probability of y, where y is the amount of excess-iron in $Fe_{1+y}Te$ [156, 157]. For a better discriminability of both iron sites, 2a and 2c are used as a subscript for the corresponding position. The Te atoms are located at the 2c site, which has the variable position $(0.25|0.25|z')$ with
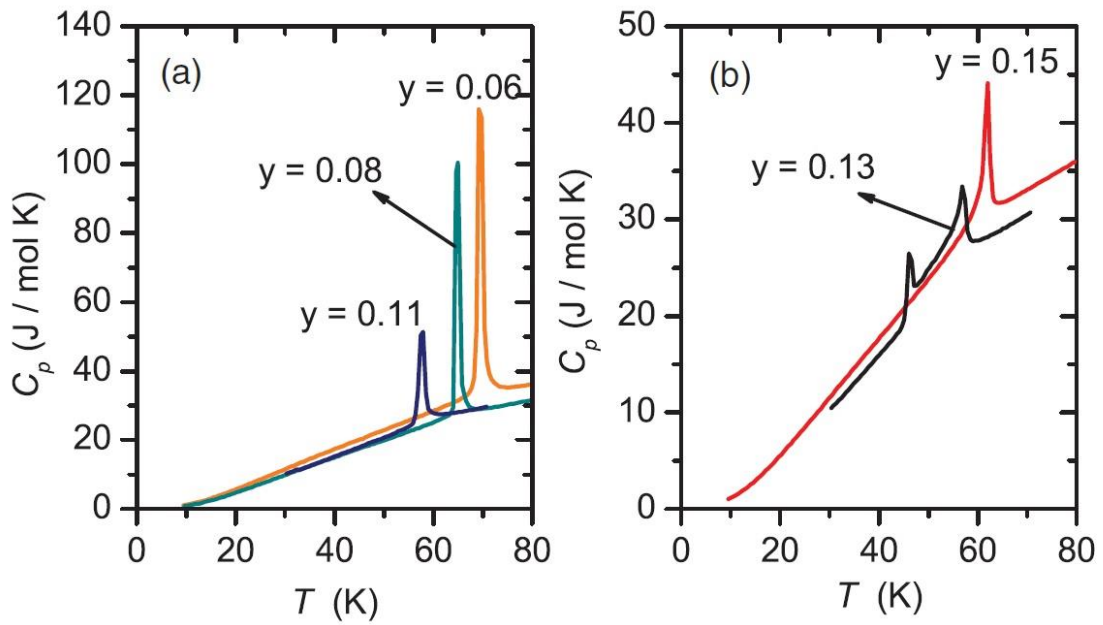
Figure 6.2.: Temperature dependence of the specific heat, $C_p(T)$, of $Fe_{1+y}Te$ for various excess-iron levels y. For $y = 0.06$, a sharp first-order phase transition is observed at 70 K. By increasing y, the transition temperature decreases to 57 K at $y = 0.11$. For $y = 0.13$, a λ-shaped peak at 57 K and a first-order peak at 46 K are observed. $Fe_{1.15}Te$ shows a λ-shaped peak at 63 K. Pictures taken from Ref. [155].

$z' \approx 0.28$ and is fully occupied [156, 157]. The lattice parameters a and c decrease with increased amount of excess-iron y [157].

In the magnetically ordered phase for $y \leq 0.11$, the crystallographic structure changes from tetragonal to monoclinic. This low-temperature phase has the space group $P2_1/m$ [155, 156]. For $y \geq 0.12$, the crystallographic structure in the magnetically ordered phase is orthorhombic with the space group $Pmmn$ [155, 156].

The temperature dependence of the specific heat $C_p(T)$ is shown in Fig. 6.2 for various excess-iron levels y. $Fe_{1.06}Te$ shows a sharp first-order like peak at 70 K, which is identified with the magneto-structural phase transition [155]. By increasing the amount of the excess-iron y, the transition temperature is suppressed to 57 K for $Fe_{1.11}Te$ [155]. The behaviour changes for $y \geq 0.12$, where two distinct phase transitions occur. For $Fe_{1.13}Te$, a λ-shaped peak at 57 K and a first-order peak at 46 K is observed. The peak at higher temperatures can be identified with the magnetic phase transition, while the peak at lower temperatures corresponds to the tetragonal-to-orthorhombic phase transition [155], which is uncommon among the iron pnictides and chalcogenides, where usually the structural phase transition occurs at the same or higher temperatures than the magnetic phase transition. $Fe_{1.15}Te$ shows a λ-shaped peak at 63 K, which is identified with the magnetic phase transition [155].

The temperature dependence upon cooling and heating of the magnetic-susceptibility, χ, measured in an applied field of 100 mT in field-cooled condition, is shown in Fig. 6.3(a) for various excess-iron levels [156]. By increasing y, the magnitude of χ increases due to the magnetic moment of the excess-iron supporting results from DFT calculations [158]. The temperature dependence of χ for $Fe_{1.11}Te$ shows a small thermal hysteresis. This indicates the first-order character of the phase transition. A broader thermal hysteresis was observed for $Fe_{1.12}Te$ and $Fe_{1.13}Te$. This indicates two consecutive phase transitions. For $y \geq 0.14$, no thermal hysteresis was observed, which is a sign for a continuous phase transition.

The temperature dependence of the normalized resistance R/R_{300K} for $y = 0.11$, 0.12, 0.13, 0.14, and 0.15 is shown in Fig. 6.3(a). For $y = 0.11$, 0.12, and 0.13, a metallic behaviour is observed below the phase transition. In contrast, the resistance of samples with $y = 0.14$ and 0.15 increases below the phase transition. This behaviour can be also seen in the temperature dependence of the resistivity, which is shown in Fig. 6.3(b). Resistivity values of the order of mΩ cm indicate semi-metallic behaviour [156]. For $y = 0.11$, a thermal hysteresis is observed. For $y = 0.12$ and 0.13, a broadened thermal hysteresis is observed and for $y = 0.14$ and 0.15 no thermal hysteresis is observed. Therefore, resistivity and magnetic-susceptibility measurements show similar behaviour in the excess-iron level dependence of the thermal hysteresis [156].

The first studies of the magnetic low-temperature phase were of theoretical nature. DFT calculations by Subedi *et al.* predict an electronic structure, which is similar to those of the iron pnictides [60]. This includes strong (π,0) Fermi surface nesting resulting in a large SDW gap. However, neutron-scattering experiments [157, 159] and ARPES measurements [160] reveal a different behaviour. The obtained magnetic and electronic structure is shown in Figs. 6.4(a) and 6.4(b). In contrast to the 122 compounds, which show a collinear antiferromagnetic order with a propagation vector (π, 0), neutron-scattering experiments evidenced a ($\delta\pi$,$\delta\pi$) bicollinear antiferromagnetic ordering, which is rotated

(a)

(b)
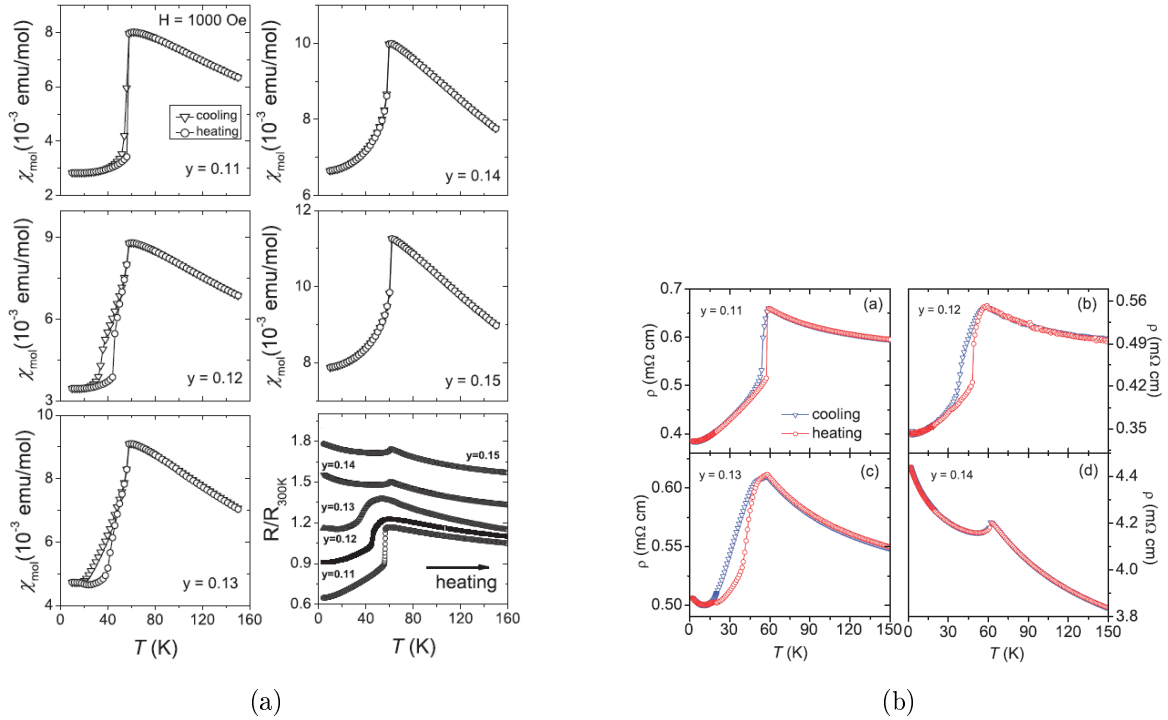
Figure 6.3.: (a) Temperature dependence of the magnetic-susceptibility χ for $y = 0.11$, 0.12, 0.13, 0.14, and 0.15 in an applied field of 100 mT. Above the magnetic transition temperature, paramagnetic behaviour is observed. For $y = 0.11$, a thermal hysteresis is observed indicating a first-order transition. For $y = 0.12$ and 0.13, a broadened thermal hysteresis is observed, indicating two consecutive phase transitions. For $y = 0.14$ and 0.15, no thermal hysteresis is observed indicating a continuous phase transition. The temperature dependence of the normalized resistance R/R_{300K} for $y = 0.11$, 0.12, 0.13, 0.14, and 0.15 upon heating is shown in the right column bottom graph. For $y = 0.11$, 0.12, and 0.13, a metallic behaviour is observed below the phase transition. In contrast, the resistance of samples with $y = 0.14$ and 0.15 increases below the phase transition. (b) Temperature dependence of the resistivity for $y = 0.11$, 0.12, 0.13, and 0.14. For $y \leq 0.13$, metallic behaviour is observed below the magnetic phase transition, while for $y = 0.14$ a semiconducting behaviour is observed. Pictures taken from Ref. [156].

by 45° compared to the 122 compounds. δ changes from a commensurate 0.5 for $y < 0.12$ to an incommensurate 0.38 for $y > 0.12$ [157, 159]. For $y < 0.12$, the magnetic moments point along the crystallographic b-axis. For $y > 0.12$, a spin component in direction of the crystallographic c-axis develops creating a helix structure [157].

The Fermi surface consists of circular hole pockets centered at Γ and elliptical electron pockets centered at M. Therefore, a nesting vector of $(\pi,0)$ between an electron and a hole pocket like in the 122 compounds is predicted by DFT calculations [60]. However, the experimentally identified antiferromagnetic propagation vector is $(\pi/2, \pi/2)$, where no nesting of an electron and an hole pocket is possible, since no electron pocket is found at $(\pi/2, \pi/2)$ by ARPES measurements [160]. Therefore, nesting as origin for the SDW order is unlikely, which makes Fe$_{1+y}$Te different from the other iron-based superconductors. Another interesting feature is the Curie-Weiss-like behaviour of the magnetic-susceptibility, which is uncommon in the iron-based superconductors, as they show an linear increasing normal-state susceptibility [103]. This supports the existence of localized magnetic moments rather than an itinerant behaviour of the system [160].

(a)   (b)
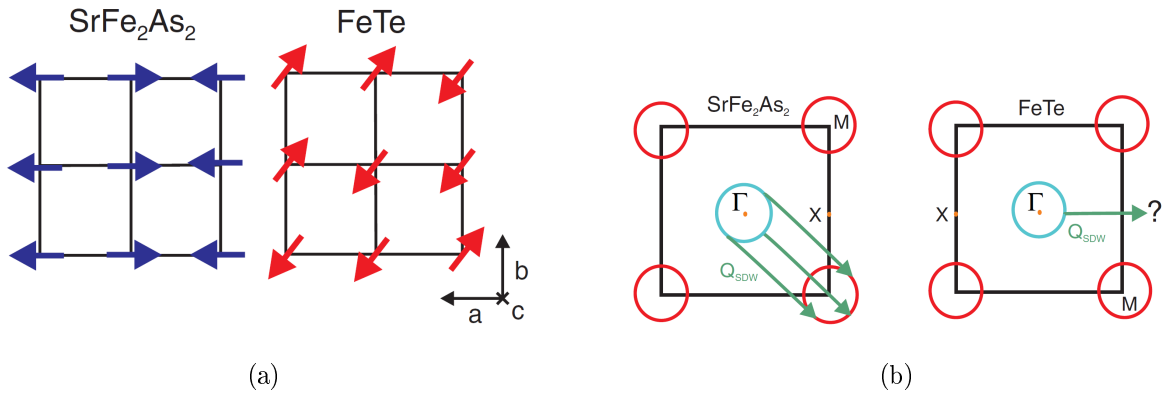
Figure 6.4.: (a) Magnetic structure of SrFe$_2$As$_2$ and FeTe. SrFe$_2$As$_2$ shows collinear antiferromagnetic ordering. The SDW has a propagation vector of $(\pi, 0)$. FeTe shows bicollinear antiferromagnetic ordering. The propagation vector is rotated by 45° and points along the $(\pi/2,\pi/2)$ direction. (b) Electronic structure of SrFe$_2$As$_2$ and FeTe. For SrFe$_2$As$_2$, electron and hole pockets can be nested by a vector $(\pi, 0)$, which is identical to the SDW propagation vector. For FeTe, a nesting between electron and hole pockets separated by $(\pi, 0)$ is in principle possible. A nesting along the SDW propagation vector $(\pi/2,\pi/2)$ is not possible, as no electron pocket is existing at $(\pi/2,\pi/2)$. Pictures taken from [160].

A summarizing phase diagram of the magnetic and structural phases is shown in Fig. 6.5.

To further investigate this splitting of the phase transitions in Fe$_{1.13}$Te as well as the magnetic ground state in all samples, muon spin relaxation and ^{57}Fe-Mössbauer spectroscopy experiments were performed.
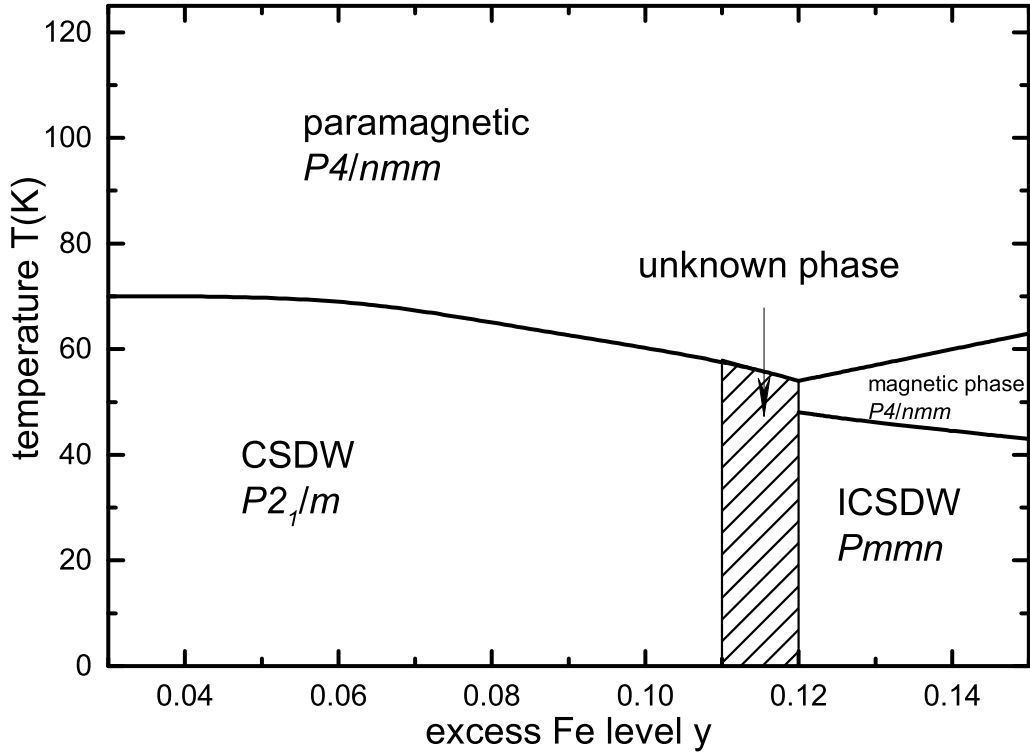
Figure 6.5.: Phase diagram of $Fe_{1+y}Te$ composed out of data from specific heat [155], magnetic-susceptibility [156], and x-ray diffraction [156] measurements as well as neutron-scattering experiments [157, 159]. The high-temperature phase consists of a paramagnetic phase with tetragonal structure. For $y < 0.11$, the low-temperature phase consists of a commensurate spin density wave (SDW) phase and a monoclinic structure. For $y > 0.12$, two phase transitions occur. The transition at higher temperatures is followed by a complicated magnetic phase and a tetragonal structure. The low-temperature phase shows an incommensurate SDW state and an orthorhombic structure.

6.2. Experimental details

Powder samples with the compositions $Fe_{1.06}Te$, $Fe_{1.12}Te$, $Fe_{1.13}Te$, and $Fe_{1.15}Te$ were successfully synthesised by Cevriye Koz at the Max-Planck-Institut für Chemische Physik fester Stoffe in Dresden. For details of the synthesis see Ref. [161].

μSR experiments were performed on samples of $Fe_{1.06}Te$, $Fe_{1.12}Te$, and $Fe_{1.13}Te$ with $\approx$ 150 mg sample mass for each composition. The experiments were performed at the πM3 beamline of the Swiss Muon Source at the Paul Scherrer Institut, Villigen, Switzerland, using the GPS spectrometer. The muon spin relaxation was measured in temperatures ranging from 5 up to 300 K in zero (ZF), longitudinal (LF) and transverse (TF) field geometry using external magnetic fields up to 400 mT. The μSR data were analysed using the MUSRFIT software [101].

I performed the Mössbauer spectroscopy (MBS) experiments for $Fe_{1.06}Te$, $Fe_{1.13}Te$, and $Fe_{1.15}Te$ at the Institut für Festkörperphysik, TU Dresden, in transmission geometry in a temperature range between 4.2 and 300 K using a CryoVac Konti IT cryostat. As a γ-source, ^{57}Co in rhodium matrix was used. The different compositions were prepared with $\approx$ 50 mg sample mass. To ensure a homogeneous distribution of the powder in the sample holder, ethanol was used. The data were analysed using the MOESSFIT software [32].

6.3. Results and discussion

6.3.1. Mössbauer spectroscopy results

Paramagnetic high-temperature phase

The room-temperature Mössbauer spectra for all compositions are shown in Fig 6.6(a). They show a slightly asymmetric doublet structure, which indicates the absence of magnetic order. The asymmetry of the doublet A is based on the angle φ between the incident γ-ray direction and the principal axis of the electric field gradient (EFG) and is described by

$$A(\varphi) = \frac{1 + \cos^2(\varphi)}{\frac{2}{3} + \sin^2(\varphi)}. \tag{6.1}$$

As the experiment was performed using powder samples, one would expect an asymmetry of $A = 1$ due to the averaging over all angles φ. In the analysing process, there are two possibilities to model an asymmetry of one: 1) Averaging over all angles φ or 2) setting the angle φ to a value of $\arccos(1/\sqrt{3}) \approx 54.7°$, which is called the magic angle. As it is shown in Fig 6.6(a), a small asymmetry is observed at room temperature. These deviation from $A = 1$ can be explained by a texture effect, which occurs, when the crystallites in the powder are not spherical but consist of small platelets. This platelets arrange in a not fully randomized orientation resulting in an effective angle φ_{eff} deviating from the magic angle corresponding to $A \neq 1$. The obtained angles are $\varphi_{\text{eff}} = 56(1)°$ and hence only differ by < 3 % from the magic angle supporting a small texture effect.

The Fe atoms are located at the 2a and 2c sites, which have the point symmetries

$\overline{4}m2$ and $4mm$. This ensures axial symmetry (asymmetry parameter $\eta = 0$) and a finite EFG at each iron site. The principal axis of EFG_{2a} and EFG_{2c} are directed along the crystallographic c-axis.
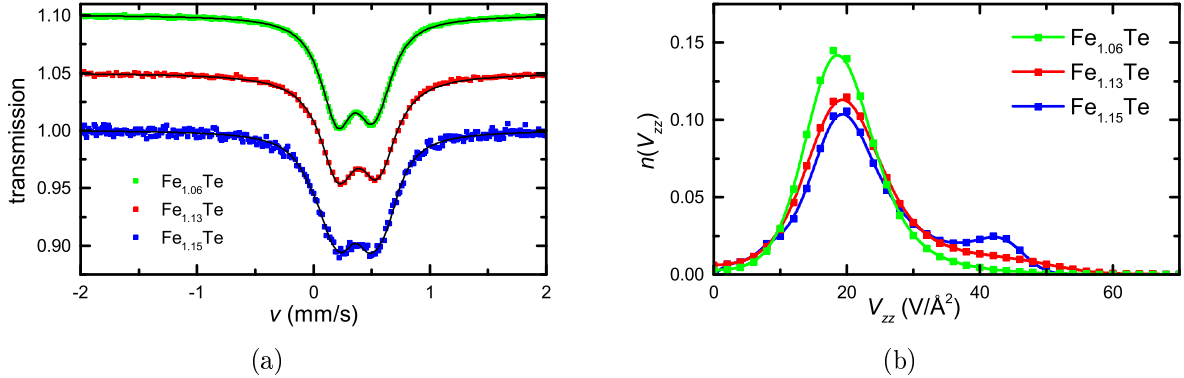
Figure 6.6.: (a) Mössbauer spectra of $Fe_{1.06}Te$, $Fe_{1.13}Te$, and $Fe_{1.15}Te$ at room temperature. The transmission of $Fe_{1.06}Te$ and $Fe_{1.13}Te$ is shifted by 0.10 and 0.05, respectively, for illustration purposes. (b) Distribution $n(V_{zz})$ extracted from the room temperature Mössbauer spectra.

The Mössbauer spectra at room temperature are analysed using a doublet pattern an isomer shift δ and the z-component of the EFG, V_{zz}. As there are two crystallographic inequivalent iron sites, where only the 2a site is fully occupied and the 2c site is partially occupied, at least two different EFGs are expected. Therefore, a distribution of V_{zz} values is assumed. The probability distribution $n(V_{zz})$ was obtained by using a maximum-entropy method, which is included in the MOESSFIT software [32]. The result is shown in Fig. 6.6(b) and shows two features at $V_{zz} = 20(1)$ V/$Å^2$ and $42(1)$ V/$Å^2$. The first is a peak with the majority of the spectral weight of the probability distribution. The second is a broad shoulder for $y = 0.06$ and 0.13, which turns into a well-defined peak for $y = 0.15$. By increasing the amount of excess-iron, spectral weight is shifted from the peak at 20 V/$Å^2$ to the feature at 42 V/$Å^2$. Analysing the spectral weight of the two features, one can extract the relative intensity of the two features at 20 V/$Å^2$(42 V/$Å^2$), which are 0.91 (0.09), 0.85 (0.15), and 0.80 (0.20) for $y = 0.06$, 0.13, and 0.15 respectively. To relate the two peaks to the two different iron sites, one has to take into account the properties of the 2a and 2c iron sites. The 2a site is fully occupied and the 2c site is occupied with a probability given by the amount of excess-iron y. Therefore, the total amount of iron in the system is $1+y$ with $\frac{y}{1+y}$ and $\frac{1}{1+y}$ being the relative amount of iron on the 2a and 2c sites. Applying this to the investigated samples, relative amounts of 0.94 (0.06), 0.88 (0.12), and 0.87 (0.13) for $y = 0.06$, 0.13, and 0.15, respectively, for the iron 2a (2c) site would be expected. Comparing this relative amounts of iron with the relative intensities of the two features in $n(V_{zz})$ gives reasonable agreements for $y = 0.06$ and 0.13. For $y = 0.15$, the agreement is moderate, which can be explained by the higher degree of disorder due to the large amount of excess-iron in the system. In addition, the 2a site is directly located on the tetragonal lattice, while the 2c site is located between the FeTe tetrahedrons. Therefore, one would expect a higher EFG for the 2c than for the 2a site. Due to this reasons, the

peak at 20 V/Å² is identified with iron occupying the 2a site and the peak at 42 V/Å² with the 2c site and hence the system contains two inequivalent iron sites.

For further analysis in the paramagnetic temperature regime, two doublet patterns are used to investigate the measured Mössbauer spectra. A set of hyperfine parameters δ and V_{zz} is assigned to each doublet pattern corresponding to the two iron sites 2a and 2c with the same relative intensities as obtained by the analysis of $n(V_{zz})$. At room-temperature, the obtained values of $V_{zz,2a}$ are 17.2(6) V/Å², 18.4(1) V/Å², and 17.2(6) V/Å², while the second pattern has values of $V_{zz,2c}$ = 32(1) V/Å², 38(1) V/Å², and 36(2) V/Å² for $y = 0.06, 0.13$, and 0.15, respectively. This values are in good agreement with the more general approach of the distribution $n(V_{zz})$. With decreasing temperature, $V_{zz,2a}$ increases slightly to values of 19.6(3) V/Å², 21.0(3) V/Å², and 20.5(5) V/Å², while $V_{zz,2c}$ increases to 40(1) V/Å², 39.3(9) V/Å², and 40(1) V/Å² for $y = 0.06, 0.13$, and 0.15 at $T \approx 80$ K, respectively. V_{zz} was fixed for temperatures below 80 K to reduce the number of free parameters in the magnetically ordered phase.

The temperature dependence of the center shift δ is shown in Figs. 6.7(a), 6.7(b), and 6.7(c). Both center shifts δ_{2a} and δ_{2c} are of equal value within error bars in the paramagnetic temperature regime. Values of 0.472(5) mm/s, 0.482(5) mm/s, and 0.479(5) mm/s are obtained at room temperature for $y = 0.06, 0.13$, and 0.15, which increase to 0.60(2) mm/s, 0.614(5) mm/s, and 0.62(2) mm/s at ≈ 80 K, respectively. For $y = 0.06$, δ_{2a} and δ_{2c} are of equal value in the magnetically ordered state. With decreasing temperature, the isomer shift increases to a value of $\delta_{2a,2c} = 0.63(1)$ mm/s at 4.2 K.

For $y = 0.13$ and 0.15 a splitting below 80 K is visible. With $\delta_{2a} = 0.69(3)$ mm/s and $\delta_{2a} = 0.67(3)$ mm/s the a site center shifts are smaller than $\delta_{2c} = 0.79(2)$ mm/s and $\delta_{2c} = 0.74(3)$ mm/s at 4.2 K, respectively. Therefore, the s-electron density at the nucleus is higher for the 2a site than for the 2c site. However, the electron density of the 1s-, 2s-, and 3s-electrons is nearly constant [24]. In contrast, the 3d-electrons can screen the 4s-electrons. A more itinerant behaviour of the 3d-electrons results in a reduced screening of the 4s-electrons and, therefore, an increased electron density at the nucleus. I.e., the 2a site shows a more itinerant behaviour than the 2c site, which supports results from DFT calculations [158].

Magnetic low-temperature phase

The onset temperature of the magnetic ordering, $T_{\mathrm{N}}^{\mathrm{onset}}$, is defined as the temperature, at which the Mössbauer linewidth, w, shows an abrupt increase due to the appearance of a magnetic hyperfine field. The Mössbauer spectra in the magnetically ordered temperature regime are analysed using two subspectra. Each subspectrum contains a set of hyperfine parameters: δ, V_{zz}, w and the magnetic hyperfine field B_{hf}. The centers shifts are δ_{2a} and δ_{2c} and their temperature dependence is shown in Figs. 6.7(a), 6.7(b), and 6.7(c). V_{zz} was fixed in the magnetically ordered state to its value at ≈ 80 K. First, the magnetic hyperfine fields at the 2a and 2c sites are analysed using a maximum-entropy method. The result of this first and most general analysis is, that the magnetic hyperfine field at the 2c site shows a Gaussian distribution. Taking into account the small relative intensity of the 2c pattern and to reduce the amount of parameters, it is convenient to analyse B_{hf} at the 2c

(a)

(b)

(c)
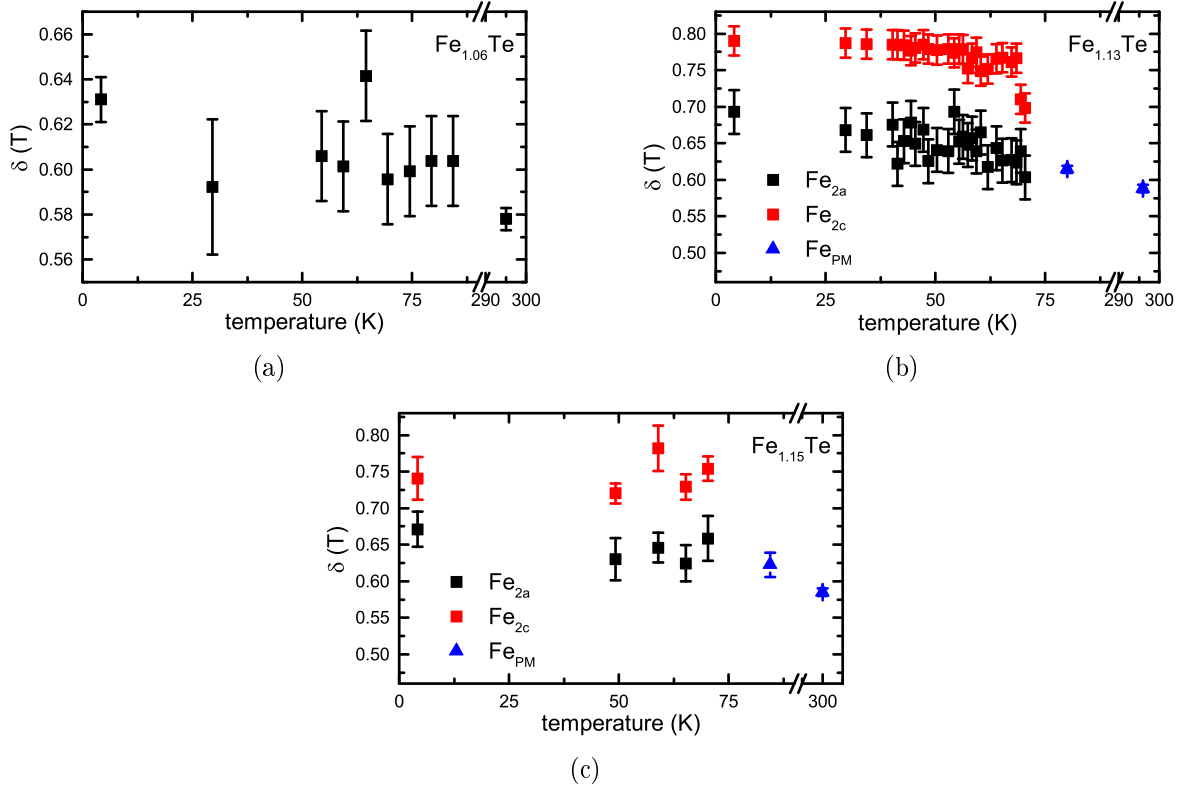
Figure 6.7.: Temperature dependence of the center shift $\delta(T)$ of (a) $Fe_{1.06}Te$, (b) $Fe_{1.13}Te$, and (c) $Fe_{1.15}Te$. For $Fe_{1.06}Te$, both δ_{2a} and δ_{2c} are of equal value over the whole temperature range. For $Fe_{1.13}Te$ and $Fe_{1.15}Te$, both δ_{2a} and δ_{2c} are of equal value and denoted as Fe_{PM} in the paramagnetic temperature regime. In the magnetically ordered state, δ_{2a} and δ_{2c} have different values.

site with a magnetic hyperfine field, which is Gauss-distributed:

$$n(B_{\mathrm{hf}}) \;=\; \frac{1}{\sqrt{2\pi}\sigma}\exp\left(-\frac{1}{2}\frac{[B-B_{2\mathrm{c}}]^2}{\sigma^2}\right), \qquad (6.2)$$

with the first moment $B_{2\mathrm{c}}$ and the standard deviation σ. The magnetic field distribution at site 2a was determined by maximum entropy at all temperatures. The resulting distributions at 4.2 K are shown in Figs. 6.8(a), 6.8(b), and 6.8(c).

(a)

(b)

(c)
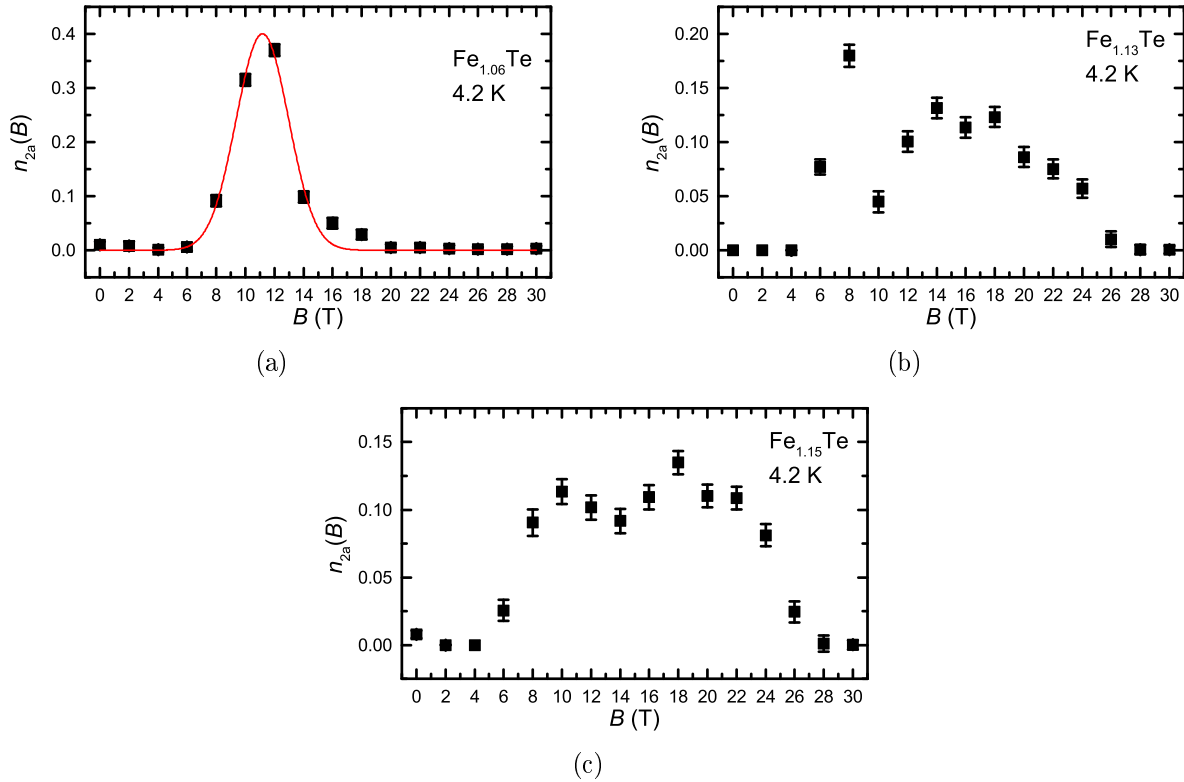
Figure 6.8.: Magnetic field distribution $n_{2\mathrm{a}}(B)$ of $Fe_{1+y}Te$ with $y = 0.06$, 0.13, and 0.15 at 4.2 K. The red line in (a) shows the Gaussian magnetic field distribution of the excess-iron for $y = 0.06$ (scaled for comparison purposes).

Magnetic order in $Fe_{1.06}Te$

The Mössbauer spectrum at 4.2 K is shown in Fig. 6.9, where a well-resolved sextet structure is visible, which is a sign for a well-defined B_{hf}-value. The temperature dependence of the magnetic volume fraction is shown in Fig. 6.10(b) together with results from TF-μSR measurements, which are discussed in Sec. 6.3.2. Below 72 K, static magnetic order is observed by Mössbauer spectroscopy, while μSR detects magnetic order up to $\approx$ 100 K. At 65 K, the magnetic volume fraction approaches 100 %. The 5 % non-magnetic sample fraction measured by μSR is attributed to muons stopping outside the sample (e.g. the
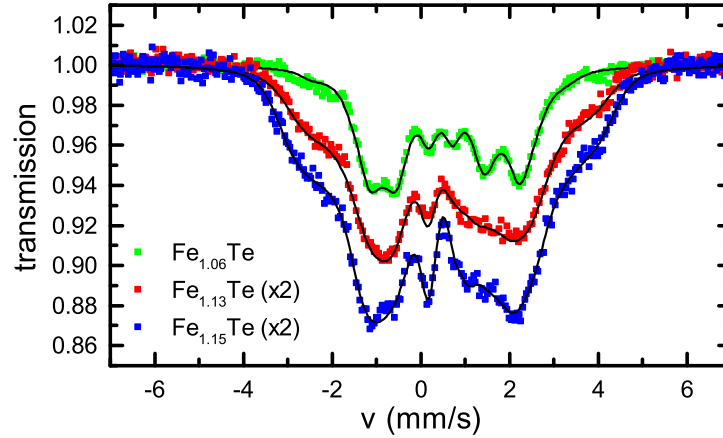
Figure 6.9.: Mössbauer spectra at 4.2 K of $Fe_{1+y}Te$ with $y = 0.06, 0.13$, and 0.15 including best fits. The absorption for $y = 0.13$ and 0.15 is doubled for illustration purposes.

cryostat). The magnetic hyperfine field at both Fe sites are of equal value within error bars within the investigated temperature range, as it is shown in Fig 6.10(a). The magnetic field distribution at the 2a site at 4.2 K shows a peak at ≈ 11 T. In Fig. 6.8(a), the magnetic field distribution at the 2a site and the Gaussian field distribution at the 2c site (scaled for comparison purposes) is plotted and both are virtually congruent. Therefore, I conclude, that both Fe sites show the same magnetic properties within the resolution of the Mössbauer spectroscopy. The Gaussian behaviour of both magnetic hyperfine fields instead of a Lorentzian is attributed to the disorder introduced by the excess-iron compared to a theoretical FeTe compound.
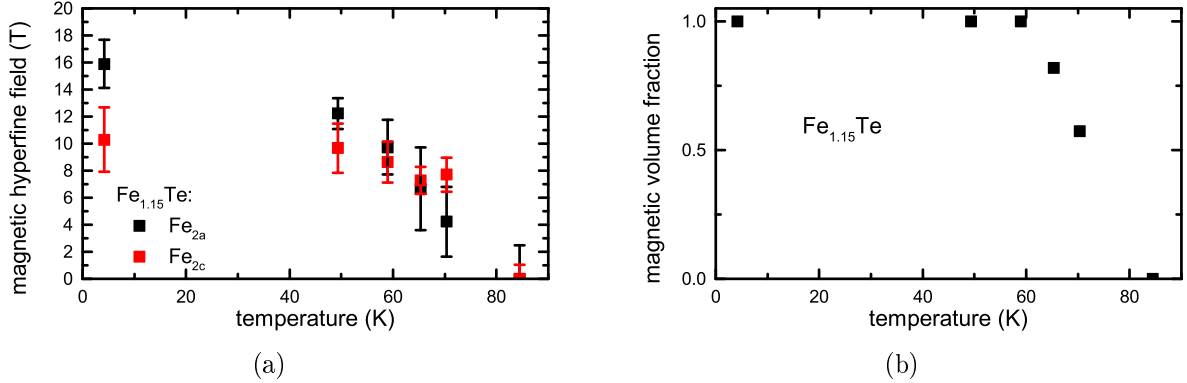

(a)

(b)
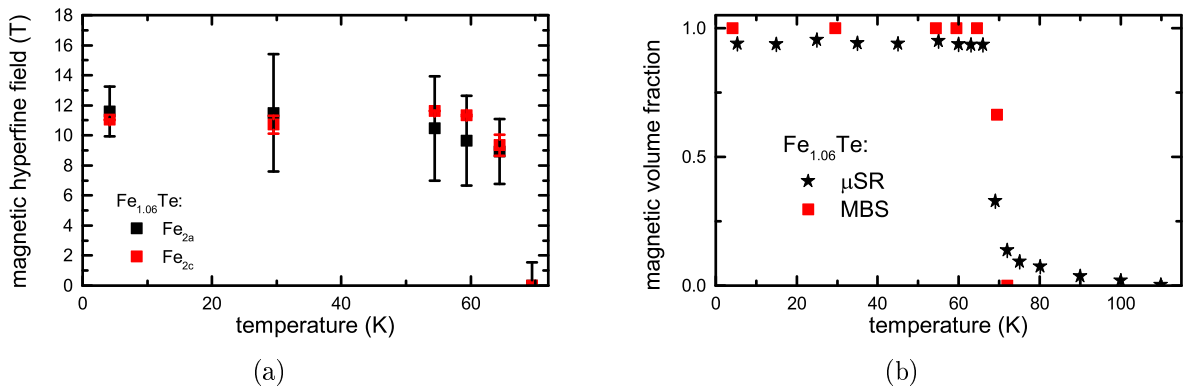
Figure 6.10.: (a) Temperature dependence of the average magnetic hyperfine field of the magnetic field distribution at the 2a site as well as the temperature dependence of the first moment of the Gaussian magnetic field distribution at the 2c site for $Fe_{1.06}Te$. (b) Temperature dependence of the magnetic volume fraction determined by Mössbauer spectroscopy and TF-μSR.

Magnetic order in Fe$_{1.13}$Te and Fe$_{1.15}$Te

The Mössbauer spectra of Fe$_{1.13}$Te and Fe$_{1.15}$Te at 4.2 K are shown in Fig. 6.9. They show a less-clear resolved sextet structure compared to Fe$_{1.06}$Te. This can be explained by either a magnetic field distribution or magnetically inequivalent Fe sites or both. The magnetic field distributions of the 2a site at 4.2 K are shown in Figs. 6.8(b) and 6.8(c). They show a rectangular shape consistent with the result in Ref. [162]. Blachowski *et al.* expanded the magnetic field distribution in terms of Fourier coefficients, which requires a periodic and piecewise continuous distribution. This may be a too strong constriction of the possible shape of the magnetic field distribution. Maximum entropy determines the most probable distribution without any restrictions of the shape of the distribution. Furthermore, the rectangular shape is comparable with a broadened incommensurate spin-density wave shape suggested by neutron-scattering experiments [157]. The temperature dependence of

(a)   (b)
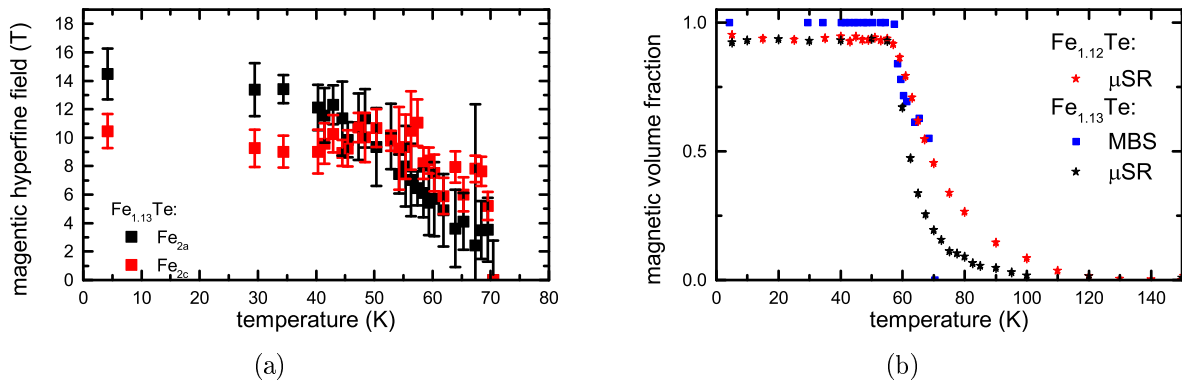
Figure 6.11.: (a) Temperature dependence of the average magnetic hyperfine field of the magnetic field distribution at the 2a site as well as the temperature dependence of the first moment of the Gaussian magnetic field distribution at the 2c site of $y = 0.13$. (b) Temperature dependence of the magnetic volume fraction determined by Mössbauer spectroscopy and TF-μSR for Fe$_{1+y}$Te with $y = 0.12$ and 0.13.

the average value of the magnetic field distribution at the 2a site as well as the first moment of the Gauss-distributed magnetic hyperfine field at the 2c site is shown in Figs. 6.11(a) and 6.12(a). At temperatures slightly below the magnetic transition temperature, both $B_{\mathrm{hf,\ 2a}}$ and $B_{\mathrm{hf,\ 2c}}$ are of equal value within error bars. For Fe$_{1.13}$Te, a splitting occurs below the structural phase transition at 46 K supporting the strong magneto-elastic coupling scenario in this compounds [155, 156, 163]. For Fe$_{1.15}$Te, a splitting is obtained down to lowest temperatures, but the onset of the splitting cannot be determined due to the lack of data points between 4.2 K and 50 K. It should be expected at 45 K, where Rössler *et al.* report the structural transition temperature [155].

The temperature dependence of the magnetic volume fraction is shown in Fig. 6.11(b) together with results from TF-μSR-measurements, which are discussed in Sec. 6.3.2. Mössbauer spectroscopy measurements show magnetic order below 70 K and 85 K and 100 % magnetic volume fraction below 60 K for $y = 0.13$ and 0.15, respectively. TF-μSR-

experiments on $Fe_{1.12}Te$ and $Fe_{1.13}Te$ show the onset of magnetic order below 100 K and they are fully magnetically ordered below 55 K. The 5 % non-magnetic sample fraction measured by μSR is attributed to muons stopping outside the sample (e.g. the cryostat).

Figure 6.12.: a) Temperature dependence of the average magnetic hyperfine field of the magnetic field distribution at the 2a site as well as the temperature dependence of the first moment of the Gaussian magnetic field distribution at the 2c site of $y = 0.15$. b) Temperature dependence of the magnetic volume fraction determined by Mössbauer spectroscopy for $y = 0.15$.

6.3.2. Muon spin relaxation results

Muon stopping sites were calculated via the minimum of the sign-reversed electrostatic potential, which was obtained from a self-consistent DFT calculation, by Lamura *et al.* for the case of stoichiometric FeTe [164]. The obtained stopping sites are $(0.25|0.25|0.27)$ and $(0.75|0.25|0.50)$. However, the former stopping site is stable, while the latter site is unstable against the zero-point motion of the muon. Therefore, muons stopping at the latter site will immigrate to either $(0.25|0.25|0.27)$ or the Fe 2c site $(0.25|0.25|z)$, which is only partially occupied [164].

ZF-μSR spectra for $y = 0.06$, 0.12, and 0.13 are shown in Figs. 6.13(a), 6.13(b), and 6.13(c), respectively, for representative temperatures in the paramagnetic and magnetically ordered state. At 290 K, the time evolution of the muon spin polarization, $P(t)$, shows an exponential relaxation with a damping rate $\lambda = 0.040(1)$ MHz and 0.068(1) MHz for $y = 0.06$ and 0.12, respectively. This exponential damping is a sign of dynamic electronic fluctuations. For $Fe_{1.13}Te$, measurements in LF geometry, which are discussed in detail below, indicate a dynamical origin of the exponential damping of $P(t)$. DFT+DMFT calculations indicate fluctuating paramagnetic moments in FeTe [165]. X-ray emission spectroscopy measurements reveal a paramagnetic fluctuating moment, which is constant within error bars for $Fe_{1.03}Te$ and $Fe_{1.12}Te$ [166]. The independence of the fluctuating paramagnetic moment from the excess-iron level indicates, that the exponential relaxation at room temperature in all investigated samples is caused by fluctuating fields. This paramagnetic contribution is given by the Fe^{2+} ions [167]. This valence state is in agreement with the former presented results for the isomer shifts [24].

(a)

(b)

(c)
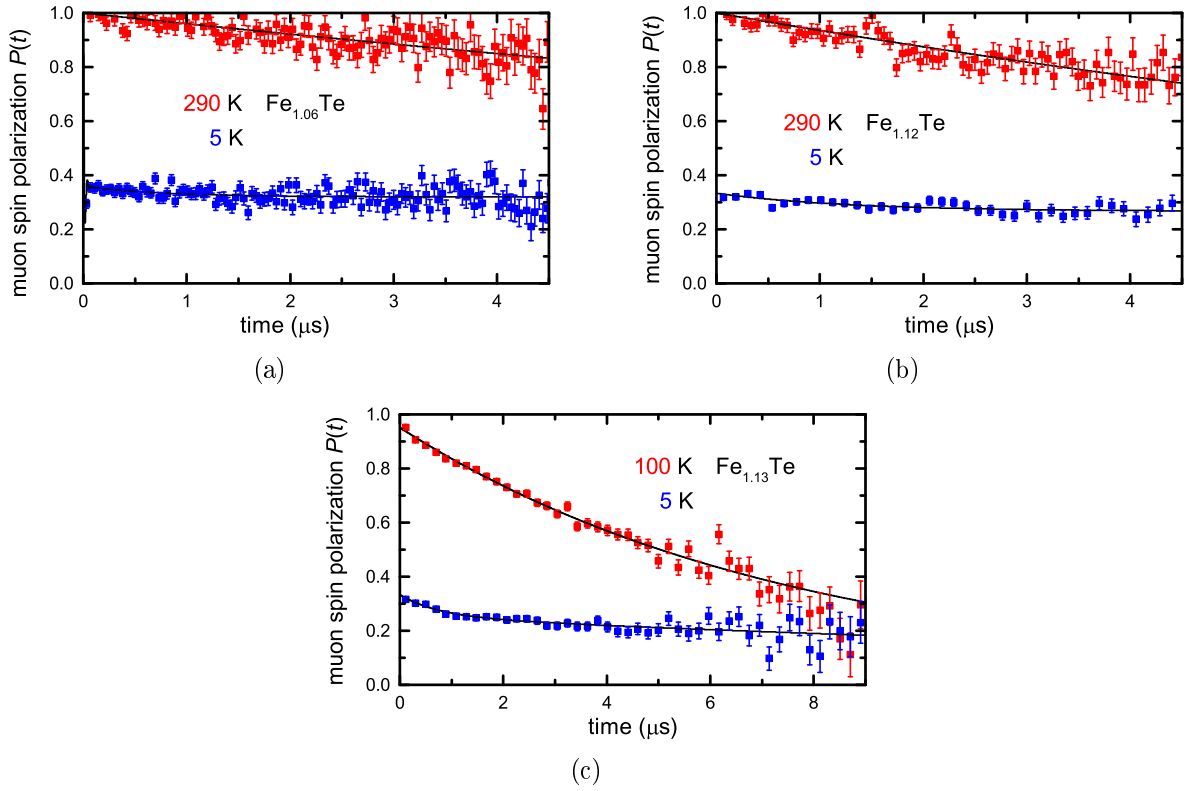
Figure 6.13.: Time evolution of the muon spin polarization $P(t)$ at temperatures above and below the magnetic transition temperatures of 65 K for (a) $Fe_{1.06}Te$, 55 K for (b) $Fe_{1.12}Te$, and (c) $Fe_{1.13}Te$, respectively. Solid lines are best fits using Eq. (6.3).

Magnetic order in Fe$_{1+y}$Te

μSR measurements in TF geometry in an applied field of 5 mT were performed at temperatures between 5 K and 300 K for Fe$_{1.06}$Te, Fe$_{1.12}$Te, and Fe$_{1.13}$Te. The resulting temperature dependence of the magnetic volume fraction is shown in Figs. 6.10(b) and 6.11(b). A nonzero magnetic volume fraction is obtained for temperatures below 100-110 K. By reducing the temperature, the magnetic volume fraction increases until it reaches nearly 100 % at 65 K for Fe$_{1.06}$Te, at 55 K for Fe$_{1.12}$Te and at 60 K for Fe$_{1.13}$Te. The small amount of non-magnetic volume fraction arises from muons stopping inside the sample holder.

ZF measurements in the magnetic phase below $\approx$ 100 K show two signal fractions corresponding to two magnetically inequivalent muon stopping sites. The time evolution of the muon spin polarization is analysed using the function

$$P(t) = V_{\mathrm{mag}} A_{\mathrm{osc}} \left[\frac{2}{3} G_{\mathrm{osc}}(f_\mu, t) \mathrm{e}^{-\lambda_{\mathrm{T,osc}} t} + \frac{1}{3} \mathrm{e}^{-\lambda_{\mathrm{L,osc}} t} \right]$$
$$+ V_{\mathrm{mag}} A_{\mathrm{nonosc}} \left[\frac{2}{3} \mathrm{e}^{-\lambda_{\mathrm{T,nonosc}} t} + \frac{1}{3} \mathrm{e}^{-\lambda_{\mathrm{L,nonosc}} t} \right]$$
$$+ \left[1 - V_{\mathrm{mag}} \right] \mathrm{e}^{-\lambda_{\mathrm{PM}} t}, \tag{6.3}$$

similar to Eq. (2.37) with the magnetic volume fraction V_{mag}, the transversal relaxation rates λ_{T} and the longitudinal relaxation rates λ_{L}. $G_{\mathrm{osc}}(f_\mu, t)$ denotes an oscillation function as a function of time t and the muon spin precession frequency f_μ. The paramagnetic signal fraction is modelled using a simple exponential relaxation function with a temperature independent relaxation rate λ_{PM}. The two magnetically inequivalent muon stopping sites are occupied with probabilities of A_{osc} and A_{nonosc} under the condition $A_{\mathrm{osc}} + A_{\mathrm{nonosc}} = 1$. The occupation probability A_{osc} has temperature-independent values of 0.96, 0.80, and 0.76 for Fe$_{1.06}$Te, Fe$_{1.12}$Te, and Fe$_{1.13}$Te, respectively. However, the 2/3-part (see Sec. 2.6.3 for more details about the origin of the 2/3 signal fraction) of both magnetic signals, A_{osc} and A_{nonosc}, are fully damped within the first 20 ns of $P(t)$. This strong damping indicates a higher degree of disorder in the system due to the excess-iron resulting in transversal relaxation rates of the order of a few hundred MHz. This high damping caused experimental difficulties, as the the time resolution of the spectrometer was of the order of 1 ns. Therefore, high statistic measurements were needed resulting in long measurement times. As the beamtime at the PSI was highly limited for Fe$_{1.06}$Te and Fe$_{1.12}$Te, only the most important temperatures were investigated by means of ZF-μSR. For Fe$_{1.13}$Te, more beam time was available resulting in more ZF data points. To analyse the form of the relaxation in this first 20 ns of $P(t)$, different relaxation functions with and without an oscillation are used and the coefficients of determination of the resultant fits are compared. These coefficients are a measure for the quality of the analysis as a function of the sample size and the number of parameters. The most probable result is the following. The oscillation function $G_{\mathrm{osc}}(f_\mu, t)$ is a cosine for Fe$_{1.06}$Te, which is identified with long-range commensurate magnetic order. The oscillation frequency at 5 K is obtained as f_μ= 168(10) MHz, which corresponds to a field of B = 197(12) mT at the muon stopping site. This is in good agreement with measurements at Fe$_{1.03}$Te and Fe$_{1.087}$Te, where values of 210 mT [168] and 197(11) mT [164] are reported. For Fe$_{1.12}$Te and Fe$_{1.13}$Te, $G_{\mathrm{osc}}(f_\mu, t)$ is best described by

a *0*th-order Bessel function, which is identified with long-range incommensurate magnetic order. The oscillation frequency at 5 K is obtained as $f_\mu = 73(6)$ MHz, which corresponds to a field of $B = 86(7)$ mT at the muon stopping site. Muons, stopping at the site described by A_{nonosc}, show no coherent oscillation of the muon spins. This is consistent with a very broad internal magnetic field distribution at this muon stopping site preventing a coherent oscillation of the muon spins.

As a consequence of this strong static damping, after 20 ns only the 1/3-tail parts of the signal are observed. The ZF spectra at 5 K, which are shown in Figs. 6.13(a), 6.13(b) and 6.13(c), show an exponential relaxation of the 1/3-tail, which is caused by magnetic field fluctuations. Above 70 K, where TF-μSR measurements show a magnetic volume fraction below 15 %, both λ_{L}s are of the same order of magnitude as the relaxation rate of the paramagnetic volume fraction, λ_{PM}. Both λ_{L} increase between 60 K and 70 K due to enhanced low-frequency magnetic fluctuations above the magnetic transition temperature. In the fully ordered state, both λ_{L}s decreases, which indicates a slowing down of the field fluctuations and a more static internal field distribution.

Taking into account the two different muon sites proposed by DFT calculations [164], the two signal fractions can be interpreted in the following way: The A_{osc}-signal fraction is identified with muons stopping at a stable site (0.25|0.25|0.27) where they experience long-range magnetic order. The A_{nonosc}-signal fraction is identified with muons stopping at a metastable site (0.75|0.25|0.50), which successfully move to a stable site. This movement results in a broad internal field distribution experienced by the muon, which prevents a coherent oscillation of the muon spin. This results in an exponential relaxation of the muon spin polarization. The reduction of the A_{osc}-signal fraction as a function of the excess-iron level is attributed to the higher degree of disorder in the system, which results in a broader field distribution.
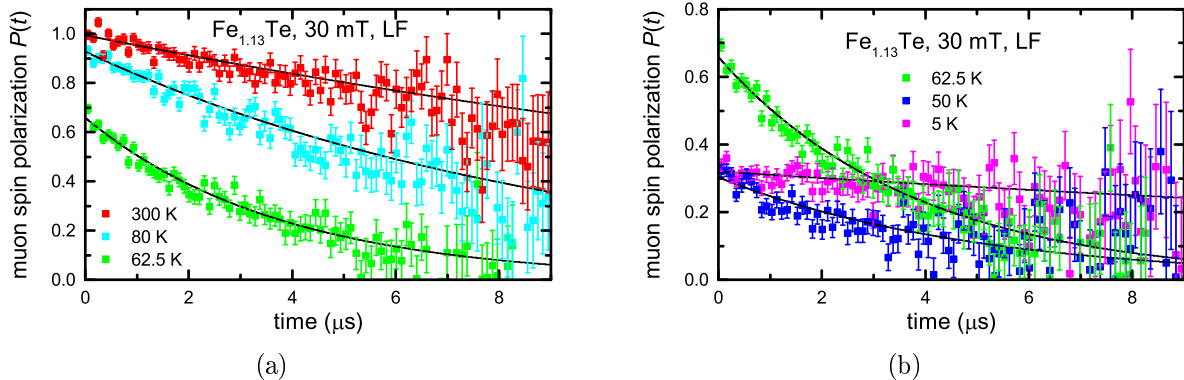
Figure 6.14.: Temperature dependence of the time evolution of the muon spin polarization of Fe$_{1.13}$Te in an applied longitudinal field (LF) of 30 mT. Solid lines are best fits to Eq. (6.4).

To further investigate the dynamics in Fe$_{1.13}$Te, μSR experiments in LF geometry in fields up to 400 mT at various temperatures between 5 K and 300 K were performed. The time evolution of the muon spin polarization in an applied LF of 30 mT is shown in Figs. 6.14(a) and 6.14(b) for various temperatures in the paramagnetic and magnetically

ordered state. $P(t)$ was analysed using the function

$$P(t) = V_{\mathrm{mag}} \left\{ A_{\mathrm{T}} \cos(\gamma_\mu B_{\mathrm{loc}} t)\, \mathrm{e}^{-\lambda_{\mathrm{T}}} + [1 - A_{\mathrm{T}}]\, \mathrm{e}^{-\lambda_{\mathrm{LF}}} \right\} + [1 - V_{\mathrm{mag}}]\, \mathrm{e}^{-\lambda_{\mathrm{PM}}}, \qquad (6.4)$$

with the magnetic volume fraction V_{mag}, the transversal fraction A_{T}, the longitudinal relaxation rate λ_{LF}, the transversal relaxation rate λ_{T} and the paramagnetic relaxation rate λ_{PM}. B_{loc} describes the local internal magnetic field at the muon site. The transversal relaxing A_{T} component of the magnetic volume fraction is depolarized within the first 20 ns in the magnetically ordered state similar to the ZF measurements. λ_{PM} and λ_{LF} are usually of the same order of magnitude and difficult to distinguish. Practically, λ_{PM} is set to be constant for the analysis process in the transition area region with $V_{\mathrm{mag}} \in (0;1)$. The resultant temperature dependence of λ_{LF} is shown in Fig. 6.3.2. λ_{LF} remains constant within error bars between 100 K and 300 K. The exponential relaxation in this temperature regime can be caused by two effects. Either due to the dipole-dipole interaction of the muon spin with diluted nuclear magnetic moments or due to fluctuating fields at the muon site. However, typical values of the relaxation rate due to the interaction of the muon spin with nuclear magnetic moments are of the order of $\sigma_{\mathrm{nm}} \leq 0.1$ MHz corresponding to a field $\sigma_{\mathrm{nm}}/\gamma_\mu \leq 2.8$ mT. Therefore, an applied field of 30 mT would sufficiently decouple the muon spin from the static internal magnetic field distribution resulting in an undamped muon spin polarization. Therefore, the exponential relaxation in the paramagnetic temperature regime above 100 K is caused by fluctuating moments. Below 100 K, magnetic order develops resulting in a non-zero V_{mag}, whose temperature dependence is equal to the temperature dependence obtained by TF-measurements, which is shown in Fig. 6.11(b). Below 100 K, λ_{LF} increases up to a maximum at 60 K. Below 55-60 K, λ_{LF} decreases down to lowest temperatures. This behaviour is identified with an increase of the magnetic fluctuations above the magnetic transition temperature of $T_{\mathrm{N}} = 55$ K and a slowing down of the dynamics within the fully ordered state. This slowing down can be seen in Fig. 6.14(b) by comparing $P(t)$ for 5 K and 50 K. The exponential depolarization of the 1/3-tail is higher for 50 K than for 5 K proving the slowing down of the magnetic fluctuations to lowest temperatures.
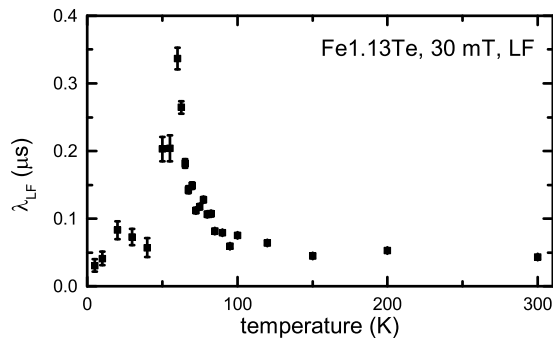
Figure 6.15.: Temperature dependence of the longitudinal relaxation rate λ_{LF}, which is contained using Eq. (6.4).

Decoupling experiments were performed in longitudinal fields up to 400 mT at 50 K, 70 K, and 100 K. The corresponding time evolution of the muon spin polarization is shown

in Figs. 6.16(a), 6.16(b), and 6.16(c), respectively. The ZF-spectrum at 100 K shows a fast depolarization from $P(t = 0) = 1.00$ to $P(t = 20 \text{ ns}) = 0.85$ due to the static magnetic order in parts of the sample volume. This fast depolarization is quenched by applying an external longitudinal field of 100 mT. This indicates, that the internal field is small compared to the applied external field. Empirical experience shows, that the internal field is around 1/10 of the applied external field, which decouples the muon spin from the internal-field distribution. Therefore, the internal field at the muon site is $\approx$ 10 mT. The time evolution of the muon spin polarization for applied longitudinal fields of 100 mT and 400 mT is equal and shows an exponential relaxation with a relaxation rate of $\lambda_{100\text{K},400\text{mT}} = 0.08(1)$ MHz. This provides evidence for fluctuating fields at the muon site at 100 K. The ZF spectrum at 70 K shows a fast depolarization from $P(t = 0) = 1.0$ to $P(t = 20 \text{ ns}) = 0.8$ due to the static magnetic order in parts of the sample volume. The enlarged reduction of the polarization by 20 %, compared to the 15 % at 100 K, indicates an increased volume fraction showing static order. This fast depolarization is quenched by applying an external longitudinal field of 100 mT similar to the LF measurements at 100 K indicating a similar internal field at the muon stopping site for both temperatures. Additionally, no change in $P(t)$ at applied longitudinal fields between 100 mT and 400 mT is observed. At both applied fields, an exponential relaxation with a relaxation rate of $\lambda_{70\text{K},400\text{mT}} = 0.32(1)$ MHz is observed, which is enhanced compared to $\lambda_{100 \text{ K}}$ indicating an increase of the magnetic field fluctuations. The ZF spectrum at 50 K shows a fast depolarization from $P(t = 0) = 1.00$ to $P(t = 20 \text{ ns}) = 0.33$ due to the static magnetic order in 100 % of the sample volume. By applying an external longitudinal field of 400 mT, the amplitude of the fast relaxation is reduced resulting in $P(t = 20 \text{ ns}) = 0.6$. This indicates, that the internal field at the muon stopping site is of the order of the external field. This is in good agreement with the internal magnetic field of 86(7) mT obtained by ZF measurement. The exponential relaxation rate at 400 mT has a value of $\lambda_{50\text{K},400\text{mT}} = 0.8(1)$ MHz. This indicates the presence of magnetic fluctuations slightly below the magnetic transition temperature of 55 K.

(a)

(b)

(c)
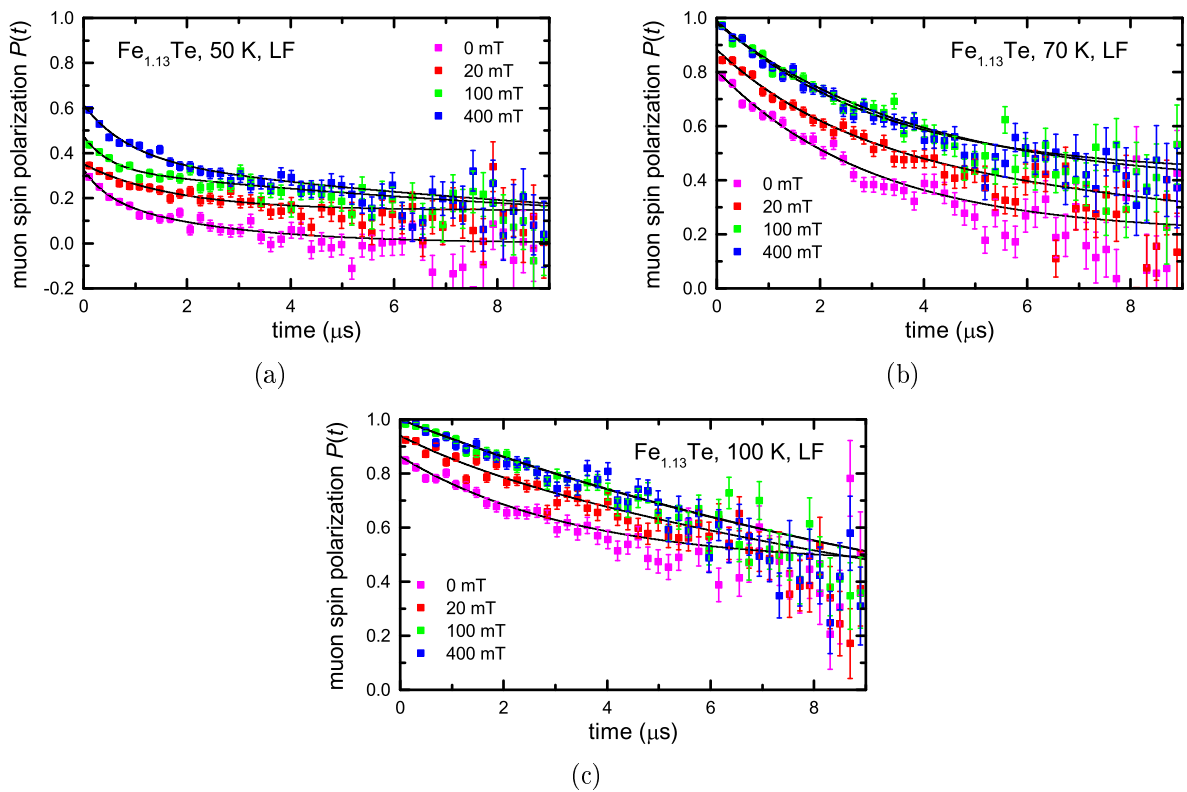
Figure 6.16.: Field dependence of the time evolution of the muon spin polarization at 50 K, 70 K, and 100 K in external longitudinal fields up to 400 mT. The exponential relaxation at 400 mT indicates fluctuating magnetic fields at the muon stopping site.

6.4. Summary - The magnetic phase diagram of $Fe_{1+y}Te$

The phase diagram of $Fe_{1+y}Te$ was studied in detail by ^{57}Fe-Mössbauer and muon spin relaxation spectroscopy. The results of the investigations are summarized and illustrated in Fig. 6.17, which is a modification of the phase diagram (Fig. 6.5) presented at the beginning of Sec. 6.1. At room temperature, an exponential relaxation of the muon spin polarization is observed for $y = 0.06$, 0.12, and 0.13. μSR-measurements in longitudinal field geometry for $y = 0.13$ prove, that this exponential relaxation is caused by fluctuating fields at the muon stopping site. This is in agreement with recent x-ray emission spectroscopy measurements observing a paramagnetic fluctuating moment, which is constant within error bars for $Fe_{1.03}Te$ and $Fe_{1.12}Te$ [166]. DFT+DMFT calculations provide evidence for fluctuating paramagnetic moments in FeTe which are of the order of the observed paramagnetic moments by x-ray emission spectroscopy in $Fe_{1.03}Te$ and $Fe_{1.14}Te$ [165, 166]. This indicate, that the fluctuating paramagnetic moments are independent of the excess-iron level. This implies, that mostly the iron atoms occupying the 2a site contribute to the fluctuating paramagnetic moment, as in FeTe the occupation of the 2c site is zero.

The magnetic transition temperatures, obtained by Mössbauer spectroscopy and muon spin relaxation experiments, are summarized in Tab. 6.1

$Fe_{1+y}Te$	$T_N^{100\%}$	T_N^{onset}	
$Fe_{1.06}Te$	65(2)	100(5)	μSR
	65(1)	72(2)	MBS
$Fe_{1.12}Te$	55(1)	110(5)	μSR
$Fe_{1.13}Te$	60(1)	100(5)	μSR
	60(1)	80(5)	MBS
$Fe_{1.15}Te$	60(5)	85(5)	MBS

Table 6.1.: Summary of the magnetic transition temperatures, obtained by Mössbauer (MBS) and muon spin relaxation (μSR) experiments, of the investigated compounds with $y = 0.06$, 0.12, 0.13 and 0.15. T_N^{onset} denotes the highest temperature with a finite magnetic volume fraction, which corresponds to the temperature, where the Mössbauer linewidth shows an abrupt increase. $T_N^{100\%}$ denotes the highest temperature, where a magnetic volume fraction of 100 % is observed.

These $T_N^{100\%}$ values are in good agreement with the magnetic transition temperatures obtained by macroscopic measurements (magnetic-susceptibility, specific heat, resistivity) and neutron-scattering experiments [156, 157, 159]. The discrepancy in T_N^{onset} between Mössbauer spectroscopy and μSR experiment originates in the different resolutions of both methods, as the μSR is able to detect smaller magnetic moments than the Mössbauer spectroscopy.

A magnetic precursor state is found for temperatures below 100 K. The onset of this precursor state is independent of the excess-iron level and characterized by an increase of the magnetic volume fraction from 0 at 100 K to 100 % at $T_N^{100\%}$. For temperatures below T_N^{onset}, a coherent sinusoidal oscillation of the muon spin as well as a well-resolved sextet
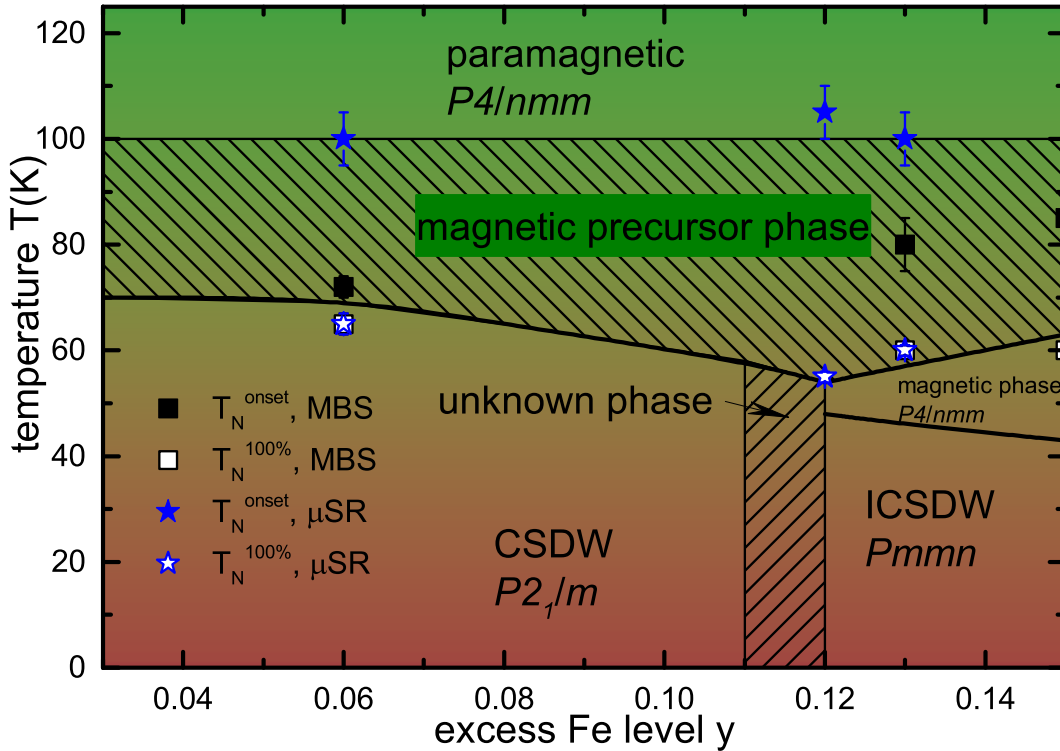
Figure 6.17.: Phase diagram of $Fe_{1+y}Te$ composed out of data taken from Ref. [155–157, 159, 165, 166, 168] as well as ^{57}Fe-Mössbauer spectroscopy and muon spin relaxation experiments. The high-temperature phase consists of a paramagnetic phase with tetragonal structure including fluctuating paramagnetic moments, which are independent of the excess-iron level. The colour code is red for static internal magnetic fields and green for fluctuating fields at the muon site corresponding to static and fluctuating magnetic moments. The transitions temperatures obtained by MBS and μSR experiments are illustrated as T_N^{onset} and $T_N^{100\%}$, where the former denotes the onset of magnetic order and the latter the temperature, where the magnetic volume fraction reaches 100 %. A magnetic precursor phase, which is independent of the excess-iron level, is found for temperatures below 100 K. For $y < 0.11$, the low-temperature phase consists of a commensurate spin density wave (SDW) phase and a monoclinic structure. For $y > 0.12$, two phase transitions occur. The transition at higher temperatures shows a complicated magnetic phase and a tetragonal structure. The low-temperature phase shows an incommensurate SDW state and an orthorhombic structure. A slowing down of the magnetic fluctuations is observed in the magnetically ordered state below T_N.

in the fully magnetically ordered state is observed for $y = 0.06$. This proves long-range commensurate magnetic order, which is consistent with the commensurate SDW found by neutron-scattering experiments [157, 159]. μSR measurements on $y = 0.12$ and 0.13 observe a coherent oscillation of the muon spin, which is modelled with a *0*th-order Bessel function indicating long-range incommensurate magnetic order. Mössbauer spectroscopy measurements on $y = 0.13$ and 0.15 show a rectangular field distribution. These results for $y = 0.12, 0.13$, and 0.15 are consistent with the magnetic structure obtained by neutron-scattering experiments, where an incommensurate SDW is found [157, 159]. Furthermore, a slowing down of the field fluctuations at the muon stopping sites in the fully magnetically ordered state is observed. Therefore, the paramagnetic high-temperature phase is more dynamic than the magnetically ordered low-temperature phase.

The magnetic structure in $Fe_{1.13}Te$ at temperatures below the magnetic and above the structural phase transition is still unclear. To solve this problem with Mössbauer spectroscopy, high-quality single crystals instead of powder are necessary.

6. Mössbauer and muon spin relaxation spectroscopy of $Fe_{1+y}Te$

7. Conclusion

In this work, the magnetic and superconducting properties of two specific series of iron pnictides and chalcogenides were studied using muon spin relaxation and Mössbauer spectroscopy.

In $Ca_{1-x}Na_xFe_2As_2$, the focus of interest was set to the crossover from magnetic order to superconductivity. Using local magnetic probes and samples with the Na-substitution levels $x = 0.00$, 0.35, 0.50, and 0.67, an updated phase diagram is derived. It was found, that the magnetic order is suppressed as a function of x and is persistent even at highest achievable Na-substitution levels, where a superconducting transition temperature of $T_c = 34$ K at $x = 0.67$ is observed. The suppression of the magnetic order is accompanied by a tilting of the magnetic moments out of the ab-plane as a function of x. For $x = 0.50$, a reduction of the magnetic order parameter below T_c is observed proving, together with a magnetic volume fraction of 100 % and a full diamagnetic signal, the coexistence of magnetic order and superconductivity in the same sample volume. The magnitude of the reduction of the magnetic order parameter is explained using Landau theory. Using the Landau theory, a clear correlation between the reduction of the magnetic order parameter in the superconducting state and the ratio of the ordering temperatures, T_c/T_N, could be quantitatively described. Further investigations of the lattice dynamics reveal no change of the phonon system at the magneto-structural phase transition. However, a softening of the lattice for finite x compared to the undoped compound is found.
In the optimally doped sample ($x = 0.67$) with $T_c = 34$ K, diluted magnetism is found coexisting with the superconducting phase. Analysing the temperature dependence of the magnetic penetration depth results in two superconducting gaps showing the multi-band character of the iron pnictides.

In $Fe_{1+y}Te$, the focus of interest was set to examine the unusual behaviour, that the magnetic phase transition temperature is higher than the structural transition temperature, which is unique among the iron pnictides and chalcogenides. The type of the magnetic order changes from a commensurate to an incommensurate spin density wave as a function of the excess iron level y. In contrast, an y-independent magnetic precursor phase below 100 K is found. This is surprising, as $T_N^{100\%}$, which is the highest temperature where 100 % of the sample show magnetic order, changes as a function of y. Additionally, fluctuating paramagnetic moments at room temperature are observed. Upon cooling, the fluctuation rate decreases and a static magnetic phase is found at lowest temperatures.

This work shows, that the understanding of the interplay between magnetism and superconductivity is crucial. Some specific questions were answered, but new question were raised. The most important question is connected to the undoped and fully doped compounds of the 122 iron pnictides. By increasing the c-axis parameter from $CaFe_2As_2$ to $CsFe_2As_2$ and, therefore, increasing the FeAs interlayer distance, the magnetic order is suppressed and superconductivity emerges. The first question is, if this change in the

electronic ground state is just based on the structure due to the increased c-axis parameter and, therefore, an increased FeAs interlayer distance or if the reduced electron count, because of the hole doping character of the alkaline-earth metal to alkaline metal substitution, is also important. The second question is, if this general trend of the change in the ground state due to the increased c-axis parameter can also be applied to the doped 122 compounds. The consequential question is, if it is possible to control the suppression of the magnetic order parameter down to a certain value, where the magnetic order is weak enough to mediate the Cooper pairing, just by changing the c-axis parameter. To answer this question, further experiments together with theoretical studies are necessary.

Room temperature superconductivity is still in the distant future, but a step in the right direction is done to remove the fiction out of the science fiction.

A. Momentum displacement operator

Let $|k\rangle$ be an eigenstate of the momentum operator $\hat{k}$ with the eigenvalue k:

$$\hat{k}\,|k\rangle = k\,|k\rangle. \tag{A.1}$$

The commutator of $\hat{k}$ with an arbitary operator $\mathrm{F}(\vec{x}, \vec{k})$ is given by

$$\left[F(\vec{x}, \vec{k}), \hat{k}\right] = -i\frac{\partial}{\partial\hat{x}}F(\vec{x}, \vec{k}), \tag{A.2}$$

where $\hat{x}$ denotes the position operator. Let the displacement operator $D(\eta)$ be defined as

$$D(\eta) = \mathrm{e}^{i\eta\hat{x}}. \tag{A.3}$$

The commutator between $D(\eta)$ and $\hat{k}$ is given by

$$\left[D(\eta), \hat{k}\right] = -\eta D(\eta). \tag{A.4}$$

Applying this commutator to the eigenstate $|k\rangle$ gives

$$\begin{aligned}\left[D(\eta), \hat{k}\right]|k\rangle &= -\eta D(\eta) \\ &= D(\eta)\hat{k}\,|k\rangle - \hat{k}D(\eta)\,|k\rangle, \end{aligned} \tag{A.5}$$

which leads to the following expression

$$\hat{k}D(\eta)\,|k\rangle = \{k + \eta\}\,D(\eta)\,|k\rangle. \tag{A.6}$$

Hence, $D(\eta)\,|k\rangle$ is an eigenvector of $\hat{k}$ with the eigenvalue $\{k + \eta\}$, and a new eigenvector can be defined:

$$D(\eta)\,|k\rangle = \underbrace{\mathrm{e}^{i\varphi}}_{\overset{!}{=}1}\,|k + \eta\rangle = |k + \eta\rangle, \tag{A.7}$$

where $\varphi \in \mathbb{C}$ is a complex phase and $\mathrm{e}^{i\varphi}$ is chosen to be 1. Thus it was shown, that $\mathrm{e}^{i\eta\hat{x}}$ is a displacement vector and the relation

$$\mathrm{e}^{i\eta\hat{x}}\,|k\rangle = |k + \eta\rangle \tag{A.8}$$

is valid.

A. Momentum displacement operator

List of Figures

List of Tables

List of Tables

Bibliography

[1] J. Cameron and W. Wisher, *Terminator 2: Judgement Day*, 1991.

[2] S. L. Bud'ko, G. Lapertot, C. Petrovic, C. E. Cunningham, N. Anderson, and P. C. Canfield, Phys. Rev. Lett. **86**, 1877 (2001).

[3] J. Bardeen, L. N. Cooper, and J. R. Schrieffer, Phys. Rev. **108**, 1175 (1957).

[4] C. W. Chu, L. Gao, F. Chen, Z. J. Huang, R. L. Meng, and Y. Y. Xue, Nature **365**, 323 (1993).

[5] Y. Kamihara, T. Watanabe, M. Hirano, and H. Hosono, J. Am. Chem. Soc. **130**, 3296 (2008).

[6] A. Schenck, *Muon spin rotation spectroscopy* (CRC Press, 1985).

[7] J. Sonier, TRIUMF Web Sites (2001).

[8] P. D. de Réotier and A Yaouanc, J. Phys. Condens. Matter **9**, 9113 (1997).

[9] R. S. Hayano, Y. J. Uemura, J. Imazato, N. Nishida, T. Yamazaki, and R. Kubo, Phys. Rev. B **20**, 850 (1979).

[10] M. Larkin, Y. Fudamoto, I. Gat, A. Kinkhabwala, K. Kojima, G. Luke, J. Merrin, B. Nachumi, Y. Uemura, M. Azuma, T. Saito, and M. Takano, Physica B **289-290**, 153 (2000).

[11] A. Overhauser, J. Phys. Chem. Solids **13**, 71 (1960).

[12] C. Timm, *Lecture: theory of superconductivity.*

[13] E. H. Brandt, Phys. Rev. B **37**, 2349 (1988).

[14] J. E. Sonier, J. H. Brewer, and R. F. Kiefl, Rev. Mod. Phys. **72**, 769 (2000).

[15] T. M. Riseman, J. H. Brewer, K. H. Chow, W. N. Hardy, R. F. Kiefl, S. R. Kreitzman, R. Liang, W. A. MacFarlane, P. Mendels, G. D. Morris, J. Rammer, J. W. Schneider, C. Niedermayer, and S. L. Lee, Phys. Rev. B **52**, 10569 (1995).

[16] A. Maisuradze, R. Khasanov, A. Shengelaya, and H. Keller, J. Phys. Condens. Matter **21**, 075701 (2009).

[17] E. Brandt, J. Low Temp. Phys. **73**, 355 (1988).

[18] D. Cardwell and D. Ginley, *Handbook of superconducting materials*, Bd. 1 (Institute of Physics, 2003).

[19] M. Tinkham, *Introduction to Superconductivity*, Dover Books on Physics Series (Dover Publications, Incorporated, 2012).

[20] A. Carrington and F. Manzano, Physica C **385**, 205 (2003).

[21]   D. V. Evtushinsky, D. S. Inosov, V. B. Zabolotnyy, M. S. Viazovska, R. Khasanov, A. Amato, H.-H. Klauss, H. Luetkens, C. Niedermayer, G. L. Sun, V. Hinkov, C. T. Lin, A. Varykhalov, A. Koitzsch, M. Knupfer, B. Büchner, A. A. Kordyuk, and S. V. Borisenko, N. J. Phys. **11**, 055069 (2009).

[22]   A. A. Golubov, A. Brinkman, O. V. Dolgov, J. Kortus, and O. Jepsen, Phys. Rev. B **66**, 054524 (2002).

[23]   R. L. Mössbauer, German, Z. Phys. **151**, 124 (1958).

[24]   D. Barb, *Grundlagen und Anwendungen der Mössbauerspektroskopie* (Berlin, Akademie-Verlag, 1980).

[25]   D.-P. Y. Yi-Long Chen, *Mössbauer effect in lattice dynamics* (WILEY-VCH, 2007).

[26]   R. J. Glauber, Phys. Rev. **131**, 2766 (1963).

[27]   J. Gazeau, *Coherent states in quantum physics* (Wiley, 2009).

[28]   D. S. Bateman, S. K. Bose, B. DuttaRoy, and M. Bhattacharyya, Am. J. Phys. **60**, 829 (1992).

[29]   H. J. Lipkin, Ann. Phys. **18**, 182 (1962).

[30]   S. Wang, Phys. Rev. A **60**, 262 (1999).

[31]   G. Schatz and A. Weidinger, *Nukleare Festkörperphysik: kernphysikalische Messmethoden und ihre Anwendungen*, Teubner-Studienbücher: Physik (Teubner, 1997).

[32]   S. Kamusella, *MoessFit: A Free Framework for ^{57}Fe Mössbauer Data Analysis*, (private communication).

[33]   B. Matthias, V. Compton, and E. Corenzwit, J. Phys. Chem. Solids **19**, 130 (1961).

[34]   B. Chandrasekhar and J. Hulm, J. Phys. Chem. Solids **7**, 259 (1958).

[35]   H. F. Braun, Phys. Lett. A **75**, 386 (1980).

[36]   H. Luetkens, H.-H. Klauss, M. Kraken, F. J. Litterst, T. Dellmann, R. Klingeler, C. Hess, R. Khasanov, A. Amato, C. Baines, M. Kosmala, O. J. Schumann, M. Braden, J. Hamann-Borrero, N. Leps, A. Kondrat, G. Behr, J. Werner, and B. Büchner, Nat. Mater. **8**, 305 (2009).

[37]   H.-H. Klauss, H. Luetkens, R. Klingeler, C. Hess, F. J. Litterst, M. Kraken, M. M. Korshunov, I. Eremin, S.-L. Drechsler, R. Khasanov, A. Amato, J. Hamann-Borrero, N. Leps, A. Kondrat, G. Behr, J. Werner, and B. Büchner, Phys. Rev. Lett. **101**, 077005 (2008).

[38]   A. D. Christianson, M. D. Lumsden, O. Delaire, M. B. Stone, D. L. Abernathy, M. A. McGuire, A. S. Sefat, R. Jin, B. C. Sales, D. Mandrus, E. D. Mun, P. C. Canfield, J. Y. Y. Lin, M. Lucas, M. Kresch, J. B. Keith, B. Fultz, E. A. Goremychkin, and R. J. McQueeney, Phys. Rev. Lett. **101**, 157004 (2008).

[39]   L. Boeri, O. V. Dolgov, and A. A. Golubov, Phys. Rev. Lett. **101**, 026403 (2008).

[40]   I. Mazin and J. Schmalian, Physica C **469**, 614 (2009).

[41] M. D. Lumsden and A. D. Christianson, J. Phys. Condens. Matter **22**, 203203 (2010).

[42] D. C. Johnston, Adv. Phys. **59**, 803 (2010).

[43] D. Johrendt, J. Mater. Chem. **21**, 13726 (2011).

[44] P. J. Hirschfeld, M. M. Korshunov, and I. I. Mazin, Rep. Prog. Phys. **74**, 124508 (2011).

[45] G. R. Stewart, Rev. Mod. Phys. **83**, 1589 (2011).

[46] K. Zhao, Q. Q. Liu, X. C. Wang, Z. Deng, Y. X. Lv, J. L. Zhu, F. Y. Li, and C. Q. Jin, Phys. Rev. B **84**, 184534 (2011).

[47] L. Harnagea, S. Singh, G. Friemel, N. Leps, D. Bombor, M. Abdel-Hafiez, A. U. B. Wolter, C. Hess, R. Klingeler, G. Behr, S. Wurmehl, and B. Büchner, Phys. Rev. B **83**, 094523 (2011).

[48] M. Pfisterer and G. Nagorsen, Z. Naturforsch. B **35** (1980).

[49] M. Rotter, M. Tegel, D. Johrendt, I. Schellenberg, W. Hermes, and R. Pöttgen, Phys. Rev. B **78**, 020503 (2008).

[50] A. Jesche, N. Caroca-Canales, H. Rosner, H. Borrmann, A. Ormeci, D. Kasinathan, H. H. Klauss, H. Luetkens, R. Khasanov, A. Amato, A. Hoser, K. Kaneko, C. Krellner, and C. Geibel, Phys. Rev. B **78**, 180504 (2008).

[51] A. I. Goldman, D. N. Argyriou, B. Ouladdiaf, T. Chatterji, A. Kreyssig, S. Nandi, N. Ni, S. L. Bud'ko, P. C. Canfield, and R. J. McQueeney, Phys. Rev. B **78**, 100506 (2008).

[52] Q. Huang, Y. Qiu, W. Bao, M. A. Green, J. W. Lynn, Y. C. Gasparovic, T. Wu, G. Wu, and X. H. Chen, Phys. Rev. Lett. **101**, 257003 (2008).

[53] A. Cano, M. Civelli, I. Eremin, and I. Paul, Phys. Rev. B **82**, 020408 (2010).

[54] K. Sasmal, B. Lv, B. Lorenz, A. M. Guloy, F. Chen, Y.-Y. Xue, and C.-W. Chu, Phys. Rev. Lett. **101**, 107007 (2008).

[55] Z. Bukowski, S. Weyeneth, R. Puzniak, J. Karpinski, and B. Batlogg, Physica C **470, Supplement 1**, Proceedings of the 9th International Conference on Materials and Mechanisms of Superconductivity, S328 (2010).

[56] M. Bendele, P. Babkevich, S. Katrych, S. N. Gvasaliya, E. Pomjakushina, K. Conder, B. Roessli, A. T. Boothroyd, R. Khasanov, and H. Keller, Phys. Rev. B **82**, 212504 (2010).

[57] F.-C. Hsu, J.-Y. Luo, K.-W. Yeh, T.-K. Chen, T.-W. Huang, P. M. Wu, Y.-C. Lee, Y.-L. Huang, Y.-Y. Chu, D.-C. Yan, and M.-K. Wu, Proc. Natl. Acad. Sci. **105**, 14262 (2008).

[58] B. C. Sales, A. S. Sefat, M. A. McGuire, R. Y. Jin, D. Mandrus, and Y. Mozharivskyj, Phys. Rev. B **79**, 094521 (2009).

[59] D. Fruchart, P. Convert, P. Wolfers, R. Madar, J. Senateur, and R. Fruchart, Mater. Res. Bull. **10**, 169 (1975).

[60] A. Subedi, L. Zhang, D. J. Singh, and M. H. Du, Phys. Rev. B **78**, 134514 (2008).

[61] D. N. Basov and A. V. Chubukov, Nat. Phys. **7**, 272 (2011).

[62] J. T. Park, D. S. Inosov, C. Niedermayer, G. L. Sun, D. Haug, N. B. Christensen, R. Dinnebier, A. V. Boris, A. J. Drew, L. Schulz, T. Shapoval, U. Wolff, V. Neu, X. Yang, C. T. Lin, B. Keimer, and V. Hinkov, Phys. Rev. Lett. **102**, 117006 (2009).

[63] A. J. Drew, C. Niedermayer, P. J. Baker, F. L. Pratt, S. J. Blundell, T. Lancaster, R. H. Liu, G. Wu, X. H. Chen, I. Watanabe, V. K. Malik, A. Dubroka, M. Rossle, K. W. Kim, C. Baines, and C. Bernhard, Nat. Mater. **8**, 310 (2009).

[64] S. Sanna, R. De Renzi, G. Lamura, C. Ferdeghini, A. Palenzona, M. Putti, M. Tropeano, and T. Shiroka, Phys. Rev. B **80**, 052503 (2009).

[65] H. Maeter, G. Pascua, H. Luetkens, J. Knolle, S. Aswartham, S. Wurmehl, G. Behr, B. Büchner, Z. Shermadini, K. Sedlak, A. Amato, R. Moessner, I. Eremin, and H.-H. Klauss, arXiv **1210.6881v1** (2012).

[66] G Wu, H Chen, T Wu, Y. L. Xie, Y. J. Yan, R. H. Liu, X. F. Wang, J. J. Ying, and X. H. Chen, J. Phys. Condens. Matter **20**, 422201 (2008).

[67] G. F. Chen, Z. Li, J. Dong, G. Li, W. Z. Hu, X. D. Zhang, X. H. Song, P. Zheng, N. L. Wang, and J. L. Luo, Phys. Rev. B **78**, 224512 (2008).

[68] D. Singh, Physica C **469**, 418 (2009).

[69] A. B. Vorontsov, M. G. Vavilov, and A. V. Chubukov, Phys. Rev. B **81**, 174538 (2010).

[70] M. G. Vavilov, A. V. Chubukov, and A. B. Vorontsov, Sup. Sci. Technol. **23**, 054011 (2010).

[71] G. Liu, H. Liu, L. Zhao, W. Zhang, X. Jia, J. Meng, X. Dong, J. Zhang, G. F. Chen, G. Wang, Y. Zhou, Y. Zhu, X. Wang, Z. Xu, C. Chen, and X. J. Zhou, Phys. Rev. B **80**, 134519 (2009).

[72] M. Neupane, P. Richard, Y.-M. Xu, K. Nakayama, T. Sato, T. Takahashi, A. V. Federov, G. Xu, X. Dai, Z. Fang, Z. Wang, G.-F. Chen, N.-L. Wang, H.-H. Wen, and H. Ding, Phys. Rev. B **83**, 094522 (2011).

[73] C. Liu, T. Kondo, N. Ni, A. D. Palczewski, A. Bostwick, G. D. Samolyuk, R. Khasanov, M. Shi, E. Rotenberg, S. L. Bud'ko, P. C. Canfield, and A. Kaminski, Phys. Rev. Lett. **102**, 167004 (2009).

[74] R. Gonnelli, M. Tortello, D. Daghero, P. Pecchio, S. Galasso, V. Stepanov, Z. Bukowski, N. Zhigadlo, J. Karpinski, K. Iida, and B. Holzapfel, English, J. Supercond. Nov. Magn. **26**, 1331 (2013).

[75] S. Avci, O. Chmaissem, D. Y. Chung, S. Rosenkranz, E. A. Goremychkin, J. P. Castellan, I. S. Todorov, J. A. Schlueter, H. Claus, A. Daoud-Aladine, D. D. Khalyavin, M. G. Kanatzidis, and R. Osborn, Phys. Rev. B **85**, 184507 (2012).

[76] T. Kondo, R. M. Fernandes, R. Khasanov, C. Liu, A. D. Palczewski, N. Ni, M. Shi, A. Bostwick, E. Rotenberg, J. Schmalian, S. L. Bud'ko, P. C. Canfield, and A. Kaminski, Phys. Rev. B **81**, 060507 (2010).

[77] D. V. Evtushinsky, V. B. Zabolotnyy, L. Harnagea, A. N. Yaresko, S. Thirupathaiah, A. A. Kordyuk, J. Maletz, S. Aswartham, S. Wurmehl, E. Rienks, R. Follath, B. Büchner, and S. V. Borisenko, Phys. Rev. B **87**, 094501 (2013).

[78] C. Liu, G. D. Samolyuk, Y. Lee, N. Ni, T. Kondo, A. F. Santander-Syro, S. L. Bud'ko, J. L. McChesney, E. Rotenberg, T. Valla, A. V. Fedorov, P. C. Canfield, B. N. Harmon, and A. Kaminski, Phys. Rev. Lett. **101**, 177005 (2008).

[79] R. M. Fernandes, D. K. Pratt, W. Tian, J. Zarestky, A. Kreyssig, S. Nandi, M. G. Kim, A. Thaler, N. Ni, P. C. Canfield, R. J. McQueeney, J. Schmalian, and A. I. Goldman, Phys. Rev. B **81**, 140501 (2010).

[80] J. Schmiedt, P. M. R. Brydon, and C. Timm, Phys. Rev. B **89**, 054515 (2014).

[81] T. A. Maier, S. Graser, D. J. Scalapino, and P. J. Hirschfeld, Phys. Rev. B **79**, 224510 (2009).

[82] A. V. Chubukov, M. G. Vavilov, and A. B. Vorontsov, Phys. Rev. B **80**, 140515 (2009).

[83] R. Thomale, C. Platt, J. Hu, C. Honerkamp, and B. A. Bernevig, Phys. Rev. B **80**, 180505 (2009).

[84] V. Cvetkovic and Z. Tesanovic, Europhys. Lett. **85**, 37002 (2009).

[85] F. Wang, H. Zhai, Y. Ran, A. Vishwanath, and D.-H. Lee, Phys. Rev. Lett. **102**, 047005 (2009).

[86] C. Platt, C. Honerkamp, and W. Hanke, N. J. Phys. **11**, 055058 (2009).

[87] S. Raghu, X.-L. Qi, C.-X. Liu, D. J. Scalapino, and S.-C. Zhang, Phys. Rev. B **77**, 220503 (2008).

[88] J. Lorenzana, G. Seibold, C. Ortix, and M. Grilli, Phys. Rev. Lett. **101**, 186402 (2008).

[89] P. M. R. Brydon and C. Timm, Phys. Rev. B **79**, 180504 (2009).

[90] M. D. Johannes and I. I. Mazin, Phys. Rev. B **79**, 220510 (2009).

[91] I. Eremin and A. V. Chubukov, Phys. Rev. B **81**, 024511 (2010).

[92] I. I. Mazin and M. D. Johannes, Nat. Phys. **5**, 141 (2009).

[93] R. D. Shannon, Acta Crystallogr. Sec. A **32**, 751 (1976).

[94] K. Momman and F. Izumi, *VESTA3 for three-dimensional visualization of crystal, volumetric and morphology data*, 2011.

[95] P. M. Shirage, K. Miyazawa, H. Kito, H. Eisaki, and A. Iyo, Appl. Phys. Express **1**, 081702 (2008).

[96] N. Ni, S. Nandi, A. Kreyssig, A. I. Goldman, E. D. Mun, S. L. Bud'ko, and P. C. Canfield, Phys. Rev. B **78**, 014523 (2008).

[97] J. Zhao, W. Ratcliff, J. W. Lynn, G. F. Chen, J. L. Luo, N. L. Wang, J. Hu, and P. Dai, Phys. Rev. B **78**, 140504 (2008).

[98] R. Cortes-Gil and S. J. Clarke, Chem. Mater. **23**, 1009 (2011).

[99]   R. Cortes-Gil, D. R. Parker, M. J. Pitcher, J. Hadermann, and S. J. Clarke, Chem. Mater. **22**, 4304 (2010).

[100] S. Johnston, M. Abdel-Hafiez, L. Harnagea, V. Grinenko, D. Bombor, Y. Krupskaya, C. Hess, S. Wurmehl, A. U. B. Wolter, B. Büchner, H. Rosner, and S.-L. Drechsler, Phys. Rev. B **89**, 134507 (2014).

[101] A. Suter and B. Wojek, Phys. Procedia **30**, 69 (2012).

[102] S. Aswartham, M. Abdel-Hafiez, D. Bombor, M. Kumar, A. U. B. Wolter, C. Hess, D. V. Evtushinsky, V. B. Zabolotnyy, A. A. Kordyuk, T. K. Kim, S. V. Borisenko, G. Behr, B. Büchner, and S. Wurmehl, Phys. Rev. B **85**, 224520 (2012).

[103] R. Klingeler, N. Leps, I. Hellmann, A. Popa, U. Stockert, C. Hess, V. Kataev, H.-J. Grafe, F. Hammerath, G. Lang, S. Wurmehl, G. Behr, L. Harnagea, S. Singh, and B. Büchner, Phys. Rev. B **81**, 024506 (2010).

[104] G. M. Zhang, Y. H. Su, Z. Y. Lu, Z. Y. Weng, D. H. Lee, and T. Xiang, Europhys. Lett. **86**, 37006 (2009).

[105] Y. G. Pashkevich, *private communication.*

[106] A. A. Aczel, E. Baggio-Saitovitch, S. L. Budko, P. C. Canfield, J. P. Carlo, G. F. Chen, P. Dai, T. Goko, W. Z. Hu, G. M. Luke, J. L. Luo, N. Ni, D. R. Sanchez-Candela, F. F. Tafti, N. L. Wang, T. J. Williams, W. Yu, and Y. J. Uemura, Phys. Rev. B **78**, 214503 (2008).

[107] R. Scheuermann, E. Roduner, G. Engelhardt, H.-H. Klauss, and D. Herlach, Phys. Rev. B **66**, 144429 (2002).

[108] M. Gooch, B. Lv, K. Sasmal, J. Tapp, Z. Tang, A. Guloy, B. Lorenz, and C. Chu, Physica C **470, Supplement 1**, Proceedings of the 9th International Conference on Materials and Mechanisms of Superconductivity, S276 (2010).

[109] M. Tegel, M. Rotter, V. Weiß, F. M. Schappacher, R. Pöttgen, and D. Johrendt, J. Phys. Condens. Matter **20**, 452201 (2008).

[110] M. Rotter, M. Pangerl, M. Tegel, and D. Johrendt, Angew. Chem. Int. Ed. **47**, 7949 (2008).

[111] E. Wiesenmayer, H. Luetkens, G. Pascua, R. Khasanov, A. Amato, H. Potts, B. Banusch, H.-H. Klauss, and D. Johrendt, Phys. Rev. Lett. **107**, 237001 (2011).

[112] S. Avci, J. M. Allred, O. Chmaissem, D. Y. Chung, S. Rosenkranz, J. A. Schlueter, H. Claus, A. Daoud-Aladine, D. D. Khalyavin, P. Manuel, A. Llobet, M. R. Suchomel, M. G. Kanatzidis, and R. Osborn, Phys. Rev. B **88**, 094510 (2013).

[113] G. Sun, D. Sun, M. Konuma, P. Popovich, A. Boris, J. Peng, K.-Y. Choi, P. Lemmens, and C. Lin, J. Supercond. Nov. Magn. **24**, 1773 (2011).

[114] Y. Qi, X. Zhang, Z. Gao, Z. Zhang, L. Wang, D. Wang, and Y. Ma, Physica C **469**, 717 (2009).

[115] Y. Li and J. Ni, Solid State Commun. **151**, 446 (2011).

[116] T. Goko, A. A. Aczel, E. Baggio-Saitovitch, S. L. Bud'ko, P. C. Canfield, J. P. Carlo, G. F. Chen, P. Dai, A. C. Hamann, W. Z. Hu, H. Kageyama, G. M. Luke, J. L. Luo, B. Nachumi, N. Ni, D. Reznik, D. R. Sanchez-Candela, A. T. Savici, K. J. Sikes, N. L. Wang, C. R. Wiebe, T. J. Williams, T. Yamamoto, W. Yu, and Y. J. Uemura, Phys. Rev. B **80**, 024508 (2009).

[117] M. Alzamora, J. Munevar, E. Baggio-Saitovitch, S. L. Bud'ko, N. Ni, P. C. Canfield, and D. R. Sánchez, J. Phys. Condens. Matter **23**, 145701 (2011).

[118] D. Kasinathan, A. Ormeci, K. Koch, U. Burkhardt, W. Schnelle, A. Leithe-Jasper, and H. Rosner, N. J. Phys. **11**, 025023 (2009).

[119] H. Suhl, J. L. Com. Metals **62**, 225 (1978).

[120] T. K. Kopec and J. Klamut, Phys. Status Solidi B **137**, 73 (1986).

[121] R. M. Fernandes and J. Schmalian, Phys. Rev. B **82**, 014521 (2010).

[122] C. R. Rotundu, W. Tian, K. C. Rule, T. R. Forrest, J. Zhao, J. L. Zarestky, and R. J. Birgeneau, Phys. Rev. B **85**, 144506 (2012).

[123] S. Avci, O. Chmaissem, E. A. Goremychkin, S. Rosenkranz, J.-P. Castellan, D. Y. Chung, I. S. Todorov, J. A. Schlueter, H. Claus, M. G. Kanatzidis, A. Daoud-Aladine, D. Khalyavin, and R. Osborn, Phys. Rev. B **83**, 172503 (2011).

[124] M. G. Kim, D. K. Pratt, G. E. Rustan, W. Tian, J. L. Zarestky, A. Thaler, S. L. Bud'ko, P. C. Canfield, R. J. McQueeney, A. Kreyssig, and A. I. Goldman, Phys. Rev. B **83**, 054514 (2011).

[125] A. Kreyssig, M. G. Kim, S. Nandi, D. K. Pratt, W. Tian, J. L. Zarestky, N. Ni, A. Thaler, S. L. Bud'ko, P. C. Canfield, R. J. McQueeney, and A. I. Goldman, Phys. Rev. B **81**, 134512 (2010).

[126] P. Wang, Z. M. Stadnik, J. Zukrowski, A. Thaler, S. L. Bud'ko, and P. C. Canfield, Phys. Rev. B **84**, 024509 (2011).

[127] H. Luo, R. Zhang, M. Laver, Z. Yamani, M. Wang, X. Lu, M. Wang, Y. Chen, S. Li, S. Chang, J. W. Lynn, and P. Dai, Phys. Rev. Lett. **108**, 247002 (2012).

[128] S. Nandi, M. G. Kim, A. Kreyssig, R. M. Fernandes, D. K. Pratt, A. Thaler, N. Ni, S. L. Bud'ko, P. C. Canfield, J. Schmalian, R. J. McQueeney, and A. I. Goldman, Phys. Rev. Lett. **104**, 057006 (2010).

[129] P. Marsik, K. W. Kim, A. Dubroka, M. Rössle, V. K. Malik, L. Schulz, C. N. Wang, C. Niedermayer, A. J. Drew, M. Willis, T. Wolf, and C. Bernhard, Phys. Rev. Lett. **105**, 057001 (2010).

[130] A. D. Christianson, M. D. Lumsden, S. E. Nagler, G. J. MacDougall, M. A. McGuire, A. S. Sefat, R. Jin, B. C. Sales, and D. Mandrus, Phys. Rev. Lett. **103**, 087002 (2009).

[131] D. K. Pratt, M. G. Kim, A. Kreyssig, Y. B. Lee, G. S. Tucker, A. Thaler, W. Tian, J. L. Zarestky, S. L. Bud'ko, P. C. Canfield, B. N. Harmon, A. I. Goldman, and R. J. McQueeney, Phys. Rev. Lett. **106**, 257001 (2011).

[132] T. Yildirim, Physica C **469**, Superconductivity in Iron-Pnictides, 425 (2009).

[133] S. E. Hahn, Y. Lee, N. Ni, P. C. Canfield, A. I. Goldman, R. J. McQueeney, B. N. Harmon, A. Alatas, B. M. Leu, E. E. Alp, D. Y. Chung, I. S. Todorov, and M. G. Kanatzidis, Phys. Rev. B **79**, 220511 (2009).

[134] R. Mittal, S. K. Mishra, S. L. Chaplot, S. V. Ovsyannikov, E. Greenberg, D. M. Trots, L. Dubrovinsky, Y. Su, T. Brueckel, S. Matsuishi, H. Hosono, and G. Garbarino, Phys. Rev. B **83**, 054503 (2011).

[135] L. Chauvière, Y. Gallais, M. Cazayous, A. Sacuto, M. A. Méasson, D. Colson, and A. Forget, Phys. Rev. B **80**, 094504 (2009).

[136] R. Khasanov, D. Evtushinsky, A. Amato, H.-H. Klauss, H. Luetkens, C. Niedermayer, B. Büchner, G. Sun, C. Lin, J. Park, D. Inosov, and V. Hinkov, Phys. Rev. Lett. **102**, 187005 (2009).

[137] R. Prozorov and V. G. Kogan, Rep. Prog. Phys. **74**, 124505 (2011).

[138] R. Housley, N. Erickson, and J. Dash, Nucl. Instrum. and Methods **27**, 29 (1964).

[139] G. Lang, Nucl. Instrum. Methods **24**, 425 (1963).

[140] Z. Li, X. Ma, H. Pang, and F. Li, J. Phys. Condens. Matter **23**, 255701 (2011).

[141] A. Blachowski, K. Ruebenbauer, J. Zukrowski, J. Przewoznik, K. Wojciechowski, and Z. Stadnik, J. All. Comp. **494**, 1 (2010).

[142] R. S. Preston, Phys. Rev. Lett. **19**, 75 (1967).

[143] A. Blachowski, K. Ruebenbauer, J. Żukrowski, K. Rogacki, Z. Bukowski, and J. Karpinski, Phys. Rev. B **83**, 134410 (2011).

[144] M. Abdel-Hafiez, P. J. Pereira, S. A. Kuzmichev, T. E. Kuzmicheva, V. M. Pudalov, L. Harnagea, A. A. Kordyuk, A. V. Silhanek, V. V. Moshchalkov, B. Shen, H.-H. Wen, A. N. Vasiliev, and X.-J. Chen, Phys. Rev. B **90**, 054524 (2014).

[145] S. A. J. Kimber, A. Kreyssig, Y.-Z. Zhang, H. O. Jeschke, R. Valenti, F. Yokaichiya, E. Colombier, J. Yan, T. C. Hansen, T. Chatterji, R. J. McQueeney, P. C. Canfield, A. I. Goldman, and D. N. Argyriou, Nat. Mater. **8**, 471 (2009).

[146] C. Bernhard, A. J. Drew, L. Schulz, V. K. Malik, M. Rössle, C. Niedermayer, T. Wolf, G. D. Varma, G. Mu, H.-H. Wen, H. Liu, G. Wu, and X. H. Chen, N. J. Phys. **11**, 055050 (2009).

[147] J. E. Sonier, W. Huang, C. V. Kaiser, C. Cochrane, V. Pacradouni, S. A. Sabok-Sayr, M. D. Lumsden, B. C. Sales, M. A. McGuire, A. S. Sefat, and D. Mandrus, Phys. Rev. Lett. **106**, 127002 (2011).

[148] R. Khasanov, A. Maisuradze, H. Maeter, A. Kwadrin, H. Luetkens, A. Amato, W. Schnelle, H. Rosner, A. Leithe-Jasper, and H.-H. Klauss, Phys. Rev. Lett. **103**, 067010 (2009).

[149] T. J. Williams, A. A. Aczel, E. Baggio-Saitovitch, S. L. Bud'ko, P. C. Canfield, J. P. Carlo, T. Goko, H. Kageyama, A. Kitada, J. Munevar, N. Ni, S. R. Saha, K. Kirschenbaum, J. Paglione, D. R. Sanchez-Candela, Y. J. Uemura, and G. M. Luke, Phys. Rev. B **82**, 094512 (2010).

[150] K. Yosida, Phys. Rev. **110**, 769 (1958).

[151] T. Goltz, V. Zinth, D. Johrendt, H. Rosner, G. Pascua, H. Luetkens, P. Materne, and H.-H. Klauss, Phys. Rev. B **89**, 144511 (2014).

[152] S. L. Thiemann, Z. Radović, and V. G. Kogan, Phys. Rev. B **39**, 11406 (1989).

[153] R. Prozorov, M. Tanatar, R. Gordon, C. Martin, H. Kim, V. Kogan, N. Ni, M. Tillman, S. Bud'ko, and P. Canfield, Physica C **469**, 582 (2009).

[154] N. Haberkorn, B. Maiorov, M. Jaime, I. Usov, M. Miura, G. F. Chen, W. Yu, and L. Civale, Phys. Rev. B **84**, 064533 (2011).

[155] S. Rößler, D. Cherian, W. Lorenz, M. Doerr, C. Koz, C. Curfs, Y. Prots, U. K. Rößler, U. Schwarz, S. Elizabeth, and S. Wirth, Phys. Rev. B **84**, 174506 (2011).

[156] C. Koz, S. Rößler, A. A. Tsirlin, S. Wirth, and U. Schwarz, Phys. Rev. B **88**, 094509 (2013).

[157] E. E. Rodriguez, C. Stock, P. Zajdel, K. L. Krycka, C. F. Majkrzak, P. Zavalij, and M. A. Green, Phys. Rev. B **84**, 064403 (2011).

[158] L. Zhang, D. J. Singh, and M. H. Du, Phys. Rev. B **79**, 012506 (2009).

[159] W. Bao, Y. Qiu, Q. Huang, M. A. Green, P. Zajdel, M. R. Fitzsimmons, M. Zhernenkov, S. Chang, M. Fang, B. Qian, E. K. Vehstedt, J. Yang, H. M. Pham, L. Spinu, and Z. Q. Mao, Phys. Rev. Lett. **102**, 247001 (2009).

[160] Y. Xia, D. Qian, L. Wray, D. Hsieh, G. F. Chen, J. L. Luo, N. L. Wang, and M. Z. Hasan, Phys. Rev. Lett. **103**, 037002 (2009).

[161] S. Rößler, D. Cherian, S. Harikrishnan, H. L. Bhat, S. Elizabeth, J. A. Mydosh, L. H. Tjeng, F. Steglich, and S. Wirth, Phys. Rev. B **82**, 144523 (2010).

[162] A. Blachowski, K. Ruebenbauer, P. Zajdel, E. E. Rodriguez, and M. A. Green, J. Phys. Condens. Matter **24**, 386006 (2012).

[163] I. Paul, Phys. Rev. Lett. **107**, 047004 (2011).

[164] G. Lamura, T. Shiroka, P. Bonfà, S. Sanna, F. Bernardini, R. De Renzi, R. Viennois, E. Giannini, A. Piriou, N. Emery, M. R. Cimberle, and M. Putti, J. Phys. Condens. Matter **25**, 156004 (2013).

[165] Z. P. Yin, K. Haule, and G. Kotliar, Nat. Mater. **10**, 932 (2011).

[166] H. Gretarsson, A. Lupascu, J. Kim, D. Casa, T. Gog, W. Wu, S. R. Julian, Z. J. Xu, J. S. Wen, G. D. Gu, R. H. Yuan, Z. G. Chen, N.-L. Wang, S. Khim, K. H. Kim, M. Ishikado, I. Jarrige, S. Shamoto, J.-H. Chu, I. R. Fisher, and Y.-J. Kim, Phys. Rev. B **84**, 100509 (2011).

[167] Y. Liu, R. K. Kremer, and C. T. Lin, Sup. Sci. Technol. **24**, 035012 (2011).

[168] R. Khasanov, M. Bendele, A. Amato, P. Babkevich, A. T. Boothroyd, A. Cervellino, K. Conder, S. N. Gvasaliya, H. Keller, H.-H. Klauss, H. Luetkens, V. Pomjakushin, E. Pomjakushina, and B. Roessli, Phys. Rev. B **80**, 140511 (2009).

Danksagung

Ich möchte allen danken, die mich während der Promotion begleitet und diese damit überhaupt auch erst möglich gemacht haben.

Da wäre an aller erster Stelle der Doktorvater Prof. Hans-Henning Klauß zu nennen, in dessen Arbeitsgruppe diese Arbeit durchgeführt wurde. Die Arbeit in und mit der Arbeitsgruppe war im Allgemeinen ausgesprochen angenehm, was sich defintiv positiv ausgewirkt hat, da ich mich immer gefreut habe, ans Institut zu kommen. Da wären zu nennen: Hemke Maeter, Johannes Spehling, Til Goltz, Sirko Kamusella, Nicolas Yeche, Mathias Dörr und Rajib Sarkar. Desweiteren danke ich Elke Wachsmuth für die Hilfe bei all den nichtwissenschaftlichen Dingen, mit denen ich mich so rumplagen musste, sowie den angenehmen Gesprächen. Das gleiche gilt für Marion Malkoc für die Hilfe beim GRK 1621. Und Hubertus Luetkens für die Hilfestellungen bei den μSR-Messreisen. Es hat immer ausgesprochen viel Spaß gemacht, ihn am PSI zu besuchen.

Desweiteren danke ich Prof. Wosnitza für die vollkommen unkomplizierte Übernahme der Tätigkeit als Zweitgutachter.

Und ich danke meiner Familie und meinen Freunden für die Unterstützung während der Promotion. Auch wenn die Fragen "Wann bist du denn fertig?" und "Was machst du nachher?," welche in regelmäßigen Zweitagesabständen aufkamen, ab und zu auch mal etwas nervig waren. Aber so hatte ich direkt einen zusätzlichen Grund, schneller fertig zu werden.

Last but not least möchte ich der Bierstube danken, auch wenn sie das Ende meiner Promotion nicht mehr erleben kann. Es gab einfach keinen besseren Ort, um nach Feierabend etwas abzuspannen oder um physikalische Probleme in entspannter Athmosphäre bei ein, zwei oder auch acht Bier zu diskutieren. Dazu gehören auch die üblichen Verdächtigen der Montagsrunde.

Versicherung

Hiermit versichere ich, dass ich die vorliegende Arbeit ohne unzulässige Hilfe Dritter und ohne Benutzung anderer als der angegebenen Hilfsmittel angefertigt habe; die aus fremden Quellen direkt oder indirekt bernommenen Gedanken sind als solche kenntlich gemacht. Die Arbeit wurde bisher weder im Inland noch im Ausland in gleicher oder hnlicher Form einer anderen Prfungsbehrde vorgelegt. Die vorliegende Dissertation wurde am Institut für Festköperphysik der Technischen Universität Dresden unter der wissenschaftlichen Betreuung von Herrn Professor Dr. Hans-Henning Klauß angefertigt. Ich erkenne hiermit die Promotionsordnung der Fakultät Mathematik und Naturwissenschaften der Technischen Universität Dresden vom 23.2.2011 an.

Dresden, den 27. April 2015